Multi-contrast Photoacoustic Computed Tomography

Thesis by

Lei Li

In Partial Fulfillment of the Requirements for
the Degree of
Doctor of Philosophy

CALIFORNIA INSTITUTE OF TECHNOLOGY
Pasadena, California

2019
Defended April 5, 2019

© 2019

Lei Li
ORCID: 0000-0001-6164-2646

All rights reserved

ACKNOWLEDGMENTS

I would like to express my sincere gratitude to my advisor, Professor Lihong Wang, for his support, guidance, encouragement, and the countless hours he has spent for me through all my years as a graduate student. His mentoring is always the key power that drives me through my Ph.D. study. Without his constructive advice and discussion, I would not have accomplished this work. In addition to the academic supervising, Dr. Wang also helps me to set up a high ethical standard which I can benefit from for my career and life.

I would like to thank my committee members, Drs. Changhuei Yang, Yu-Chong Tai, Mikhail Shapiro, Yuki Oka, for their invaluable advice and help on my research. Especially, I thank Dr. Changhuei Yang, as my committee chair, for his great support and help during my graduate study. I also thank Dr. Yuki Oka for his professional advice and support on applying our engineering innovation to neuroscience study.

I am grateful to Dr. Konstantin Maslov, who has been a mentor, a colleague, and a friend throughout my Ph.D. study. Without his ingenious design, patient instruction and inspiring discussion, this dissertation would not be possible. I express special thanks to my collaborator, Dr. Vladislav Verkhusha, for his creative development on protein engineering. It is his involvement that advances our technique and great expands the applications. I am also grateful to my colleagues, Drs. Song Hu, Jun Xia, and Junjie Yao, for their generous help at the early stage of my Ph.D. research. I also thank Drs. Liren Zhu, Cheng Ma, Guo Li, Chiye Li, Yan Liu, Alejandro Garcia-Uribe for their considerable assistance, other lab members for their fruitful discussions and friendship.

I appreciate my parents in China for their endless support and unrequited love.

Finally, my one true love and my wife, Li Li, deserves far more credit than I can give her.

This work was sponsored by National Institutes of Health (NIH) grants NIH grants EB016986, CA186567, NS090579, NS099717, and EB016963.

DEDICATION

To my wife Li Li, my daughters Eleanor and Evenly, my parents, and my parents in law,

for their true love and support.

ABSTRACT

Imaging of small animals has played an indispensable role in preclinical research by providing high dimensional physiological, pathological, and phenotypic insights with clinical relevance. Yet pure optical imaging suffers from either shallow penetration (up to ~1–2 mm) or a poor depth-to-resolution ratio (~3), and non-optical techniques for whole-body imaging of small animals lack either spatiotemporal resolution or functional contrast. A stand-alone single-impulse photoacoustic computed tomography (PACT) system has been built, which successfully mitigates these limitations by integrating high spatiotemporal resolution, deep penetration, and full-view fidelity, as well as anatomical, dynamical, and functional contrasts. Based on hemoglobin absorption contrast, the whole-body dynamics and large scale brain functions of rodents have been imaged in real time. The absorption contrast between cytochrome and lipid has enabled PACT to resolve MRI-like whole brain structures. Taking advantage of the distinct absorption signature of melanin, unlabeled circulating melanoma cells have been tracked in real time *in vivo*.

Assisted by near-infrared dyes, the perfusion processes have been visualized in rodents. By localizing single-dyed droplets, the spatial resolution of PACT has been improved by six-fold *in vivo*. The migration of metallic-based microrobots toward the targeted regions in the intestines has been monitored in real time. Genetically encoded photochromic proteins benefit PACT in detection sensitivity and specificity. The unique photoswitching characteristics of different photochromic proteins allow quantitative multi-contrast imaging at depths. A split version of the photochromic protein has permitted PA detection of protein-protein interactions in deep-seated tumors. The photochromic behaviors have also been utilized to guide photons to form an optical focus inside live tissue. As a rapidly evolving imaging technique, PACT promises pre-clinical applications and clinical translation.

PUBLISHED CONTENT AND CONTRIBUTIONS

1. [Zhang, P., **L. Li**], L. Lin, J. Shi, L. V. Wang (2019). "*In vivo* superresolution photoacoustic computed tomography by localization of single dyed droplets". In: *Light: Science & Applications* 8(1), 36. doi: 10.1038/s41377-019-0147-9

   L.L participated in the conception of the project, constructed the system, performed the experiments, analyzed the data, and participated in the writing of the manuscript.

2. [Zhang, P., **L. Li**], L. Lin, P. Hu, J. Shi, Y. He, L. Zhu, Y. Zhou and L. V. Wang (2018). "High-resolution deep functional imaging of the whole mouse brain by photoacoustic computed tomography *in vivo*". In: *Journal of Biophotonics* 11(1): e201700024. doi: 10.1002/jbio.201700024

   L.L participated in the conception of the project, constructed the system, performed the experiments, analyzed the data, and participated in the writing of the manuscript.

3. [Qu, Y., **L. Li**], Y. Shen, X. Wei, T. T. Wong, P. Hu, J. Yao, K. Maslov and L. V. Wang (2018). "Dichroism-sensitive photoacoustic computed tomography". In: *Optica* 5(4): 495-501. doi: 10.1364/OPTICA.5.000495

   L.L participated in the conception of the project, performed the experiments, analyzed the data, and participated in the writing of the manuscript.

4. Matthews, T. P., J. Poudel, **L. Li**, L. V. Wang and M. A. Anastasio (2018). "Parameterized Joint Reconstruction of the Initial Pressure and Sound Speed Distributions for Photoacoustic Computed Tomography". In: *SIAM Journal on Imaging Sciences* 11(2): 1560-1588. doi: 10.1137/17M1153649

   L.L performed the experiments, and participated in the writing of the manuscript.

5. Liu, W., Y. Zhou, M. Wang, **L. Li**, E. Vienneau, R. Chen, J. Luo, C. Xu, Q. Zhou and L. V. Wang (2018). "Correcting the limited view in optical-resolution photoacoustic microscopy". In: *Journal of Biophotonics* 11(2): e201700196. doi: 10.1002/jbio.201700196

   L.L participated in the conception of the project and the writing of the manuscript.

6. **Li, L.**, A. A. Shemetov, M. Baloban, P. Hu, L. Zhu, D. M. Shcherbakova, R. Zhang, J. Shi, J. Yao and L. V. Wang (2018). "Small near-infrared photochromic protein for photoacoustic multi-contrast imaging and detection of protein interactions *in vivo*". In: *Nature Communications* 9(1): 2734. doi: 10.1038/s41467-018-05231-3

   L.L participated in the conception of the project, constructed the system, performed the experiments, analyzed the data, and participated in the writing of the manuscript.

7. Lin, L., P. Hu, J. Shi, C. M. Appleton, K. Maslov, **L. Li**, R. Zhang and L. V. Wang (2018). "Single-breath-hold photoacoustic computed tomography of the breast". In: *Nature Communications* 9(1): 2352. doi: 10.1038/s41467-018-04576-z

   L.L constructed the control program, and participated in the writing of the manuscript.

8. Imai, T., J. Shi, T. T. Wong, **L. Li**, L. Zhu and L. V. Wang (2018). "High-throughput ultraviolet photoacoustic microscopy with multifocal excitation". In: *Journal of Biomedical Optics* 23(3): 036007.

   L.L participated in the conception of the project, developed the reconstruction algorithm, and participated in the writing of the manuscript.

9. Hsu, H.-C., **L. Li**, J. Yao, T. T. Wong, J. Shi, R. Chen, Q. Zhou and L. V. Wang (2018). "Dual-axis illumination for virtually augmenting the detection view of optical-resolution photoacoustic microscopy". In: *Journal of Biomedical Optics* 23(7): 076001. doi: 10.1117/1.JBO.23.3.036007

   L.L participated in the conception of the project, designed the experiments, and participated in the writing of the manuscript.

10. [Yeh, C., **L. Li**], L. Zhu, J. Xia, C. Li, W. Chen, A. Garcia-Uribe, K. I. Maslov and L. V. Wang (2017). "Dry coupling for whole-body small-animal photoacoustic computed tomography". In: *Journal of Biomedical Optics* 22(4): 041017. 1 doi: 10.1117/1.JBO.22.4.041017

    L.L constructed the system, designed the experiments, analyzed the data, and participated in the writing of the manuscript.

11. Rao, B., R. Zhang, **L. Li**, J.-Y. Shao and L. V. Wang (2017). "Photoacoustic imaging of voltage responses beyond the optical diffusion limit". In: *Scientific Reports* 7(1): 2560. doi: 10.1038/s41598-017-02458-w

    L.L performed the experiments, analyzed the data, and participated in the writing of the manuscript.

12. Poudel, J., T. P. Matthews, **L. Li**, M. A. Anastasio and L. V. Wang (2017). "Mitigation of artifacts due to isolated acoustic heterogeneities in photoacoustic computed tomography using a variable data truncation-based reconstruction method". In: *Journal of Biomedical Optics* 22(4): 041018. doi: 10.1117/1.JBO.22.4.041018

    L.L performed the experiments, and participated in the writing of the manuscript.

13. **Li, L.**, L. Zhu, Y. Shen and L. V. Wang (2017). "Multiview Hilbert transformation in full-ring transducer array-based photoacoustic computed tomography". In: *Journal of Biomedical Optics* 22(7): 076017. doi: 10.1117/1.JBO.22.7.076017

    L.L participated in the conception of the project, performed the experiments, analyzed the data, and participated in the writing of the manuscript.

14. **Li, L.**, L. Zhu, C. Ma, L. Lin, J. Yao, L. Wang, K. Maslov, R. Zhang, W. Chen and J. Shi (2017). "Single-impulse panoramic photoacoustic computed tomography of small-animal whole-body dynamics at high spatiotemporal resolution". In: *Nature Biomedical Engineering* 1(5): 0071. doi: 10.1038/s41551-017-0071

    L.L participated in the conception of the project, constructed the system, performed the experiments, analyzed the data, and participated in the writing of the manuscript.

15. [Yao, J., A. A. Kaberniuk, L. Li], D. M. Shcherbakova, R. Zhang, L. Wang, G. Li, V. V. Verkhusha and L. V. Wang (2016). "Multiscale photoacoustic tomography using reversibly switchable bacterial phytochrome as a near-infrared photochromic probe". In: *Nature Methods* 13(1): 67. doi: 10.1038/nmeth.3656

    L.L constructed the system, performed the experiments, analyzed the data, and participated in the writing of the manuscript.

16. Wong, T. T., Y. Zhou, A. Garcia-Uribe, L. Li, K. Maslov, L. Lin and L. V. Wang (2016). "Use of a single xenon flash lamp for photoacoustic computed tomography of multiple-centimeter-thick biological tissue *ex vivo* and a whole mouse body *in vivo*". In: *Journal of Biomedical Optics* 22(4): 041003. doi: 10.1117/1.JBO.22.4.041003

    L.L developed the reconstruction algorithm, and participated in the writing of the manuscript.

17. Lin, L., P. Zhang, S. Xu, J. Shi, L. Li, J. Yao, L. Wang, J. Zou and L. V. Wang (2016). "Handheld optical-resolution photoacoustic microscopy". In: *Journal of Biomedical Optics* 22(4): 041002. doi: 10.1117/1.JBO.22.4.041002

    L.L participated in the design of the system and the writing of the manuscript.

18. Li, L., J. Xia, G. Li, A. Garcia-Uribe, Q. Sheng, M. A. Anastasio and L. V. Wang (2016). "Label-free photoacoustic tomography of whole mouse brain structures *ex vivo*". In: *Neurophotonics* 3(3): 035001. doi: 10.1117/1.NPh.3.3.035001

    L.L participated in the conception of the project, performed the experiments, analyzed the data, and participated in the writing of the manuscript.

19. He, Y., L. Wang, J. Shi, J. Yao, **L. Li**, R. Zhang, C.-H. Huang, J. Zou and L. V. Wang (2016). "*In vivo* label-free photoacoustic flow cytography and on-the-spot laser killing of single circulating melanoma cells". In: *Scientific Reports* 6: 39616. doi: 10.1038/srep39616

    L.L performed the experiments, analyzed the data, and participated in the writing of the manuscript.

20. Yao, J., L. Wang, J.-M. Yang, K. I. Maslov, T. T. Wong, **L. Li**, C.-H. Huang, J. Zou and L. V. Wang (2015). "High-speed label-free functional photoacoustic microscopy of mouse brain in action". In: *Nature Methods* 12(5): 407. doi: 10.1038/nmeth.3336

L.L performed the experiments, analyzed the data, and participated in the writing of the manuscript.

21. Lin, L., J. Yao, **L. Li**, and L. V. Wang (2015). "*In vivo* photoacoustic tomography of myoglobin oxygen saturation". In: *Journal of Biomedical Optics* 21(6): 061002. doi: 10.1117/1.JBO.21.6.061002

    L. L developed the reconstruction algorithm, and participated in the writing of the manuscript.

22. Lin, L., J. Xia, T. T. Wong, **L. Li** and L. V. Wang (2015). "*In vivo* deep brain imaging of rats using oral-cavity illuminated photoacoustic computed tomography". In: *Journal of Biomedical Optics* 20(1): 016019. doi: 10.1117/1.JBO.20.1.016019

    L. L developed the reconstruction algorithm, and participated in the writing of the manuscript.

23. Li, G., **L. Li**, L. Zhu, J. Xia and L. V. Wang (2015). "Multiview Hilbert transformation for full-view photoacoustic computed tomography using a linear array". In: *Journal of Biomedical Optics* 20(6): 066010. doi: 10.1117/1.JBO.20.6.066010

    L.L performed the experiments, analyzed the data, and participated in the writing of the manuscript.

24. [Zhu, L., **L. Li**], L. Gao and L. V. Wang (2014). "Multiview optical resolution photoacoustic microscopy". In: *Optica* 1(4): 217-222. doi: 10.1364/OPTICA.1.000217

    L.L participated in the conception of the project, constructed the system, performed the experiments, and participated in the writing of the manuscript.

25. Zhang, Y. S., J. Yao, C. Zhang, **L. Li**, L. V. Wang and Y. Xia (2014). "Optical-Resolution Photoacoustic Microscopy for Volumetric and Spectral Analysis of Histological and Immunochemical Samples". In: *Angewandte Chemie* 126(31): 8237-8241. doi:10.1002/ange.201403812

    L.L performed the experiments, and participated in the writing of the manuscript.

26. **Li, L.**, C. Yeh, S. Hu, L. Wang, B. T. Soetikno, R. Chen, Q. Zhou, K. K. Shung, K. I. Maslov and L. V. Wang (2014). "Fully motorized optical-resolution photoacoustic microscopy". In: *Optics letters* 39(7): 2117-2120. doi: 10.1364/OL.39.002117

    L.L participated in the conception of the project, constructed the system, performed the experiments, analyzed the data, and participated in the writing of the manuscript.

[ ], equal contribution.

TABLE OF CONTENTS

Acknowledgments iii

Dedication iv

Abstract v

Published content and contributions vi

Table of contents x

List of illustrations and/or tables xii

List of frequently used abbreviations xxx

Chapter I: Introduction 1

    Background and Motivation 1

    Photoacoustic computed tomography (PACT) 3

    Dissertation outline 5

Chapter II: Single-impulse panoramic PACT (SIP-PACT) 7

    Introduction and motivation 7

    Methods 8

    Results and discussion 15

Chapter III: Linear-array based full-view high-resolution PACT 25

    Introduction and motivation 25

    Methods 25

    Results and discussion 28

Chapter IV: Multi-contrast PACT with endogenous contrasts 33

    Monitoring largescale hemodynamic responses 33

    Imaging brain structures 36

    Tracking of circulating melanoma tumor cells 42

Chapter V: Multi-contrast PACT with exogenous contrasts 47

    PACT of organic near-infrared dyes 47

    PACT of microparticles—metallic microrobots 54

PACT of genetically encoded photoswitchable proteins 57
Chapter VI: Conclusions and outlook 83
Bibliography 85

LIST OF ILLUSTRATIONS AND/OR TABLES

List of Figures

Number *Page*

Figure 1. Configurations of PACT [5]. (a) A linear array based PACT system, where optical fiber bundles flank a linear ultrasonic array for light delivery. (b) A circular/ring array based PACT system, where the laser beam is broadened and homogenized by an engineer diffuser for illumination and the PA waves are received laterally with 2π in-plane coverage. (c) A hemispheric array based PACT system. (d) A planar array based PACT system, where a 2D Fabry-Perot interferometer is used as the planar ultrasonic detector array. The PA signals are detected by raster scanning an interrogation beam over the sensing plane of the interferometer. 3

Figure 2. The electrical impulse response (EIR) of the SIP-PACT system. (a) The raw radio frequency (RF) signal from each ultrasonic transducer element corresponding to a point PA source at the center of the full-ring array. The black solid line represents the mean value of all transducer elements' responses, and the gray region represents the standard deviation across the elements. (b) Fourier transform amplitude of each RF signal in (a), showing the bandwidth of the transducer array is about 4.55 MHz. The black solid line represents the mean value of the spectral amplitude of all RF signals, and the gray region represents the standard deviation across the elements. 9

Figure 3. Schematics of the SIP-PACT system for (a) brain and (b) trunk imaging. During dual-wavelength illumination, all lasers fire at 10 Hz and the delay time between the dual-pulse is 50 μs. For single-wavelength illumination, the 1064-nm laser fires at 50 Hz and the Ti: Sapphire (Ti-Sa) laser fires at 20 Hz. BC, beam combiner; CL, conical lens; MBS, magnetic base scanner; OC, optical condenser; USTA, (full-ring) ultrasonic transducer array; WT, water tank. (c) Close up of the green dashed box region in (b), which shows the confocal design of light delivery and PA wave detection. 11

Figure 4. Numerical simulation results of dual-SOS reconstruction, forward data is generated by the k-Wave toolbox (http://www.k-wave.org/). (a) Schematic of the simulation. (b) The optical absorption distribution of the numerical phantom. Reconstructed images using universal back projection based on (c) single speed with v = 1489.8 m s^{-1} and (d) dual speed with v_1 = 1480 m s^{-1} (in water) and v_2 = 1520 m s^{-1} (in tissue), where the close-up insets show the splitting artifacts due to the mismatched speed of sound. 13

Figure 5. Image quality improvement by dual-SOS reconstruction. (a) Definition of parameters used in half-time dual-speed-of-sound universal back projection. (b) Position of a point source back-projected using single-speed reconstruction. Color represents the in-plane azimuthal angle of the transducer array. In the calculation, $R_x = R_y$ = 10 mm, $x_0 = y_0 = 0$, v_1 = 1.570 m s^{-1} (in tissue), v_2 = 1.506 m s^{-1} (in water), and R_d = 50 mm. The correct position of the point source is labeled by the red star. (c) and (d) *In vivo* images of a cross-section of a mouse trunk (liver) reconstructed using half-time universal back projection based on (c) single speed with v = 1.520 m s^{-1} and (d) dual speed with v_1 = 1.590 m s^{-1} (in tissue) and v_2 = 1.507 m s^{-1} (in water). 15

Figure 6. Label-free SIP-PACT of small-animal whole-body anatomy from the brain to the trunk. (a) Vasculature of the brain cortex; SSS, superior sagittal sinus. (b) Cross-sectional image of the upper thoracic cavity; HT, heart; LL, left lung; RL, right lung; ST, sternum. (c) Cross-sectional image of lower thoracic cavity; LV, liver; TA, thoracic aorta; VE, vertebra. (d) Cross-sectional image of two lobes of liver; AA, abdominal aorta; IVC, inferior vena cava; LLV, left lobe of liver; PV, portal vein; RLV, right lobe of liver. (e) Cross-sectional image of upper abdominal cavity; IN, intestines; SC, spinal cord; SP, spleen; SV, splenic vein. (f) Cross-sectional imaging of lower abdominal cavity; BM, backbone muscles; CM, cecum; LK, left kidney; RK, right kidney. 16

Figure 7. Quantification of the in-plane resolution of the SIP-PACT. (a) An image of two crossed tungsten wires, each with a nominal diameter of 50 µm. (b) The PA amplitude distribution along the red dash-dot line in (a). (c) The contrast-to-noise ratio (CNR) versus the shift in the sum of the original line profile shown in (b) and the shifted one. The in-plane resolution, defined as the shift corresponding to 6-dB CNR, is 125 µm. 17

Figure 8. Quantification of elevational resolution of SIP-PACT. (a) Simulated acoustic focus field in the *x-z* plane. (b) The PA image of a tungsten wire with a nominal diameter of 50 µm, projected on the *x-z* plane. (c) The simulated line profiles of (a) at the center of the ring (indicated in (a) by the solid white arrow) and at 6.5 mm (off-center, indicated in (a) by the dashed white arrow). (d), as (c), but showing the measured line profiles of (b). 17

Figure 9. Label-free imaging of small-animal whole-body dynamics. (a) Cross-sectional image of the upper thoracic cavity, where the red solid line crosses a rib, and the blue dashed line crosses the heart wall. (b) Line profiles in (a) versus time show the displacements of (upper panel) the rib during respiration and (lower panel) the heart wall during heartbeats. The traces of the rib and heart wall movements are identified and highlighted with solid red lines. (c) Fourier transforms of the rib and heart wall movements showing the respiratory frequency and heartbeat frequency, respectively. (d) Heartbeat encoded arterial network mapping overlaid on the anatomical image. (e) Cross-sections of the vessels highlighted by arrows in (d), showing changes associated with arterial pulse propagation. (f) A zoomed-in of the dashed box in (e) shows the relative phase delay between the two curves of the vessels' cross sections. 18

Figure 10. Validation of the SIP-PACT measurement of breathing motion and heartbeats. The pressure sensor and electrocardiography (ECG) measurement were conducted in parallel with the SIP-PACT imaging on the same mouse. (a) Co-registered measurement of breathing motion from SIP-PACT (top) and the pressure sensor (bottom). (b) Fourier transform of (a), which shows the identical respiratory frequency measured by SIP-PACT and the pressure sensor. (c) Co-registered measurement of heartbeats from SIP-PACT (top) and ECG (bottom). (d) Fourier transform of (b), which shows the identical heartbeat frequency measured by SIP-PACT and ECG. 20

Figure 11. Setup for rat brain imaging. The rat head was mounted vertically during imaging and the light was obliquely delivered to the rat cortex. 21

Figure 12. Deep imaging of rat whole brain functions and whole-body anatomy. (a) Rat whole brain vasculature in the coronal plane. (b) Segmentations of different functional regions of the brain. (c) Seed-based functional connectivity analyses of RSGc (top row), Hippocampus (middle row), and Thalamus (bottom row) regions on both sides of the brain. (d) Correlation matrix of the 16 functional regions labeled in (b). Notice the correlation between left and right hemispheres, as well as the correlation across different regions in the neocortex. S1Sh, primary somatosensory–shoulder region; S1HL, primary somatosensory cortex–hindlimb region; M1, primary motor cortex; M2, secondary motor cortex; RSD, retrosplenial dysgranular cortex; RSGc, retrosplenial granular cortex; Hip, hippocampus; Thal, thalamus. (e) and (f) Cross-sectional images of a rat wholebody. IN, intestine; LK, left kidney; LLV, left liver; RK, right kidney; RLV, right liver; SC, spinal cord; SP, spleen; SV, splenic vein. 23

Figure 13 Schematic setup of linear-array based full-view PACT for mouse brain imaging. 26

Figure 14. Coronal plane PACT of a mouse brain through the intact skull (Bregma −1.0 mm). (a-e) Limited-view images reconstructed at view angles of –76, –36, 0, 36 and 76 degrees, respectively. Each of these images was averaged over 200 acquisitions. (f) Full-view planar image combined from the 39 limited-view images. The scale bar is 2 mm. 27

Figure 15. Functional connectivity in a mouse brain acquired by a linear-array based full-view PACT. (a-d) The correlation maps calculated at four representative functional regions (black circles) are overlaid onto the anatomic image that was synthesized from multiple limited-view images (Bregma −1.0 mm). The scale bar is 2 mm. S1HL, somatosensory 1, hindlimb region; HIP, hippocampal region; TH, thalamus; RHP, retrohippocampal region. (e) Time series of the filtered PA signals of a pair of correlated regions as marked in (a). The red and blue curves are corresponding to the points marked in white and black circles, respectively. Amplitudes are normalized to the maximum. 29

Figure 16. Epileptiform activities of a mouse brain during a seizure. The fractional changes in the PA amplitude at different times after the injection of 4-aminopyridine solution are superimposed on the anatomic image (Bregma –1.0 mm). The scale bar is 2 mm, and the arrow indicates the injection site. 31

Figure 17. (a) The absorption spectra of oxy-hemoglobin (HbO_2) and deoxy-hemoglobin (HbR), and the absorption ratio of deoxy-hemoglobin to oxy-hemoglobin (HbR/HbO_2). (b) Fractional changes of blood's absorption coefficient (μ_a) corresponding to the blood sO_2 change ($d(\Delta\mu_a/\mu_a)$ /

d(sO_2)) with visible and NIR light illumination. Wavelengths from 626 nm to 720 nm provide an sO_2 sensitive imaging window for SIP-PACT (highlighted by the gray area). 33

Figure 18. SIP-PACT of mouse whole-body oxygenation dynamics. sO_2 mapping of mouse cortical vasculatures during (a) hyperoxia and (b) hypoxia. (c) Brain sO_2 changes during oxygen challenges, the gray rectangle outlines the challenge periods. (d). Changes in concentrations of oxy-hemoglobin and deoxy-hemoglobin during oxygen challenges, the gray rectangle outlines the challenge periods. (e) Fractional changes in blood oxygen level in the cross-sectional image of the lower abdominal cavity. (f) Normalized PA amplitude, corresponding to blood oxygen level, in internal organs during hyperoxia and hypoxia, where the hollow bars represent the baseline amplitudes and the solid bars represent the plateau amplitudes during challenge (n = 50, error bars are s.e.m.). The p values were calculated by paired Student's *t*-test. 34

Figure 19. Fractional changes of blood oxygen levels in the cross-section of (a) the lower abdominal cavity during oxygen challenge and (b) the liver during oxygen challenge. 36

Figure 20. Label free PA imaging. (a) Absorption coefficient spectra of endogenous tissue chromophores at typical concentrations in the human body (Adapted from http://omlc.ogi.edu/spectra and http://www.ucl.ac.uk/medphys/research/borl/intro/spectra) (b) *In vivo* imaging of the mouse brain cortex through the intact skull (imaging depth: 0.5 mm beneath the skull surface). (c) *In vivo* imaging of the deep mouse brain (imaging depth: 3.0 mm beneath the skull surface). 36

Figure 21. PACT of the saline perfused mouse brain without the skull. (a) Cross-sectional PACT image of the mouse brain at 2.8 mm depth, clearly resolving the structure of the brain. (b) Segmented and annotated image from (a). (c) One slice of a 3D high-resolution MRI image with its structural segmentation superimposed as colored lines, chosen as a gold standard for validation of PACT (Courtesy of Frontiers in Neuroscience) [70]. 37

Figure 22. Spectral PACT of a mouse brain at 2.8 mm depth. 38

Figure 23. Spectral analysis of the origin of optical absorption in the brain. (a) Cross-section imaged at 600 nm wavelength at 2.8 mm depth as part of the 3D brain imaging, with red outlined areas segmented for analysis. (b) Measured PA spectrum and least-squares fit with a mixture of cytochromes *b* and *c*. (c) Histology image of one horizontal section slice stained with hematoxylin and eosin (H&E). 39

Figure 24. Analysis of the origins of the contrast. (a) Cross-section imaged at 600 nm wavelength at 2.8 mm depth selected from the 3D brain images, with brown outlined areas segmented for analysis. (b) Close-up of the region inside the brown square in (a). (c) Comparison of the measured AR between the granular cell layer and the cerebellar white matter and the AR between cytochrome and fat. (d) Histology image of one horizontal section slice stained with luxol fast blue. (e) Close-up of the region inside the brown square in (d). 41

Figure 25. Detection of melanoma cells in blood *in vitro*. (a) Spectra of whole blood (85% sO_2) and melanosome, and the absorption ratio of melanosome and whole blood, which peaks at 680 nm. The melanosome to blood contrast can be maximized with 680-nm excitation. (b) Image of a tube (300 µm in diameter) filled with the mixture of blood and melanoma cells (10^6 cells in 2 mL of bovine blood). The mixture of blood and melanoma cells is driven by a syringe to flow through the tube. The melanoma cells (or cluster) are highlighted by the yellow arrows. (c–e) Time trace plot of each pixel along the red dashed line in (b). The space-time domain slope in (c–e) were computed by linear fitting as ~0.67 mm s^{-1}, representing the flow speed of melanoma cells. 42

Figure 26. Label-free tracking of CTCs in the mouse brain *in vivo*. (a) Baseline cortical vasculature before the injection of melanoma cancer cells, under 680-nm excitation. (b) PA imaging of the mouse cortex after injection of melanoma cancer cells, where colors represent CTCs' flow direction. Flow speed is radially encoded in the color disk by hue saturation (a greater radius indicates faster) (c) Tracking the flowing of cancer cells, where red highlights the moving cancer cells in the current frame, yellow crosses show their initial positions, and the orange dashed lines represent the CTCs' flowing traces. (d) Time trace plot of each pixel along the red dashed line in (a). (e) 2D Fourier transform of (d), which maps lines with the same slope in the space-time domain onto a single line in the spatiotemporal frequency domain. The slope of the red dashed line, computed by linear fitting as 0.65 mm s-1, represents the flow speed of CTCs. The spectral amplitude values were normalized according to the maximum value, and were saturated at 0.15 for display purposes. (f) Flow speed distribution of CTCs in segmented cortical vessels.................... 44

Figure 27. Flowing of melanoma cells in cortical arteries. (a) PA image of the mouse brain cortex after injection of melanoma cancer cells. (b) The time trace plot of each pixel along an artery (the red dashed line in (a)). (c) 2D Fourier transform of (b), which maps lines with the same slope in the space-time domain onto a single line in the spatiotemporal frequency domain. The slope of the red dashed line, computed by linear fitting as 10.0 mm s^{-1}, represents the flow speed of CTCs, which is higher than that in veins... 45

Figure 28. *In vivo* observation of CTCs whose motion in mouse cortex has ceased. (a) The PA image of the mouse brain cortex after injection of melanoma cancer cells. (b) Displacement versus time trace plot of the finally ceased CTCs, where the red line is the displacement of the center position of the non-moving CTCs, and the plateau of the red line represents where and when the CTCs ceased moving. (c) Zoomed-in images of the white dashed box in (a), where the yellow crosses represent the initial center position of the tracked CTC, the red patches label its central position in the current frames, and the orange dashed lines represent the CTCs' flowing traces. 45

Figure 29. Comparison of absorption of the NIR dye and bovine blood (90% sO_2) at 1064 nm. The NIR dye (0.5% mass concentration in deionized water) and bovine blood are filled in silicone tubes (600 µm diameter), which is embedded in agar. (a) PA image of the two tubes filled with NIR dye and bovine blood, with 1064-nm illumination. The signals from blood are amplified by 3-fold for improved display. (b) Line profile of the yellow dashed line in (a), showing that the NIR dye has 19.8-fold more absorption than blood at 1064 nm. Thus the absorption coefficient of the dye solution is 74.7 cm^{-1}. 47

Figure 30. Visualization of dye perfusion in the mouse brain. (a) Images of the mouse cortex after the injection of dye solution at different times. (b) The total PA signal of the mouse brain greatly increases after the injection of dye solution. 48

Figure 31. Visualization of whole-body dye perfusion. (a–f) Cross-sectional images of the lower abdominal cavity at different times after injection of dye solution, showing that dye molecules perfused to both kidneys and the intestinal region. IN, intestine; LK, left kidney; RK, right kidney; SP, spleen. 49

Figure 32. Absorption spectra of HbO_2, HbR, and IR-780 dye solution as well as the absorption coefficient ratio of IR-780 to hemoglobin (80% HbO_2 and 20% HbR). 51

Figure 33. Tracking of single dyed droplets in the brain *in vivo*. (a) A unipolar image of the baseline cortical vasculature that was acquired prior to the injection of droplets. (b) A profile of the PA amplitude along the dashed line in (a). (c) The flow of a droplet (orange dot) in brain vessels, which was tracked over time. The droplet images were overlaid on the baseline vascular image in the region that is bounded by the dashed rectangle in (a). The dotted red circles indicate the initial locations of the droplets, and the dashed arrows indicate the flow pathway and direction. (d) The droplet flow velocities for several cortical vessels. The colors indicate the flow speeds, and the arrows indicate the flow directions. The scale bars are 2, 1 and 2 mm in (a), (c) and (d), respectively. 52

Figure 34. Superresolution imaging of the mouse brain cortex. (a) A unipolar image of the cortical layer that was acquired by conventional PACT using hemoglobin as the contrast. (b) A superresolution PACT image of the cortical layer by localizing single droplets. (c) Amplitude profiles of the conventional image (blue dashed line) and the superresolution image (red solid line) along the dotted lines that are shown in (a) and (b). (d and e) Magnified images of the regions that are bounded by dotted rectangles in (a) and (b). (f) Amplitude profiles along the dotted lines in (d) and (e), where the red solid line corresponds to the profile from the superresolution image, the blue dashed line corresponds to the profile from the conventional image, and the vertical black dashed lines indicate the locations of the two vessels. 54

Figure 35. PA characterization of the MCs. (a) PACT images of Mg particles, blood, and MCs in silicone rubber tubes with laser wavelengths at 720, 750, and 870 nm, respectively. Scale bar, 500 µm. (b) PACT spectra of MCs (red line), blood (blue line), and Mg particles (black line), respectively. (c and d) PACT images (c) and the corresponding PA amplitude (d) of the MCs with different micromotor loading amount, and the dependence of the PA amplitude on the fluence of NIR light illumination (inset in d). Scale bar in c, 500 µm. (e) Dependence of PA amplitude of the MCs (red line) and blood (black line) on the depth of tissue, and the normalized PA amplitude and fluorescence intensity of the MCs under tissue (inset). Norm., normalized; amp., amplitude; Fl., fluorescence; int., intensity. 55

Figure 36. PACT evaluation of the MC dynamics *in vivo*. (a) The time-lapse PACT images of the MCs in intestines for 7.5 hours. The MCs migrating in the intestine are shown in color, the mouse tissue is shown in gray. Scale bar, 2 mm. (b and c) The movement displacement caused by the migration of the MCs in the intestine (b) and by the respiration motion of the mouse (c). (d) Comparison of the speeds of the MC migration and the respiration-induced movement. 57

Figure 37. Structure and photochemical properties of *Rp*BphP1 bacterial phytochrome. **(**a) Organization of a monomer subunit of *Rp*BphP1. (b) Enzymatic synthesis of BV from a heme. (c) Photoswitchings of a BV chromophore from the Pfr state to the Pr state, and vice versa, induced by NIR (~730-790 nm) light and far-red (~630-690 nm) light illumination, respectively. The photoswitchings result from the out-of-plane rotation (black arrows) of the D-ring of BV about the adjacent C15/16 double bond between the C and D pyrrole rings. (d) Absorption spectra of unbound BV photoisomerization in solution measured by a standard spectrophotometer. There is virtually no change in the spectra after 5 min illumination at 630 nm and 780 nm. 59

Figure 38. Optical properties of reversible photoswitching of BphP1. (a) Molar extinction spectra of HbO_2, HbR, Pfr (ON) and Pr (OFF) state BphP1. (b) Absorbance of BphP1 at 780 nm, switched off with 780 nm light illumination and then switched on with 630 nm light illumination. 60

Figure 39. PACT of BphP1-expressing U87 cells at 10 mm depth. (a) Fluorescence microscopic image of the BphP1-expressing U87 cells, where EGFP was co-expressed, providing the fluorescence signal. (b) PA images of U87 cells and HbO_2 placed at 10 mm depth in scattering media mixed with blood to provide background signal. The differential image effectively eliminates the background signals and clearly shows the U87 cells that are otherwise not detectable in the ON and OFF state images. (c) Contrast to noise ratio quantified from the ON state, OFF state, and differential (Diff) PA images. (d) PA signals of BphP1-expressing U87 cells observed over 10 photoswitching cycles. 61

Figure 40. Deep PACT of genetically encoded reversibly switchable BphP1 *in vivo*. (a) PA CNR of BphP1-expressing U87 cells embedded at 10 mm depth versus increasing cell counts. (b) *In vivo* whole-body PACT images of the kidney region of a nude mouse, acquired one week after injection of ~10^6 BphP1-expressing U87 cells into the left kidney. The ON and OFF state PA images clearly show the major blood-enriched internal organs, including the left kidney (LK), right kidney (RK), spinal cord (SC), renal vein (RV), bladder (BL), and spleen (SP). The differential image clearly reveals the tumor in the left kidney. (c) An overlay of the U87 tumor (shown in color) in the left kidney and the blood-dominated OFF state image (shown in gray). (d) Normalized signal profiles of the ON state, OFF state, and differential images along the white dashed line in (b). (e) A representative H&E histological image of the harvested left kidney, showing the tumor region. (f) Deep PACT of a mouse brain U87 tumor expressing BphP1. The tumor (shown in color) was ~3 mm beneath the scalp surface. A global threshold was applied to all the differential images with a threshold level at three times the noise level. 62

Figure 41. Development of a 1.5-fold smaller photochromic probe for PA imaging. Monomers (shown) of naturally dimeric bacterial phytochromes (BphPs) share a common domain structure. It is represented here by the photosensory core module (PCM), formed by the PAS-GAF-PHY domain triad, and output domains. BV is covalently bound with conservative cysteine from the PAS domain and secured to a chromophore-binding pocket in the GAF domain. The molecular weight of the BphPs monomer is ~80 kDa. RpBphP1, consists of the regular PCM and the output PAS/PAS and HOS domains. The domain organization of BphP from Deinococcus radiodurans, DrBphP, is comprised of the PCM and the output histidine kinase (HisK) domain. We truncated full-length DrBphP to its PCM and called the result DrBphP-PCM, achieving a 1.5-fold reduction in the molecular weight of the PA probe. 64

Figure 42. Spectral and PA characterization of the DrBphP-PCM. (a) Molar extinction spectra of HbO_2, HbR, Pfr (ON) and Pr (OFF) state of DrBphP-PCM and RpBphP1. (b) Schematic of the whole-body PACT system. BC, beam combiner; CL, conical lens; DAQ, data acquisition unit; ED, engineering diffuser; M, mirror; OC, optical condenser; P, prism; PC, personal computer; pre-A, pre-amplifier; USTA, ultrasonic transducer array. L1, the Ti:Sapphire laser. L2, the optical parametric oscillator (OPO) laser. (c) Time sequence of photoswitching and imaging of BphPs (pop., population). (d) Absorbance of DrBphP-PCM at 780 nm. (e) PA images of BphPs and hemoglobin in clear media. Left column: ON state PA image of BphPs and hemoglobin, middle column: LIR images of BphPs and hemoglobin; right column, decay constant encoded image showing a reliable separation of DrBphP-PCM, RpBphP1, and hemoglobin. Scale bar, 500 µm. (f) PA signal changes upon 780 nm light illumination and their fits. (g) The switching ratio of BphPs and hemoglobin, defined as the PA amplitude ratio between the ON and OFF states, in both clear media (0 mm in depth) and scattering media (12 mm in depth); error bars are s.e.m. (n = 40). 64

Figure 43. *In vivo* separation of two types of cells at depths. (a) LIR image overlaid on a conventional PACT cross-sectional image, highlighting the two tumors of HEK-293 cells expressing both DrBphP-PCM and RpBphP1 (left lobe) or U87 cells expressing DrBphP-PCM (right lobe) inside the liver. (b) Coefficient *b* encoded image overlaid on a conventional PACT image. (c) Coefficient *c* encoded image overlaid on a conventional PACT cross-sectional image. (d) Normalized coefficient *k* encoded image overlaid on a conventional PACT image. (e) PA signal decays and their fits in the tumor regions. (f) The computed coefficients of *b*, *c*, and *k* from the tumor regions. Scale bar, 5 mm. 69

Figure 44. Development of the bimolecular photoacoustic complementation (BiPC) reporter DrSplit. (a) DrBphP-PCM consists of three domains, PAS, GAF, and PHY. The biliverdin (BV) chromophore is covalently bound with conservative cysteine from the PAS domain and secured to a chromophore-binding pocket in the GAF domain. DrBphP-PCM was genetically split into two parts, the PAS domain and GAF-PHY domain, together named DrSplit. In this case, BV does not bind with any part of DrSplit. Genetically fusing one protein of interest (protein A) to one part of DrSplit and another protein of interest (protein B) to another part of DrSplit makes possible the monitoring of protein-protein interactions (PPIs) between protein A and protein B. (b) We used a model rapamycin-induced PPI between the FRB and FKBP proteins for evaluation of DrSplit. FRB was fused to the PAS domain and FKBP was fused to the GAF-PHY domains. Upon addition of rapamycin to the DrSplit, DrBphP-PCM was re-functionalized. 70

Figure 45. Longitudinal imaging of PPIs in a tumor and monitoring of tumor metastases in a mouse liver. ~1×10^6 MTLn3 cells expressing DrSplit were injected into the mouse liver. The mice (n = 4) were imaged at multiple time points after tumor cell injection, and rapamycin was injected via the tail vein ~40-44 h before each PA imaging. (a-d) PA images of the mouse on (a) day 5, (b) day 15, (c) day 24, and (d) day 33 after injection of tumor cells, where the white arrows indicate the secondary tumor. LIR images are overlaid on the anatomical images. The overlay image shows the DrSplit signal in color and the background blood signal in gray. Scale bar, 5 mm. (e) Tumor growth curve, in-plane tumor area vs. time (quantified from LIR images). (f) A representative H&E histological image of a harvested left lobe of a tumorous liver, showing the tumor metastasis, where the primary tumor and secondary tumor are bordered by green and yellow lines, respectively. Scale bar, 1 mm. The close-up H&E image shows the secondary tumor, which can be clearly differentiated from normal tissue. Scale bar, 100 µm. 72

Figure 46. Principle of GePGS guided optical focusing inside scattering media. (a) Photoswitching of DrBphP-PCM chromophore from the Pfr state to the Pr state, and vice versa, induced by 780 nm light and 637 nm light illumination, respectively. The photoswitchings result from the out-of-plane rotation (black arrows) of the D-ring of biliverdin about the adjacent C15/16 double bond between the C and D pyrrole rings. (b) Molar absorption spectra of HbO_2, HbR, Pfr (ON) and Pr (OFF) states of DrBphP-PCM. The absorption ratio (black solid line) between the two states (Pfr/Pr) is ~10 at 780 nm. (c) Time sequence of GePGS guided DOPC system (pop., population). (d) Switching the DrBphP-PCM to ON state by a 637-nm laser with a duration of 24 ms. (e) Switching the DrBphP-PCM to OFF state by a 780-nm laser with a duration of 26 ms and capturing two holograms with an interval of 25 ms. (f) Time reversed focusing on the GePGS inside scattering media. BS beam splitter; RB reference beam. 74

Figure 47. *In vitro* demonstration of focusing light onto GePGS inside scattering media. **(a)** Experimental setup for *in vitro* demonstration. BS, beam splitter; IP, intralipid-gelatin phantom. TML, tissue-mimicking layer. (**b)** Normalized (Norm.) transmittance of the light passing through the tubes with different sizes filled with GePGS. The length of the inner side of the tubes is 50 µm, 100 µm, 200 µm, and 300 µm, respectively. (**c)** Images of the focusing light onto GePGS injected in the tubes with different sizes. Scale bar, 300 µm. (**d)** Image shows that light is focused only onto the GePGS. Two tubes filled with GePGS and blood, respectively, are placed side by side. The white dash-dotted lines represent the inner wall of the tube filled with blood. The length of the inner side of the tubes is 100 µm. Scale bar, 200 µm. (e) Normalized intensity distribution along the yellow line in (**d)**. (**f)** Image of the focusing light onto a tube filled with U87 cells expressing GePGS. It shows that light is focused onto the GePGS expressing cells/cell clusters. The white dash-dotted lines represent the inner wall of the tube. Scale bar, 300 µm. (**g)** Normalized intensity distribution along the yellow line in (**f)**. In (e) and (g), the blue dashed line is the measured value, and the red solid line is the smoothed curve with a span of 10 points. 76

Figure 48. *In vivo* demonstration of focusing light inside tumors. (a) Schematic of the set-up for focusing light inside tumors on the mouse ear *in vivo*. A microscope is placed on a translation stage and can be moved horizontally into the light path to image the time-reversed focus. (b) The speckle correlation coefficient as a function of time for a living-mouse ear. Three speckle decorrelation characteristics were identified. (c) Normalized intensity distribution of the optical foci inside the tumor on the mouse ear. Left, with 637-nm light switching for *N*= 2, 40 and 120, respectively; Right, without 637-nm light switching. Scale bar, 100 µm. (d) Signal enhancement of tagged photons (at 20 Hz) and the PBR of time-reversed focusing as a function of total cycle number *N*. 78

Figure 49. Demonstration of focusing light inside live brain slices. (a) Fluorescence images of the transduced mouse brain *in vivo* and a live brain slice showing the brain tissue expressing GePGS. The differential fluorescence signals between ON and OFF states highlight the brain tissue express RSBPs, which are shown in color; and the background signals are shown in gray. Excitation wavelength, 630 nm. (b) Schematic of the set-up for focusing light inside brain slices. (c) Speckle correlation coefficient as a function of time for a live brain slice. Two speckle decorrelation characteristics are identified. (d) Normalized amplitude spectral density of the detected photons, where a peak is observed at 20 Hz with light switching. (e) Normalized intensity distribution of the optical foci inside the brain slices. Left, with 637-nm light switching for N= 20; Right, without 637-nm light switching. (f) Signal enhancement of tagged photons (at 20 Hz) and the PBR of time-reversed focusing as a function of total cycle number N. 79

List of Tables

Number *Page*

Table 1. Comparison of PAT with deep-tissue (> 2 mm) imaging modalities. 2

Table 2. Spectral and PA properties of RpBphP1 and DrBphP-PCM *in vitro*. . 67

LIST OF FREQUENTLY USED ABBREVIATIONS

2D: Two-dimensional
3D: Three-dimensional
ANSI: American National Standards Institute
BphP: Bacterial phytochromes
BV: Biliverdin IXα
BOLD: Blood oxygenation level dependent
BiFC: Bimolecular fluorescence complementation
BiPC: Photoacoustic complementation
BRET: Bioluminescence energy transfer
CNR: Contrast-to-noise ratio
CTC: Circulating tumor cell
DAQ: Data acquisition
DOPC: digital OPC
DOT: Diffuse optical tomography
DrBphP-PCM: A PCM part of the DrBphP phytochrome from *Deinococcus radiodurans*
DrSplit: A split version of DrBphP-PCM
ECG: Electrocardiography
EIR: Electrical impulse response
FC: Functional connectivity
fMRI: Functional MRI
FP: fluorescent proteins
FRET: Förster resonance energy transfer
FWHM: Full width at half maximum
fUS: Functional ultrasound / Power doppler ultrasound
GePGS: Genetically-encoded photochromic guide star
HbO2: Oxy-hemoglobin
HbR: Deoxy-hemoglobin
H&E: Hematoxylin and eosin

HR-PACT: High-resolution PACT

LA-PACT: Linear array based PACT

LIR: Lock-in reconstruction

MC: Micromotors capsule

MRI: Magnetic resonance imaging

NA: Numerical aperture

NIR: Near infrared

OAT: Optoacoustic tomography

OPC: Optical phase conjugation

OPO: Optical parametric oscillator

PA: Photoacoustic

PALM: Photoactivation localization microscopy

PAM: Photoacoustic microscopy

PAT: Photoacoustic tomography

PBR: Peak-to-background ratio

PCM: Photosensory core module

PDT: Photodynamic therapy

PET: Positron emission tomography

PFA: Paraformaldehyde

PPI: Protein-protein interactions

PSF: Point spread function

RA-PACT: Ring array based PACT

RF: Radio frequency

RpBphP1: Phytochrome from the bacterium *Rhodopseudomonas palustris* (referred to as BphP1)

RSBP: Reversibly switchable bacterial phytochrome

RSFC: Resting-state functional connectivity

SIP-PACT: Single-impulse photoacoustic computed tomography

sO_2: Hemoglobin oxygen saturation

SOS: Speed-of-sound

SPECT: Single-photon emission computed tomography

STORM: Stochastic optical reconstruction microscopy

UBP: Universal back-projection

US: Ultrasound

X-ray CT: X-ray computed tomography

Chapter 1

INTRODUCTION

Background and Motivation

Photoacoustic tomography (PAT), also known as optoacoustic tomography (OAT), refers to cross-sectional or three-dimensional (3D) imaging of a material that is based on the photoacoustic (PA) effect. Although Alexander Graham Bell firstly reported the PA effect in 1880 [1], the development of PAT took off after the advent of ultrasonic transducers, computers, and lasers. Typically, in PAT non-ionizing laser pulses (~ps–ns pulse width) are directed to the object (when radio frequency pulses are used, the technology is referred to as thermoacoustic tomography). Some of delivered optical energy is absorbed by the object and converted into heat. The heat then induces a pressure rise through thermoelastic expansion. The pressure rise propagates as an ultrasonic wave, which is referred to as a PA wave. The PA waves are detected by ultrasonic transducers and are processed by a computer to form an image.

PAT is a hybrid imaging technique that combines two forms of energy—optical and acoustic energy. The motivation for PAT is to combine the contrast of optical absorption with the spatial resolution of ultrasound for deep imaging in the optical quasidiffusive or diffusive regime. Table 1 compares PAT with different biomedical imaging modalities, including the optical imaging approaches and non-optical approaches.

PAT inherits the advantages of both optical imaging and ultrasound imaging. First, PAT is sensitive to the optical absorption of molecules. By preferentially exciting different molecules with carefully selected optical wavelengths, PAT reveals abundant contrasts based on the chemical compositions. Using on the endogenous absorption of hemoglobin, cytochrome, and DNA/RNA, PAT offers anatomical, functional, metabolic, and histologic imaging. By exploiting exogenous contrasts, including organic dyes, proteins, and nanoparticles, PAT can perform molecular and cellular imaging. Second, PAT directly detects acoustic waves induced by the excitation photons, regardless of whether they are ballistic photons or scattered/diffused photons, thus PAT achieves far greater penetration than optical microscopy. More importantly, acoustic waves are much less scattered inside biological tissue (about three orders of magnitude weaker than optical scattering on a per unit path length basis); therefore, PAT can provide orders of magnitude higher spatial resolution deep in tissue (> 2 mm) than pure optical imaging technology. In addition, the image resolution and imaging depth of PAT are scalable with ultrasonic frequency within the reach of diffuse photons. As ultrasonic center frequency and bandwidth increase, spatial resolution improves at the expense of penetration. PAT has demonstrated multiscale imaging from organelles to small-animal whole bodies and human organs.

Table 1. Comparison of PAT with deep-tissue (> 2 mm) imaging modalities* [2-4]

Modality*	Temporal resolution**	Spatial resolution	Throughput	Sensitivity (moles of detected substance)	Soft-tissue contrast	Functional contrast	Ionizing Radioactivity
X-ray CT	~0.1 s	30–100 μm	Low	10^{-6}	Low	Low	Yes
MRI	seconds to minutes	50–200 μm	Low	10^{-9}–10^{-6}	High	Moderate	None
PET/SPECT	~0.3 s	1–2 mm	Low	10^{-15}–10^{-14}	NA	High	Yes
US (operating at 5 MHz)	~ms	100–200 μm	High	10^{-8}	Moderate	Moderate	None
DOT	~ms	Poor: 1/3 of imaging depth	High	10^{-12}	Low	High	None
PAT (operating at 5 MHz)	50 μs	100–200 μm	High	10^{-12}	High	High	None

* The high-resolution optical imaging techniques, such as multiphoton microscopy and optical coherence tomography, penetrate <2 mm, which are not listed in the table.

** X-ray CT: X-ray computed tomography. MRI: magnetic resonance imaging. PET: positron emission tomography. SPECT: single-photon emission computed tomography. US: ultrasound. DOT: diffuse optical tomography.

*** Image formation time, including signal excitation and acquisition. Changes of the object within this duration induce motion artifacts in the final images.

Photoacoustic computed tomography (PACT)

In light of the image formation methods, PAT has two primary incarnations: inverse-reconstruction-based photoacoustic computed tomography (PACT) [5, 6] and focused-scanning-based photoacoustic microscopy (PAM) [7-13]. When PAT is implemented in the form of computed tomography, a broadened laser beam illuminates the entire tissue object. Ultrasonic transducers or array are placed around the object to receive the emitted acoustic waves simultaneously. The received PA signals are then amplified and digitized through a data-acquisition system. Finally, inverse digital reconstruction yields an image, which maps the optical absorption of the tissue.

PACT has been primarily configured in four geometries below: linear, circular, spherical and planar geometry, or their scanning equivalents (**Fig. 1**) [14]. In this dissertation, PACT has been implemented mainly in the circular and linear geometry.

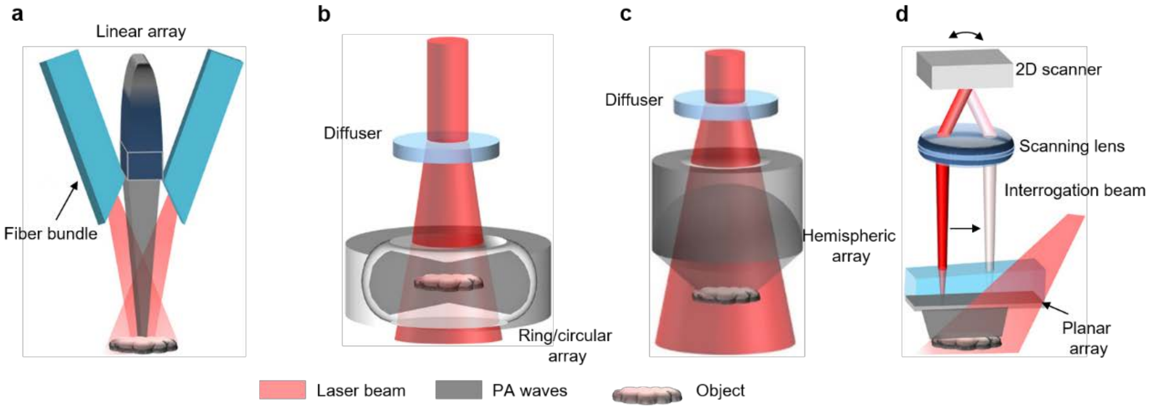

Figure 1. Configurations of PACT [14]. (a) A linear array based PACT system, where optical fiber bundles flank a linear ultrasonic array for light delivery. (b) A circular/ring array based PACT system, where the laser beam is broadened and homogenized by an engineer diffuser for illumination and the PA waves are received laterally with 2π in-plane coverage. (c) A hemispheric array based PACT system. (d) A planar array based PACT system, where a 2D Fabry-Perot interferometer is used as the planar ultrasonic detector array. The PA signals are detected by raster scanning an interrogation beam over the sensing plane of the interferometer.

Researchers first explored circular/ring array based PACT (RA-PACT) or its scanning equivalent in 2003; and it demonstrated the functional PA imaging of the rodent brain functions through an intact scalp for the first time [15]. Triggered particularly by first functional PACT, the PA field experiences a rapid growth. RA-PACT provides 2π angular in-plane coverage, effectively mitigating the limited view artifacts [16-19]. The current state-of-the-art RA-PACT, equipped with a 512-element full-ring ultrasonic transducer array, one-to-one mapped amplification and digitization and advanced reconstruction algorithm, yields great performance of high spatiotemporal resolution, deep penetration, anatomical, dynamical and functional contrasts, and full-view fidelity [4], which I will detail in Chapter II.

Linear array based PACT (LA-PACT) has widely usage for pre-clinical imaging and clinical translations. The linear ultrasonic transducer array is relatively low cost, commercially available with a wide bandwidth selection and convenient to use thanks to the hand-held operation [16, 20, 21]. One can easily convert the pre-clinical or clinical ultrasound imaging machines into LA-PACT by adding a laser excitation source, and then it provides both ultrasonic and optical contrasts. LA-PACT (1–5 MHz frequency range) has imaged tissue deep to 7 cm [22]. A key drawback of the LA-PACT is the limited detection view, which could result in missing detecting features that are perpendicular to the linear array. We can ameliorate this problem with the engineering described in Chapter III [23].

Spatial resolution of PACT with an ideal full-view detection configuration is bandwidth limited. Assuming that a system has a rectangular-shaped bandwidth with a cutoff frequency f_c, the corresponding point spread function (PSF) can be expressed by

$$PSF(R) = \frac{k_c^3}{2\pi^2}\frac{j_1(k_cR)}{k_cR}, \tag{1}$$

where R is the radial coordinate from the point of observation, $k_c = \frac{2\pi f_c}{v_s} = \frac{2\pi}{\lambda_c}$, λ_c is the corresponding wavelength at the cutoff frequency, j_1 is the spherical Bessel function of the first kind. The full width at half maximum (FWHM) of the PSF is typically used to quantify the spatial resolution. It can be obtained that $\frac{3j_1(x)}{x} = 0.5$, when $x = 2.5$. Then the FWHM can be computed as

$$W_{\mathrm{FWHM}} = 2 \times \frac{2.5}{k_c} = 2 \times \frac{2.5}{2\pi} \lambda_c \approx 0.8\lambda_c, \tag{2}$$

For the planar and spherical geometry, the resolutions are nearly isotropic at the center of the field of view, which we can estimate using Eq. (2). For the linear and circular geometry, the axial and lateral resolutions in the imaging plane can be derived from Eq. (2). And the elevational resolution for linear and circular geometry, determined typically by cylindrical acoustic focusing, can be written as

$$FWHM_{\mathrm{ele}} \approx \frac{0.71\lambda_0}{NA}, \tag{3}$$

where λ_0 is the central acoustic wavelength, NA is the numerical aperture of the acoustic lens. Typically, the NA of the acoustic lens is small (~0.1–0.2) to offer large enough depth of focus. Thus, the elevational resolution for linear and circular geometry is worse than the in-plane resolution.

Dissertation outline

In Chapter II, I described a stand-alone single-impulse photoacoustic computed tomography (SIP-PACT) along with advanced reconstruction algorithm that provides high spatiotemporal resolution (125-µm in-plane resolution, 50 µs / frame data acquisition and 50-Hz frame rate), deep penetration (48-mm cross-sectional width *in vivo*), anatomical, dynamical and functional contrasts, and full-view fidelity [4].

In Chapter III, I reported a high-resolution PACT (HR-PACT) system equipped with a high frequency linear transducer array for mapping the microvascular network of a whole mouse brain with the skull intact and studying its hemodynamic activities [23]. The linear array was scanned in the coronal plane to collect data from different angles, and full-view images were synthesized from the limited-view images in which vessels were only partially revealed. We investigated spontaneous neural activities in the deep brain by monitoring the concentration of hemoglobin in the blood vessels and observed strong interhemispherical correlations between several chosen functional regions, both in the cortical layer and in the deep regions.

We also studied neural activities during an epileptic seizure and observed the epileptic wave spreading around the injection site and the wave propagating in the opposite hemisphere.

In Chapter IV, I applied the constructed PACT systems for multi-contrast imaging of endogenous contrasts. Multi-contrast PACT has monitored whole-body and whole-brain hemodynamic responses based on the oxy- and deoxy-hemoglobin contrasts [4]. Multi-contrast PACT imaged whole brain structures based on the cytochrome and lipid contrasts [24]. Multi-contrast PACT also tracked circulating tumor cells based on the melanin contrast [4].

In Chapter V the constructed PACT systems were applied for multi-contrast imaging of exogenous contrasts. From the contrast of organic near infrared (NIR) dyes, multi-contrast PACT has visualized the process of dye perfusion in the mouse wholebody [4], and tracked flowing single dyed droplets for localization-based superresolution imaging [25]. From the contrast of metallic microrobots, multi-contrast PACT has monitored the migration of ingestible microrobotic capsules in the intestines *in vivo*. The combination of PACT with efficient reversibly switchable phytochrome photoswitching significantly enhanced the detection sensitivity and improved specificity [26]. The combination of the protein development and the decay analysis has successfully addressed the impact of unknown local fluence and enabled quantitative cell classification at depths [27]. A split version of the photochromic protein has permitted PA detection of protein-protein interactions in deep-seated tumors. I have also utilized the photochromic behaviors to guide photons to form an optical focus inside live tissue [27].

All experimental procedures in this dissertation were carried out in conformity with laboratory animal protocols approved by the Animal Studies Committee at Washington University in St. Louis and the Institutional Animal Care and Use Committee at California Institute of Technology.

Chapter 2

SINGLE-IMPULSE PANORAMIC PACT (SIP-PACT)

Introduction and motivation

Small animals, especially rodents, are essential models for preclinical studies, and they play an important role in modeling human physiology and development, and in guiding the study of human diseases and in seeking effective treatment [2]. The ability to directly visualize dynamics with high spatiotemporal resolution in these small-animal models at the whole-body scale provides insights into biological processes at the whole organism level [28]. In addition to high spatiotemporal resolution, the ideal non-invasive small-animal imaging technique should provide deep penetration, and anatomical and functional contrasts. Previously, small-animal whole-body imaging has typically relied on non-optical approaches, including magnetic resonance imaging (MRI), X-ray computed tomography (X-ray CT), positron emission tomography (PET) or single-photon emission computed tomography (SPECT), and ultrasound tomography (UST) [29, 30]. Although these techniques provide deep penetration, they suffer from significant limitations. For example, adapting MRI to achieve microscopic resolution requires a costly high magnetic field and a long data acquisition time, ranging from seconds to minutes, too slow for imaging dynamics [31, 32]. X-ray CT lacks functional contrast [33]. PET/SPECT alone suffers from poor spatial resolution. In addition, X-ray CT and PET/SPECT use ionizing radiation, which may inhibit longitudinal monitoring [34]. UST does not image blood oxygenation or extravascular molecular contrasts [35]. To overcome all of the above limitations using one system, we need to develop new imaging modalities.

Optical imaging of biological tissue employs non-carcinogenic electromagnetic waves to provide extraordinary structural, functional, and molecular contrasts with either endogenous or exogenous agents [36-38]. Unfortunately, the strong optical scattering of tissue impedes the application of conventional optical imaging technologies to small-animal whole-body imaging, which prevents high-resolution imaging beyond the optical diffusion limit of ~1–2 mm in depth [29]. Although diffusive optical imaging methods, such as fluorescence diffuse optical tomography [39], can provide centimeters of penetration, their image resolution is rather poor, approximately 1/3 of the depth.

To date, photoacoustic tomography (PAT) is the only high-resolution optical imaging modality that breaks the optical diffusion limit [40]. In PAT, the energy of incident photons is absorbed by chromophores inside the tissue to be imaged and re-emitted as ultrasonic waves. The ultrasonic waves are subsequently detected to generate tomographic images with optical contrasts. Thanks to the weak scattering of ultrasound in soft tissue (about three orders of magnitude weaker than light scattering on a per unit path length basis in the ultrasonic frequency of interest), PAT enjoys superb resolution at depths, with a depth-to-resolution ratio of ~200 [3]. Combining the advantages of optical contrasts and acoustic detection, PAT holds great promise for a full-package solution of small-animal whole-body imaging. We have demonstrated high-speed, high-resolution functional PAM of the mouse brain in action, with penetration up to several millimeters [41]. PACT has provided penetration beyond 10 mm, but with either poor temporal resolution, due to data acquisition multiplexing [26, 42, 43], or unclearly resolved sub-organ features, due either to partial acoustic detection coverage [44, 45] or to sparse spatial sampling [46-48]. For high-performance small-animal whole-body imaging, we need to simultaneously integrate high spatiotemporal resolution, deep penetration, multiple contrasts, full-view fidelity, and high detection sensitivity in one system.

Here, we report a significant advance in PACT technology that overcomes all the above-mentioned limitations prevalent in both non-optical and pure optical imaging techniques. Our imaging technology, called single-impulse panoramic PACT (SIP-PACT), allows us to capture structural, functional, cellular, and molecular small-animal whole-body images with unprecedented speed and quality [4].

Methods

System construction and laser configuration

SIP-PACT employed a 512-element full-ring ultrasonic transducer array (Imasonic, Inc., 50-mm ring radius, 5-MHz central frequency, more than 90% one-way bandwidth, **Fig. 2**) for 2D panoramic acoustic detection. Each element has a cylindrical focus (0.2 NA, 20-mm element elevation size, 0.61-mm pitch, 0.1-mm inter-element spacing). A lab-made 512-channel pre-amplifier (26-dB gain) was directly connected to the ultrasonic transducer array housing, with minimized connection cable length to reduce cable noise. The pre-amplified PA signals were digitized by a 512-channel data acquisition (DAQ) system (four SonixDAQs, Ultrasonix Medical ULC, 128 channels each, 40-MHz sampling rate, 12-bit dynamic range) with programmable amplification up to 51 dB. The digitized radio frequency (RF) data were first stored in the onboard buffer then transferred to a computer through USB 2.0. A single laser pulse, sufficiently short to be treated as an impulse, excites PA waves, which are detected within 50 µs for 2D imaging of a cross-section. The 2D panoramic acoustic detection scheme provides 125-µm isotropic in-plane resolution within a field of view (FOV) of ~16 mm in diameter, and full-view fidelity (i.e., no partial-view artifacts) [49].

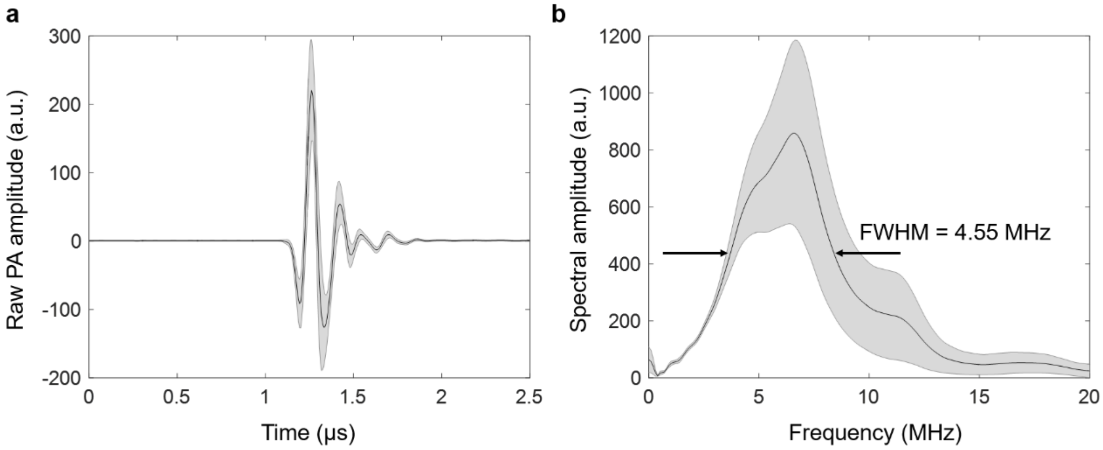

Figure 2. The electrical impulse response (EIR) of the SIP-PACT system. (a) The raw radio frequency (RF) signal from each ultrasonic transducer element corresponding to a point PA source at the center of the full-ring array. The black solid line represents the mean value of all transducer elements' responses, and the gray region represents the standard deviation across the elements. (b) Fourier transform amplitude of each RF signal in (a), showing the bandwidth of the transducer array is about 4.55 MHz. The black solid line represents the

mean value of the spectral amplitude of all RF signals, and the gray region represents the standard deviation across the elements.

For whole-body imaging illumination, a 1064-nm laser beam (DLS9050, Continuum, 50-Hz pulse repetition rate, 5–9-ns pulse width) or a 720-nm laser beam (LS-2145-LT-150, Symphotic Tii, 20-Hz pulse repetition rate, 12-ns pulse width) was first homogenized and expanded by an engineered diffuser (EDC-10-A-1r, RPC Photonics). The laser beam then passed through a conical lens (AX-FS-1-140-0, Del Mar Photonics) to form a ring-shaped light pattern, and re-focused by a lab-made optical condenser. The incident light formed a ring pattern on the trunk of the mouse, with the illuminated area located within the transducer's elevational focal zone. For brain imaging illumination, the excitation beam was uniformly shined on the cortex after passing through the engineered diffuser. The laser fluence (8 mJ cm^{-2}) at 630 nm, 680 nm, and 720 nm was within the American National Standards Institute (ANSI) safety limits for laser exposure (20 mJ cm^{-2} at 630 nm and 680 nm, and 40 mJ cm^{-2} at 720 nm, at a 10-Hz pulse repetition rate). The laser fluence in mouse and rat brain imaging, and in mouse trunk imaging, was ~18 mJ cm^{-2} at 1064 nm, with a 50-Hz pulse repetition rate, which is below the ANSI safety limit (at 1064 nm: 100 mJ cm^{-2} at a 10-Hz pulse repetition rate, or 1 W cm^{-2}). During the rat trunk imaging, the excitation fluence was ~38 mJ cm^{-2}at 1064 nm, with a 50-Hz pulse repetition rate, which is above the ANSI limit. The rats were monitored periodically after imaging, and no skin damage was found.

Two different illumination approaches have been applied respectively for imaging the mouse brain cortex and trunk (**Fig. 3**). Top illumination and side detection are used for brain cortex imaging, and full-ring side illumination and side detection (aligned confocally to maximize detection sensitivity) are used for trunk imaging.

For two-wavelength imaging, such as in the brain oxygen saturation (sO_2) mapping experiment (see details in Chapter V, two lasers were synchronized by a control card (sbRIO-9626, National Instruments). The Q-switch trigger of each laser was set at a fixed delay of 50 µs, thus one laser fired 50 µs later than the other. Since the pulses at each of the two wavelengths were delayed by only 50 µs, during which time the object was relatively stationary in terms of most biological activities, we call the illumination essentially simultaneous.

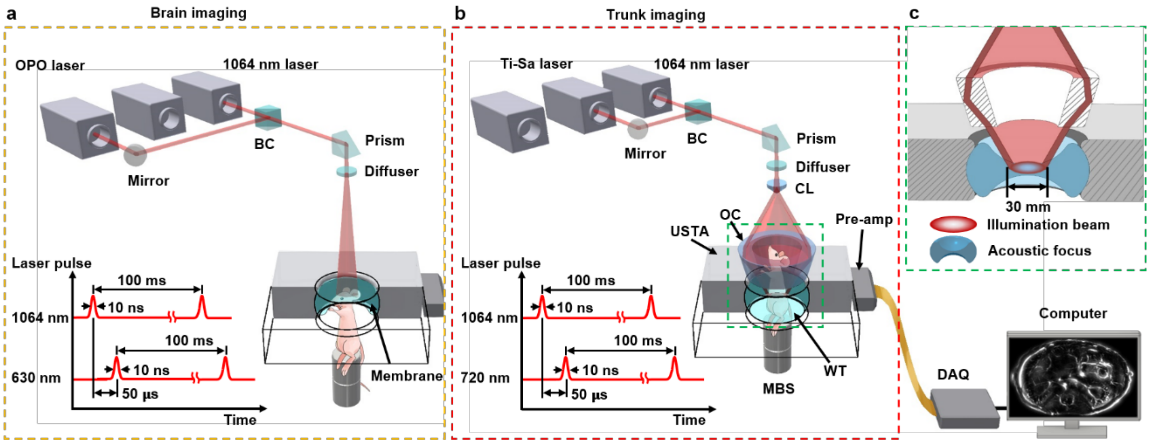
a
Brain imaging
OPO laser
1064 nm laser
BC
Mirror
Prism
Diffuser
Laser pulse
100 ms
10 ns
1064 nm
100 ms
10 ns
630 nm
50 μs
Time
Membrane
b
Trunk imaging
Ti-Sa laser
1064 nm laser
Mirror
BC
Prism
Diffuser
CL
OC
USTA
Pre-amp
Laser pulse
100 ms
10 ns
1064 nm
100 ms
10 ns
720 nm
50 μs
Time
MBS
WT
c
30 mm
Illumination beam
Acoustic focus
Computer
DAQ

Figure 3. Schematics of the SIP-PACT system for (a) brain and (b) trunk imaging. During dual-wavelength illumination, all lasers fire at 10 Hz and the delay time between the dual-pulse is 50 μs. For single-wavelength illumination, the 1064-nm laser fires at 50 Hz and the Ti: Sapphire (Ti-Sa) laser fires at 20 Hz. BC, beam combiner; CL, conical lens; MBS, magnetic base scanner; OC, optical condenser; USTA, (full-ring) ultrasonic transducer array; WT, water tank. (c) Close up of the green dashed box region in (b), which shows the confocal design of light delivery and PA wave detection.

Half-time, dual-speed-of-sound PA reconstruction

Moreover, to better reveal detailed features inside the body, we developed a half-time dual-speed-of-sound (SOS) universal back-projection (UBP) algorithm to compensate for the first-order effect of acoustic inhomogeneity.

Conventional half-time UBP assumes a uniform SOS to calculate the PA signal delay necessary for the reconstruction. In real applications, however, the heterogeneous acoustic properties of the substances within the elevational focal plane render the uniform SOS assumption problematic. Consequently, the resulting images always suffer from artifacts that cannot be removed or alleviated by image processing techniques, such as deconvolution. In the case of whole-body imaging, at a given elevational position, breakdown of the uniform SOS assumption mainly results from the dramatic acoustic property difference between the biological tissue and the surrounding fluid (in our case, water), whereas the SOS differences among different tissue types cause only second-order effects. For example, at room temperature, the SOS of water, the liver, and the kidney are 1480 m s^{-1}, 1590 m s^{-1}, and 1570 m s^{-1}, respectively [49].

We numerically simulated the problem in 2D, using a circular numerical phantom with a radius of 13 mm and a uniform speed of sound of 1520 m s^{-1}. The phantom was surrounded by water with an SOS of 1480 m s^{-1}, and the whole region was bounded by a ring-shaped detector array with a radius of 50 mm. The phantom and the ring array were located concentrically, as shown in **Fig.4a**. Within the phantom, an optical absorption pattern representing a leaf skeleton was used (**Fig. 4b**). We used the k-Wave toolbox to generate PA data [50], and reconstructed images using half-time UBP with single and dual SOS. We compared the images reconstructed using a single uniform SOS (**Fig**. **4c**) and the correct (**Fig**. **4d**) dual-SOS map. Clearly, a single SOS reconstruction introduces splitting or fringing artifacts in the image (**Fig**. **4c**, inset zoomed-in view).

To date, many methods have been developed to solve the problem caused by SOS heterogeneity. These methods either rely on iterative SOS corrections [51-54] or use additional hardware and software to measure the SOS map [55]. Both types of approaches dramatically increase the complexity of signal demodulation and image reconstruction. Here, to improve the image quality, we used a method that imposes no additional computational cost. The key is to correct the first-order errors only. In doing so, we segment the entire region into two zones: a tissue zone and a water zone. We assume that the SOS is uniform within each zone, but is different across the zones. To further simplify the problem, we make the following two assumptions. First, the cross section of the mouse body is approximated by an ellipse characterized by its center position (x_0, y_0) and the lengths of its major and minor radii (R_x, R_y). Second, refraction at the boundary of the two zones is negligible. In other words, rays travel straight from the field point (x_s, y_s) to a detector (x_d, y_d). The second assumption is sufficiently accurate, according to a simple geometrical analysis [49].

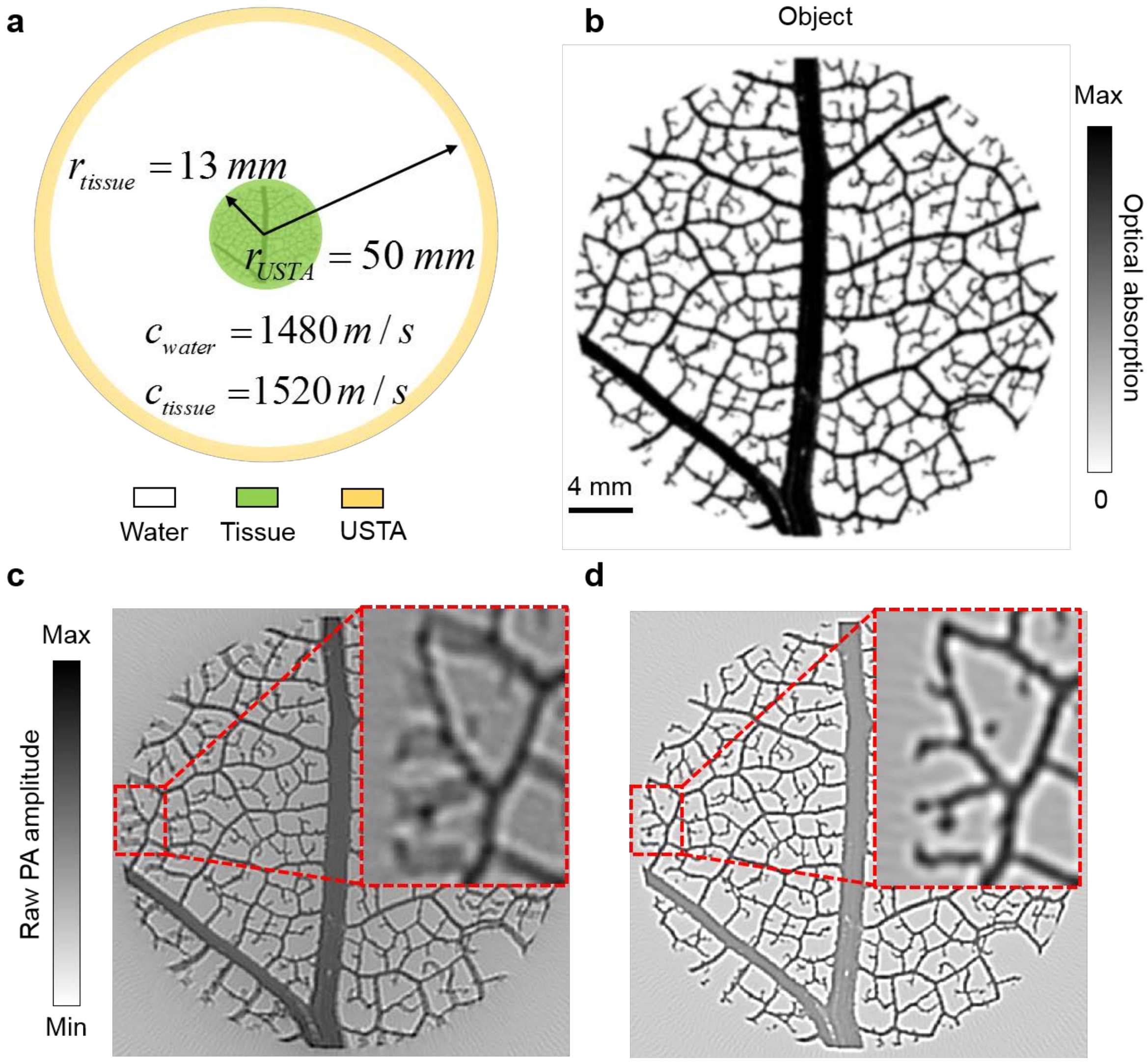
a
$r_{tissue} = 13\ mm$
$r_{USTA} = 50\ mm$
$c_{water} = 1480\ m/s$
$c_{tissue} = 1520\ m/s$
Water
Tissue
USTA
b
Object
Max
Optical absorption
0
4 mm
c
Max
Raw PA amplitude
Min
d

Figure 4. Numerical simulation results of dual-SOS reconstruction, forward data is generated by the k-Wave toolbox (http://www.k-wave.org/). (a) Schematic of the simulation. (b) The optical absorption distribution of the numerical phantom. Reconstructed images using universal back projection based on (c) single speed with v = 1489.8 m s^{-1} and (d) dual speed with v_1 = 1480 m s^{-1} (in water) and v_2 = 1520 m s^{-1} (in

tissue), where the close-up insets show the splitting artifacts due to the mismatched speed of sound.

Using these assumptions, we can calculate the sound propagation delay between any source-detector pairs given the SOS in the body (v_1) and water (v_2), (**Fig. 5a**). It should note that if a series of images are taken at, or close to, a fixed elevational position, the delay map is calculated only once before reconstruction. Subsequently, we can use the delay map generated by the dual-speed assumption to reconstruct images with no additional computational cost. In **Fig. 5b**, we illustrate the gross localization error produced by the single-speed assumption. In the calculation, we assumed that $R_x = R_y = 10$ mm, $x_0 = y_0 = 0$, and $v_1 = 1570$ m s^{-1}, $v_2 = 1506$ m s^{-1}, and $R_d = 50$ mm. The PA signal generated by a point source, located at the position labeled by a red star in **Fig. 5b**, was back-projected along the direction piercing the source and the detector. The reconstructed position of the point source, according to the single-speed assumption, scatters around the correct position, depending on the azimuthal angle of the transducer. A splitting as large as 0.4 mm is observed. In **Fig. 5c** and **5d**, we compare the images of the liver region of a mouse reconstructed using half-time single-speed (**Fig. 5c**) and half-time dual-speed (**Fig. 5d**) UBP approaches. **Figure. 5c** shows many artifacts, including the horseshoe-shaped features on the body surface (which are shown as blood vessels perpendicular to the image plane in **Fig. 5d**), and splitting of the vasculature in the upper-left and lower-right regions of the body. These artifacts are completely removed by the dual-speed reconstruction, as shown in **Fig. 5d**. The acquired data was reconstructed off-line using the half-time dual-speed-of-sound universal back-projection method, and it takes ~0.1 s to reconstruct one frame with 400 × 400 pixels using intel i7 CPU, which can be further accelerated by GPU parallel computing.

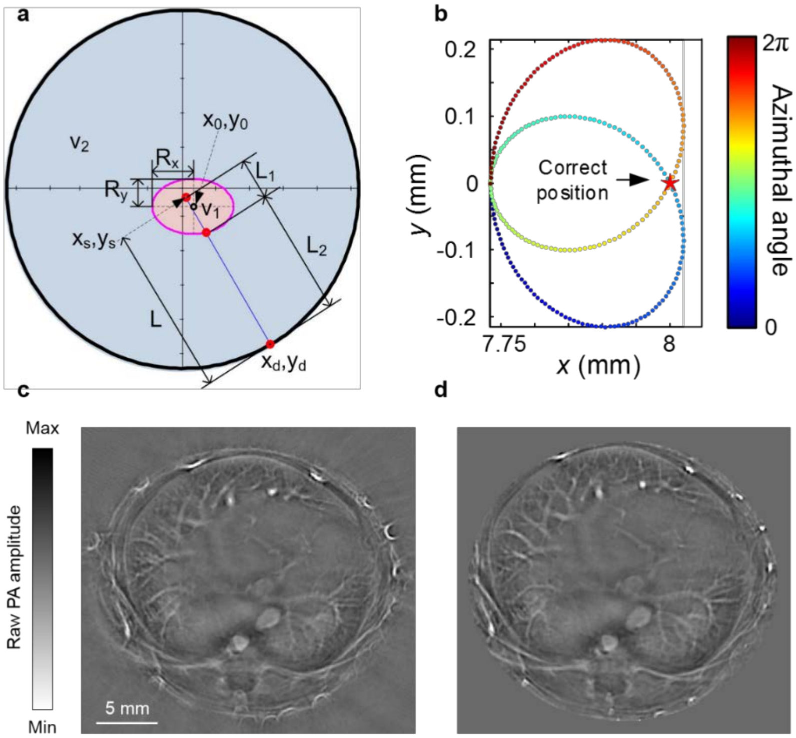
a
x_0,y_0
v_2
R_x
R_y
L_1
v_1
x_s,y_s
L_2
L
x_d,y_d
b
0.2
0.1
0
-0.1
-0.2
y (mm)
7.75
8
x (mm)
Correct position
2π
Azimuthal angle
0
c
d
Max
Raw PA amplitude
Min
5 mm

Figure 5. Image quality improvement by dual-SOS reconstruction. (a) Definition of parameters used in half-time dual-speed-of-sound universal back projection. (b) Position of a point source back-projected using single-speed reconstruction. Color represents the in-plane azimuthal angle of the transducer array. In the calculation, $R_x = R_y = 10$ mm, $x_0 = y_0 = 0$, $v_1 = 1.570$ m s^{-1} (in tissue), $v_2 = 1.506$ m s^{-1} (in water), and $R_d = 50$ mm. The correct position of the point source is labeled by the red star. (c) and (d) *In vivo* images of a cross-section of a mouse trunk (liver) reconstructed using half-time universal back projection based on (c) single speed with $v = 1.520$ m s^{-1} and (d) dual speed with $v_1 = 1.590$ m s^{-1} (in tissue) and $v_2 = 1.507$ m s^{-1} (in water).

Results and discussion

Label-free imaging of small-animal whole-body anatomy and dynamics

SIP-PACT non-invasively imaged the vasculature of the brain cortex (**Fig. 6a**) and the anatomy of the internal organs within the thoracic cavity (heart, lungs; **Fig. 6b** and **6c**) and the abdominal cavity (liver, spleen, kidney, cecum, and intestine; **Fig. 6**, **d** to **f**), with detailed structures revealed by hemoglobin contrast.

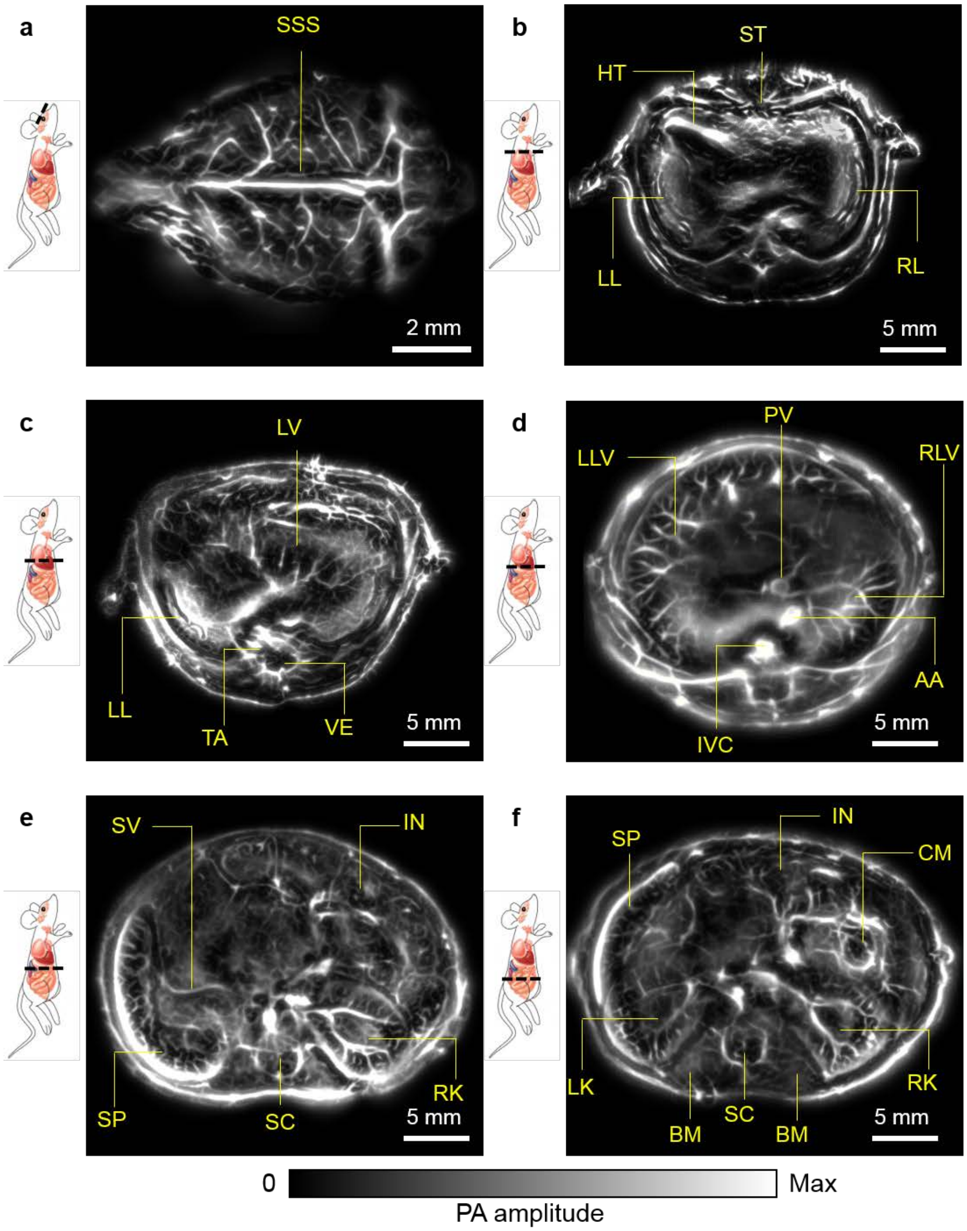
a
SSS
2 mm
b
ST
HT
LL
RL
5 mm
c
LV
LL
TA
VE
5 mm
d
PV
LLV
RLV
AA
IVC
5 mm
e
SV
IN
SP
SC
RK
5 mm
f
IN
SP
CM
LK
BM
SC
BM
RK
5 mm
0
Max
PA amplitude

Figure 6. Label-free SIP-PACT of small-animal whole-body anatomy from the brain to the trunk. (a) Vasculature of the brain cortex; SSS, superior sagittal sinus. (b) Cross-sectional image of the upper thoracic cavity; HT, heart; LL, left lung; RL, right lung; ST, sternum. (c) Cross-sectional image of lower thoracic cavity; LV, liver; TA, thoracic aorta; VE, vertebra. (d) Cross-sectional image of two lobes of liver; AA, abdominal aorta; IVC, inferior vena cava; LLV, left lobe of liver; PV, portal vein; RLV, right lobe of liver. (e)

Cross-sectional image of upper abdominal cavity; IN, intestines; SC, spinal cord; SP, spleen; SV, splenic vein. (f) Cross-sectional imaging of lower abdominal cavity; BM, backbone muscles; CM, cecum; LK, left kidney; RK, right kidney.

As with many other tomographic imaging modalities, after scanning the animal vertically through the confocal plane and stacking the slices of cross-sectional images, we can compile a three-dimensional (3D) tomogram of the mouse trunk.

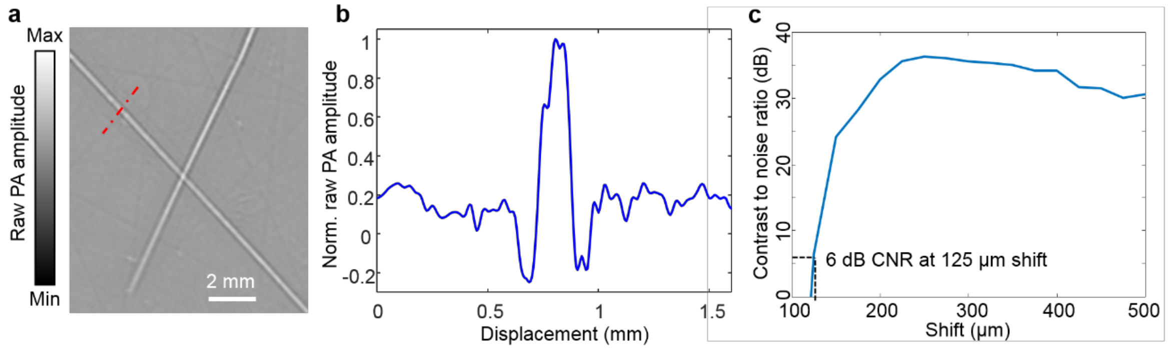

Figure 7. Quantification of the in-plane resolution of the SIP-PACT. (a) An image of two crossed tungsten wires, each with a nominal diameter of 50 μm. (b) The PA amplitude distribution along the red dash-dot line in (a). (c) The contrast-to-noise ratio (CNR) versus the shift in the sum of the original line profile shown in (b) and the shifted one. The in-plane resolution, defined as the shift corresponding to 6-dB CNR, is 125 μm.

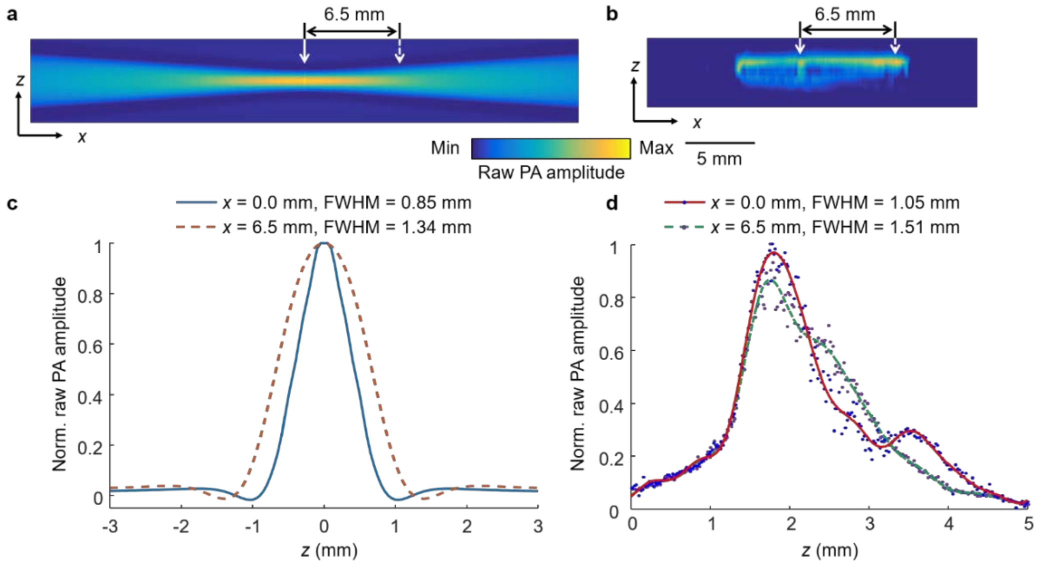

Figure 8. Quantification of elevational resolution of SIP-PACT. (a) Simulated acoustic focus field in the *x*-*z* plane. (b) The PA image of a tungsten wire with a nominal diameter of 50 μm, projected on the *x*-*z* plane. (c) The simulated line profiles of (a) at the center of

the ring (indicated in (a) by the solid white arrow) and at 6.5 mm (off-center, indicated in (a) by the dashed white arrow). (d), as (c), but showing the measured line profiles of (b).

The thickest section of the mouse trunk had a width of 28 mm (**Fig. 6e** and **6f**), and the entire cross-section was clearly imaged with a spatial resolution of 125 µm (**Figs**. **7** and **8**). At an imaging frame rate of 50 Hz, respiratory motions and heartbeats were fully captured at well above the Nyquist sampling rate. The substantially improved system performance and whole-body image quality enable SIP-PACT to complement other small-animal whole-body anatomical imaging modalities.

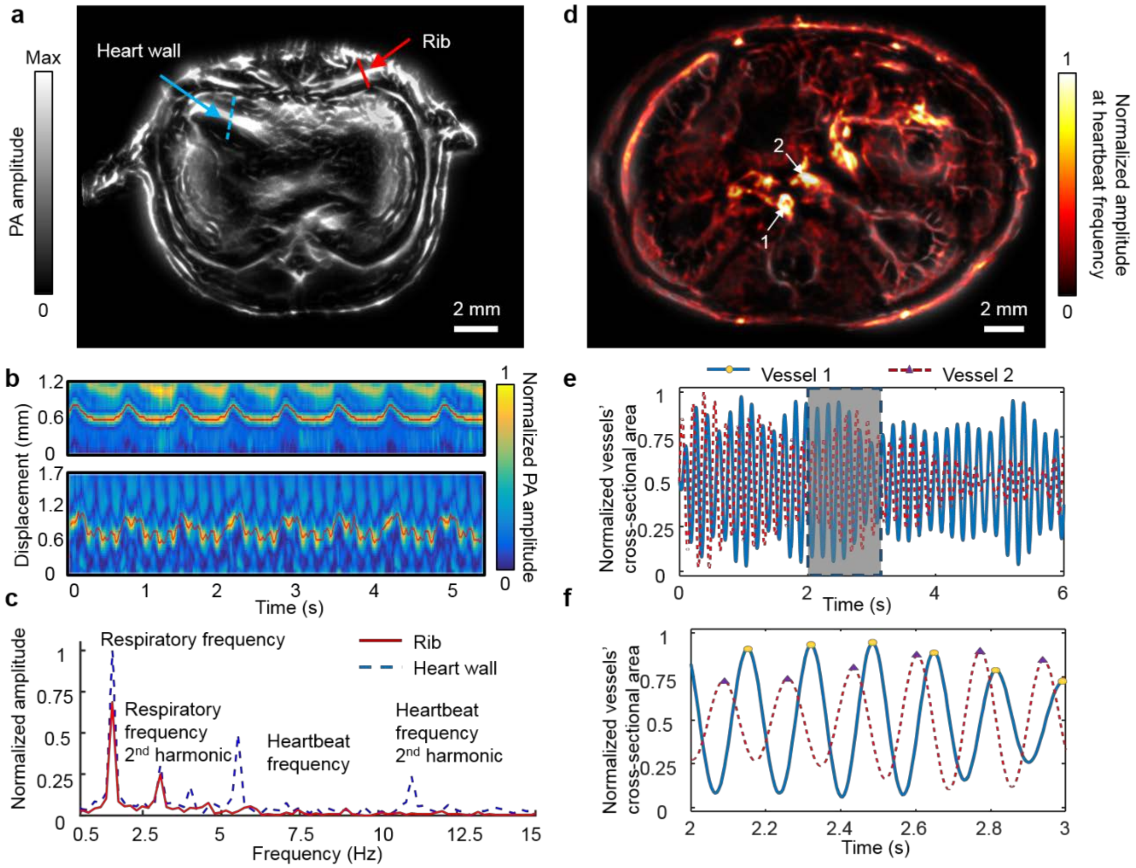
a
Max
PA amplitude
0
Heart wall
Rib
2 mm
d
1
Normalized amplitude at heartbeat frequency
0
2
1
2 mm
b
1.2
0.6
0
1.7
1.2
0.6
0
Displacement (mm)
0
1
2
3
4
5
Time (s)
1
Normalized PA amplitude
0
e
Vessel 1
Vessel 2
Normalized vessels' cross-sectional area
1
0.75
0.5
0.25
0
0
2
4
6
Time (s)
c
Normalized amplitude
Respiratory frequency
Rib
Heart wall
Respiratory frequency 2nd harmonic
Heartbeat frequency
Heartbeat frequency 2nd harmonic
1
0.75
0.5
0.25
0
0.5
2.5
5
7.5
10
12.5
15
Frequency (Hz)
f
Normalized vessels' cross-sectional area
1
0.75
0.5
0.25
0
2
2.2
2.4
2.6
2.8
3
Time (s)

Figure 9. Label-free imaging of small-animal whole-body dynamics. (a) Cross-sectional image of the upper thoracic cavity, where the red solid line crosses a rib, and the blue dashed line crosses the heart wall. (b) Line profiles in (a) versus time show the displacements of (upper panel) the rib during respiration and (lower panel) the heart wall during heartbeats. The traces of the rib and heart wall movements are identified and highlighted with solid red lines. (c) Fourier transforms of the rib and heart wall movements showing the respiratory frequency and heartbeat frequency, respectively. (d) Heartbeat encoded arterial network mapping overlaid on the anatomical image. (e) Cross-sections of the vessels highlighted by arrows in (d), showing changes associated with arterial pulse

propagation. (f) A zoomed-in of the dashed box in (e) shows the relative phase delay between the two curves of the vessels' cross sections.

One cross-sectional image of the thoracic cavity (**Fig. 6b** and **Fig. 9a**) displays both respiratory motion and heartbeats. By recording the signal changes of a rib (along the red solid line in **Fig. 9a**) and the heart wall (along the blue dashed line in **Fig. 9a**), we can identify and track the respiratory motion and heartbeats (**Fig. 9b**). Fourier analysis shows that the motion of the rib repeated at a respiratory frequency of ~1 Hz, and the motion of the heart wall repeated at both the respiratory frequency and a heartbeat frequency of ~5.2 Hz (**Fig. 9c**) and **Fig. 10**).

Within a cross-sectional view of lower abdominal cavity, the signals from arteries are temporally correlated due to their direct connection to the heart. The high imaging speed and the single-impulse acquisition capability of SIP-PACT enabled us to selectively map the arterial network on the whole-body cross-sectional image. By pixel-wise calculation of the amplitude at the heartbeat frequency, we can map the arterial network on the whole-body cross-sectional image (**Fig. 9d**), where the renal arterial network of the right kidney is highlighted by heartbeat encoding. During systole, the aortic wall dilates due to the ejection of blood from the contracted left ventricle, generating a pressure wave that travels along the arterial tree. We selected two vertically distributed arteries from the arterial network (highlighted by arrows 1 and 2 in **Fig. 9d**) to compute the changes of the cross-sectional areas (**Fig. 9e**). The close-up panel (**Fig. 9f**) reveals a steady phase delay, indicating that the changes of the cross-sectional areas are the results of the pulse wave propagating through the arterial network. This demonstrates that SIP-PACT can noninvasively map the whole-body arterial network and measure the relative pulse wave phase difference between arteries. This capability could provide a non-invasive and direct diagnostic tool for chronic coronary artery disease and chronic renal disease [56, 57].

In addition, the measurements of breathing motion and heartbeats also were validated by the pressure sensor and electrocardiography (**Fig. 10**).

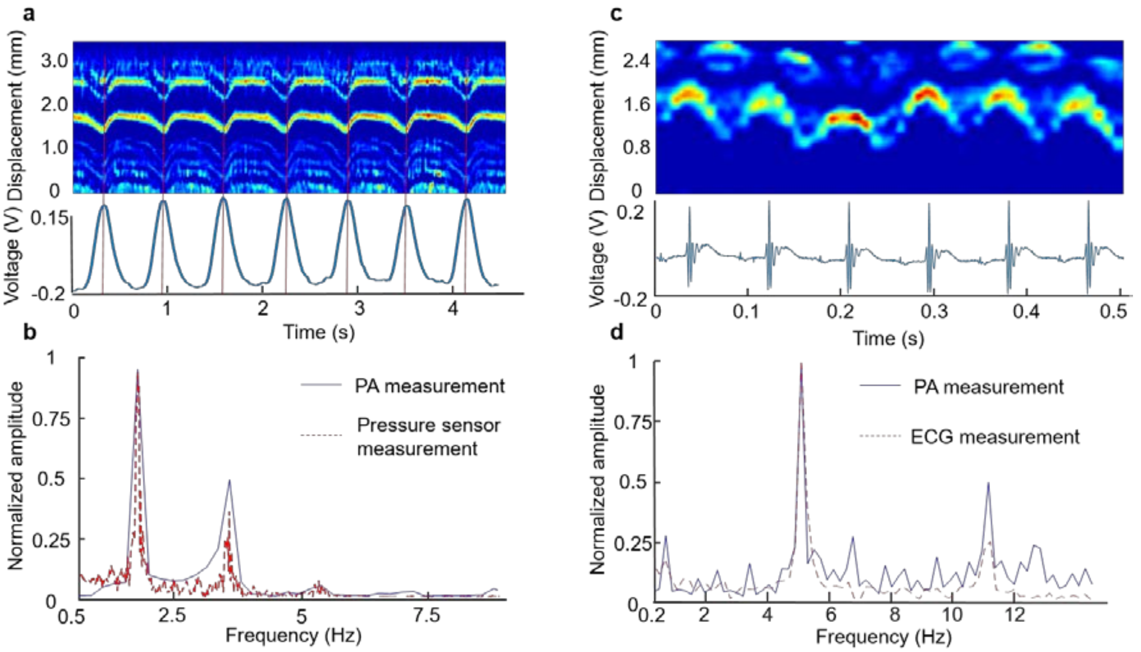

Figure 10. Validation of the SIP-PACT measurement of breathing motion and heartbeats. The pressure sensor and electrocardiography (ECG) measurement were conducted in parallel with the SIP-PACT imaging on the same mouse. (a) Co-registered measurement of breathing motion from SIP-PACT (top) and the pressure sensor (bottom). (b) Fourier transform of (a), which shows the identical respiratory frequency measured by SIP-PACT and the pressure sensor. (c) Co-registered measurement of heartbeats from SIP-PACT (top) and ECG (bottom). (d) Fourier transform of (b), which shows the identical heartbeat frequency measured by SIP-PACT and ECG.

Deep imaging through rat whole brain and whole body

Revealing how our brain works is a great challenge that merits our every effort: It will not only illuminate the profound mysteries in science but also provide the key to understanding and treating neurological diseases such as Alzheimer's and Parkinson's. To date, most deep brain functional studies have been based on functional MRI (fMRI) or power Doppler ultrasound (fUS), and optically imaging through even a mouse brain (~6 mm in depth) with reasonable spatiotemporal resolution and contrast is still a hurdle. In this study, we used SIP-PACT to see through a rat's whole brain. As shown in **Fig. 11**, the rat head was mounted vertically and the light was obliquely delivered to the rat cortex. A cranial window was opened to maximize the acoustic transmission. Taking advantage of the deep penetration of 1064-nm light, the full-view acoustic coverage and high detection sensitivity of SIP-PACT, a coronal view of the rat whole brain (11 mm in depth) was produced with detailed vasculature (**Fig. 12a**).

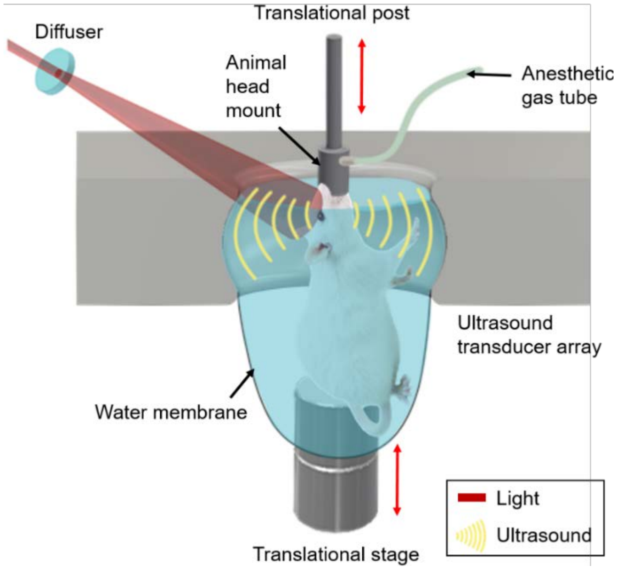

Figure 11. Setup for rat brain imaging. The rat head was mounted vertically during imaging and the light was obliquely delivered to the rat cortex.

The brain serves as the center of the nervous system, dynamically coordinating responses through the functional network. The intrinsic functional connectivity (FC) across spatially separated brain regions can be measured through regionally correlated, spontaneous, low frequency (0.01–0.1 Hz) fluctuations in blood oxygenation level dependent (BOLD) signals with fMRI, particularly during resting-state/task-free periods (resting-state fMRI or rsfMRI). Similar to fMRI, SIP-PACT can also globally monitor the brain hemodynamics with appropriate spatiotemporal resolution and penetration. To detect the FC, we measured and compared the spontaneous hemodynamic responses between contralateral regions of the rat brain. We measured the FC of the rat whole brain in the coronal plane (~bregma -2.16 mm), where we identified 16 functional regions (labeled in **Fig. 12b**) and computed the correlation coefficients of every pair. We also employed a seed-based method to study the FC (**Fig. 12c**). The results (**Fig. 12d**) show clear correlation between corresponding regions across the left and right hemispheres, as well as correlation between neighboring regions in the neocortex. These findings are consistent with previous research in both fMRI and fUS [58, 59]. Most interestingly, we identified the left-right correlation between the deep thalamus regions (9.7 mm in depth, **Fig. 12c**, bottom row), which, to our best knowledge, has not been demonstrated at this spatial resolution. Our FC observation demonstrates the potential of SIP-PACT as a high-resolution imaging tool for studying deep brain functions in rats, which was previously difficult to accomplish using optical contrast, and, therefore underexplored.

To further validate the deep penetration, an adult rat with a trunk (abdominal region) width of 48 mm was also imaged by SIP-PACT using side illumination. As shown in **Fig. 12e** and **12f**, the internal organs, such as the left and right lobes of the liver, the kidneys, the spleen, the intestine, and supply vessels, are clearly revealed.

Outlook

SIP-PACT enables a number of new whole-body imaging capabilities, with performance complementary to those of the above-mentioned non-optical approaches. At a 50-Hz frame rate, it non-invasively images whole-body small animals, with sub-organ vasculature and internal organ structures clearly resolved, without any labeling. At such high spatiotemporal resolutions, the biological dynamics associated with heartbeats and respiration are clearly observed without motion artifacts. Such a capability makes possible the direct diagnosis of pathological changes of internal organs. As a result, our technology opens a new window for medical researchers to test drugs and monitor longitudinal therapy, without the harm from ionizing radiation in X-ray CT, PET or SPECT. Aortic pulse wave measurement and analysis have been widely used to study cardiovascular diseases in both clinical and preclinical research [56, 57]. With a frame rate of 50 Hz, SIP-PACT reveals whole-body cardiac related dynamics and selectively maps the whole-body arterial network in mice. Relatively steady phase delays between arteries within internal organs can also be computed, which indicate changes in the cross-sectional areas resulting from pulse wave propagation through the arterial network. Thus, the capability of mapping the arterial network and the relative phase delay distribution within each cross-section enables SIP-PACT to be a potential non-invasive tool for direct diagnosis of chronic coronary artery disease and chronic renal vascular disease.

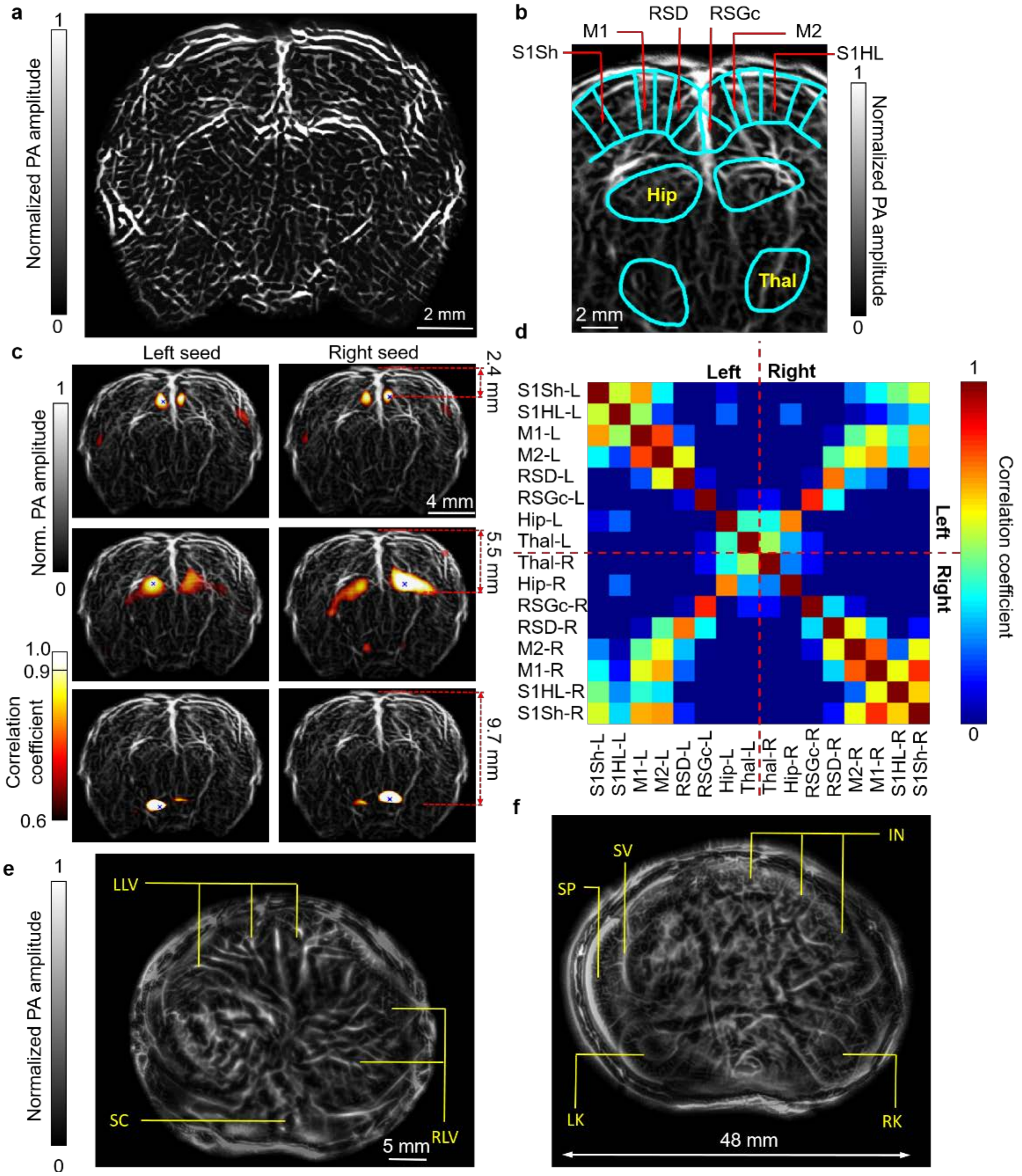
a
1
Normalized PA amplitude
0
2 mm
b
S1Sh
M1
RSD
RSGc
M2
S1HL
Hip
Thal
2 mm
1
Normalized PA amplitude
0
c
Left seed
Right seed
1
Norm. PA amplitude
0
2.4 mm
4 mm
5.5 mm
1.0
0.9
Correlation coefficient
0.6
9.7 mm
d
Left
Right
S1Sh-L
S1HL-L
M1-L
M2-L
RSD-L
RSGc-L
Hip-L
Thal-L
Thal-R
Hip-R
RSGc-R
RSD-R
M2-R
M1-R
S1HL-R
S1Sh-R
Left
Right
1
Correlation coefficient
0
e
1
LLV
Normalized PA amplitude
SC
5 mm
RLV
0
f
SV
SP
IN
LK
RK
48 mm

Figure 12. Deep imaging of rat whole brain functions and whole-body anatomy. (a) Rat whole brain vasculature in the coronal plane. (b) Segmentations of different functional regions of the brain. (c) Seed-based functional connectivity analyses of RSGc (top row), Hippocampus (middle row), and Thalamus (bottom row) regions on both sides of the brain. (d) Correlation matrix of the 16 functional regions labeled in (b). Notice the correlation between left and right hemispheres, as well as the correlation across different regions in the neocortex. S1Sh, primary somatosensory–shoulder region; S1HL, primary somatosensory cortex–hindlimb region; M1, primary motor cortex; M2, secondary motor cortex; RSD, retrosplenial dysgranular cortex; RSGc, retrosplenial granular cortex; Hip, hippocampus;

Thal, thalamus. (e) and (f) Cross-sectional images of a rat wholebody. IN, intestine; LK, left kidney; LLV, left liver; RK, right kidney; RLV, right liver; SC, spinal cord; SP, spleen; SV, splenic vein.

Photoacoustic imaging has already demonstrated its capability of functional brain imaging in rodents with exquisite sensitivity and high resolution at depths beyond the optical diffusion limit [41, 60, 61]. Now SIP-PACT has further extended the functional brain imaging depth to the rat whole brain (~10 mm in depth), which has not been demonstrated with optical contrast and spatiotemporal resolution as fine as SIP-PACT provides. However, to reach the ultimate goal of imaging single neuron action potentials at the whole brain level, great efforts are needed to further improve the spatiotemporal resolution, sensitivity, and voltage-sensitive PA contrast agents.

Chapter 3

LINEAR-ARRAY BASED FULL-VIEW HIGH-RESOLUTION PACT

Introduction and motivation

In recent years, advanced imaging methodologies with increased spatial and temporal resolution have augmented our understanding of brain functions. Optical imaging techniques, such as optical coherence tomography and multiphoton microscopy, have also been demonstrated for imaging neural activity with cellular and subcellular resolution [62, 63], but the shallow penetration limits their observation to only the cortical layer (~1–2 mm). PACT detects ultrasonic waves generated by diffused photons and retrieves the absorption distribution through an inverse algorithm, allowing an imaging depth of up to several centimeters. SIP-PACT, operating at 5 MHz with 1064 nm illumination, has imaged through the rat whole brain. However, the spatial resolution of SIP-PACT is 125 µm, leaving detailed brain features unresolved. In addition, the high-frequency (>15 MHz) versions of the circular array used in SIP-PACT are commercially unavailable. The linear ultrasonic transducer array is relatively low cost, commercially available with a wide bandwidth selection and convenient to use thanks to the hand-held operation. A linear array with 21-MHz central frequency was used to achieve high-resolution imaging of the mouse brain. To eliminate the limited-view issue, the linear array was scanned in the coronal plane to collect signals from different angles, and full-view images were synthesized from the limited-view images in which vessels were only partially revealed [23].

Methods

Figure 13 shows the schematic setup of linear-array based full-view PACT for mouse brain imaging. In this work, 6–8 week-old female mice (Swiss Webster, Invigo) were used. Prior to imaging, the hair on the head of the mouse was removed by a depilatory cream. The mouse was then mounted onto a holder with its head fixed by a nose cone and a tooth bar. A rubber tube connecting the nose cone and an isoflurane vaporizer was used to deliver oxygen and anesthetic gas. The temperature of the mouse holder was regulated by a controller. The scalp of the mouse was removed, and ultrasound gel was applied before imaging. The mouse was placed beneath the water tank, within an imaging window with dimensions of 8 cm × 10 cm. The imaging window was covered with plastic film at the bottom of the water tank, and the tank was filled with water for ultrasound coupling. A 5-cm-wide window in one side of the tank wall allowed laser beam access to the mouse head. The laser beam used for exciting ultrasonic waves was provided by a Nd:YAG laser (Quantel, Brillant B, 4–6 ns pulse duration, 10 Hz repetition rate). The laser beam was expanded and homogenized by an engineered diffuser (EDC-5-A-2 s, RPC Photonics, Inc.), resulting in a 2 cm-diameter illumination area on the mouse head. With a pulse energy of 200 mJ, the optical fluence on the head surface was 64 mJ cm^{-2}, which is below the ANSI safety limit of 100 mJ cm^{-2} at 1064 nm.

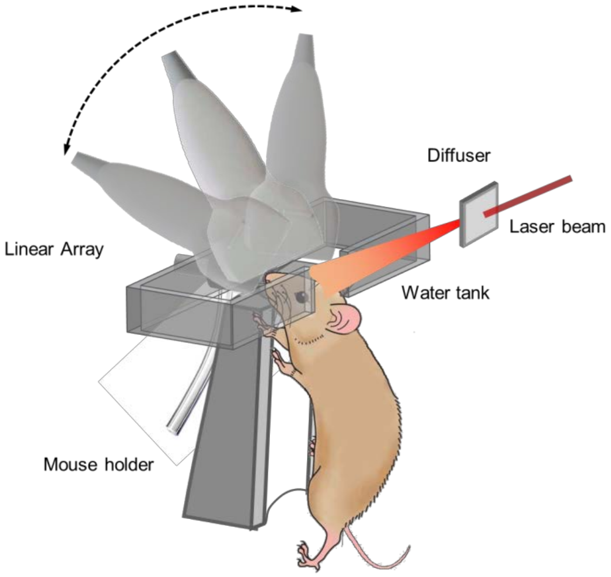

Figure 13 Schematic setup of linear-array based full-view PACT for mouse brain imaging.

The excited PA waves were detected by a focused linear transducer array (LZ250, VisualSonics) consisting of 256 elements. The linear array had a one-way bandwidth of 11 MHz around the central frequency of 21 MHz, providing a lateral resolution of 75 microns. The numerical aperture of the transducer array is 0.1, yielding a sectioning thickness of about 0.5 mm within the depth of focus, which covers the whole mouse brain. The detected signals were first amplified by homemade pre-amplifiers (256 channels, 26 dB gain per channel) and then digitalized by a customized 256-channel data acquisition system (National Instruments, Customized PXI system, 14 bits) at a sampling rate of 250 MHz. The features within the imaging plane were reconstructed using the filtered universal back-projection algorithm [64].

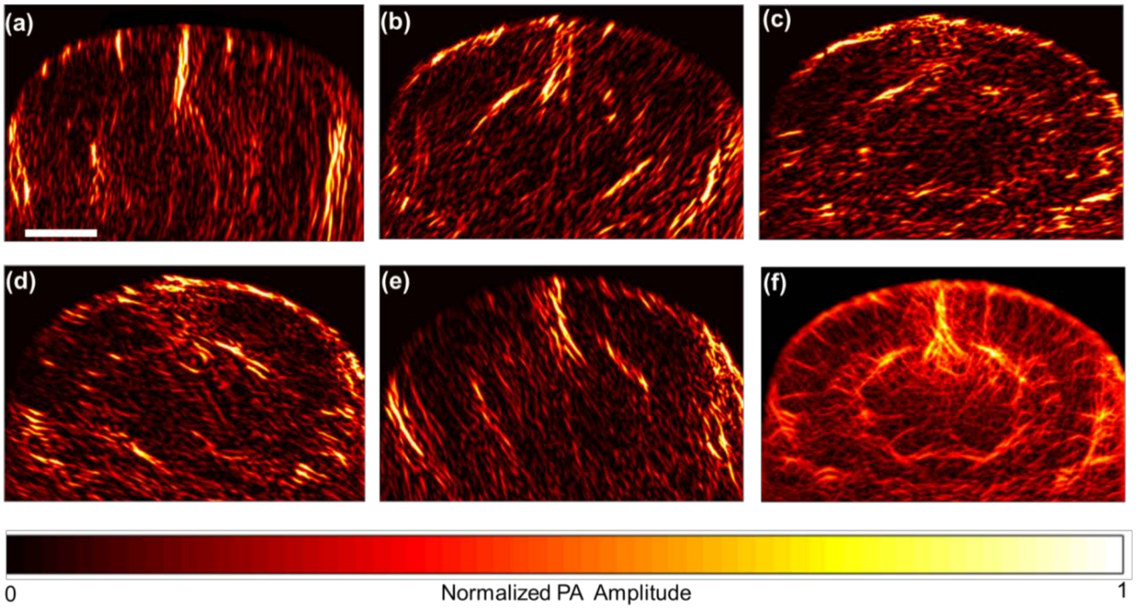

Figure 14. Coronal plane PACT of a mouse brain through the intact skull (Bregma −1.0 mm). (a-e) Limited-view images reconstructed at view angles of –76, –36, 0, 36 and 76 degrees, respectively. Each of these images was averaged over 200 acquisitions. (f) Full-view planar image combined from the 39 limited-view images. The scale bar is 2 mm.

To map the vessels in the coronal plane, the mouse was mounted with its cortical plane horizontal to the bottom of the water tank, and the linear array was oriented in the coronal plane, as shown in **Fig. 13**. The surface of the linear array was about 1 cm away from the top of the head, and the diffused laser beam was obliquely incident on the head. The pulsed laser at 1064 nm was used to excite the PA waves, which came predominantly from oxyhemoglobin, a dominant chromophore in the blood stream. Due to the limited view of the linear array, only vessels normal to the acoustic axis could be reconstructed, but the vessels with their orientation deviated from the axis were almost invisible [65]. **Figure 14a-e** show reconstructed images of a typical coronal plane recorded from several representative view angles, each averaged over 200 acquisitions. To solve this limited-view problem, the linear array was mounted on a rotary stage with its rotational axis centered at the mouse brain. The linear array was then scanned around the brain without changing the laser illumination to record images at view angles ranging from –76 to 76 degrees, with a step size of 4 degrees. The reconstructed bipolar images were converted into unipolar images by Hilbert transformation along each view's acoustic axis [16]. The processed images were then rotated back to recover the vascular distribution in the global coordinate system in which the brain was fixed, and the rotated images were summed to form a full-view unipolar image, as shown in **Fig. 14f**. The full-view image demonstrated that the PACT system equipped with the high frequency linear array can provide high resolution and deep penetration imaging of a whole mouse brain.

Results and discussion

Resting-state functional connectivity of the mouse whole brain

Since light at the chosen laser wavelength is weakly absorbed in biological tissue, and changes in the concentrations of hemoglobin and other absorbers during neural activities are generally small, the local optical fluence in the mouse brain is assumed to be temporally invariant, enabling the PACT system to study the hemodynamic activities in the deep brain. As a first demonstration, we used our linear-array PACT system to study the resting-state functional connectivity (RSFC) in the coronal plane of a mouse brain. RSFC measures the temporal correlation of the low frequency, spontaneous hemodynamic fluctuations among spatially separated but functionally related regions in the brain [66, 67]. The alteration in the functional connectivity properties is usually an indicator of such brain disorders as depression, Alzheimer's disease, and schizophrenia [68-70]. To explore the functional connectivity of a mouse brain in resting state, the linear array was fixed with its axis normal to the cortical plane, and 6000 images were acquired at a frame rate of 10 Hz. This study again used 6–8 week-old female ND4 Swiss Webster mice (Invigo), anesthetized with 0.8% (vol/vol) isoflurane at an air flow rate of 0.8 L/min, a dose does not alter the functional connectivity patterns [71]. The PA signals due to scattered photons from the transducer surface were used to correct the fluctuations in the total laser pulse energy. Every set of 10 images was averaged to improve the signal-to-noise (SNR) ratio, and the resulting 600 images over a 10-minute acquisition were analyzed with a seed-based approach [72, 73]. Basically, the reconstructed images were first filtered by a 2-D Gaussian smoothing kernel with standard deviation of 6 pixels. Then a band pass filter with a window of 0.009-0.08 Hz was applied on the time series of the images to reduce the effects caused by heart beating and breathing [73]. Finally, a seed was chosen and the temporal correlations of its PA signal with that of each pixel in the image were calculated. A high coefficient in the correlation map indicates a region that is functionally related to the seed region. The correlation maps for representative regions in the mouse brain were superimposed on the synthesized anatomic image obtained as described above.

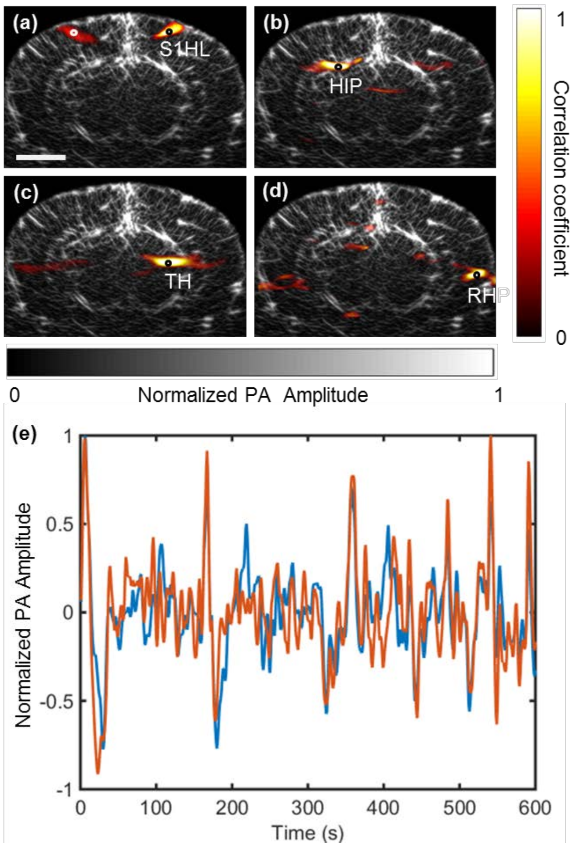
(a)
S1HL
(b)
HIP
(c)
TH
(d)
RHP
1
Correlation coefficient
0
0
Normalized PA Amplitude
1
(e)
Normalized PA Amplitude
1
0.5
0
-0.5
-1
0
100
200
300
400
500
600
Time (s)

Figure 15. Functional connectivity in a mouse brain acquired by a linear-array based full-view PACT. (a-d) The correlation maps calculated at four representative functional regions (black circles) are overlaid onto the anatomic image that was synthesized from multiple limited-view images (Bregma −1.0 mm). The scale bar is 2 mm. S1HL, somatosensory 1,

hindlimb region; HIP, hippocampal region; TH, thalamus; RHP, retrohippocampal region. (e) Time series of the filtered PA signals of a pair of correlated regions as marked in (a). The red and blue curves are corresponding to the points marked in white and black circles, respectively. Amplitudes are normalized to the maximum.

As shown in **Fig. 15a-d**, strong interhemispherical correlations were observed in the chosen functional regions, including the somatosensory, hippocampal, thalamic and retrohippocampal regions. The high correlations in the contralateral hemisphere were mostly from the regions symmetrically opposed to the seeds. **Figure 15e** also shows the time series of the filtered PA signals of a pair of correlated regions marked by white and black circles in **Fig. 15a**, displaying strong correlation in their fluctuations.

Epileptiform activities of the mouse brain

PACT using a high frequency transducer array allows studying the hemodynamics in the mouse brain with high spatial and temporal resolutions. To demonstrate this capability, we used our linear-array PACT system to study epilepsy in a mouse model. An epileptic seizure in a mouse was induced by injection of 4-aminopyridine, a potassium channel blocker. A hole with a diameter of 1 mm was drilled in the skull prior to imaging, and 2 μl of 4-aminopyridine solution at a concentration of 15 mM was injected into the brain through a 30 gauge needle. After the injection, the neural activities were imaged with the linear array fixed at an angle of 30 degrees. The images were acquired at a frame rate of 10 Hz, and every ten images were averaged into one, resulting in a temporal resolution of 1 s. The PA signal from the transducer surface due to scattered photons was used to correct the fluctuations in the total laser pulse energy. The fractional changes in the PA amplitude at different times after the injection are shown in **Fig. 16**. As indicated, an increase in the PA amplitude was initially observed at the injection site and then spread out. Even more interesting, epileptic wave propagation was also observed in the opposite hemisphere.

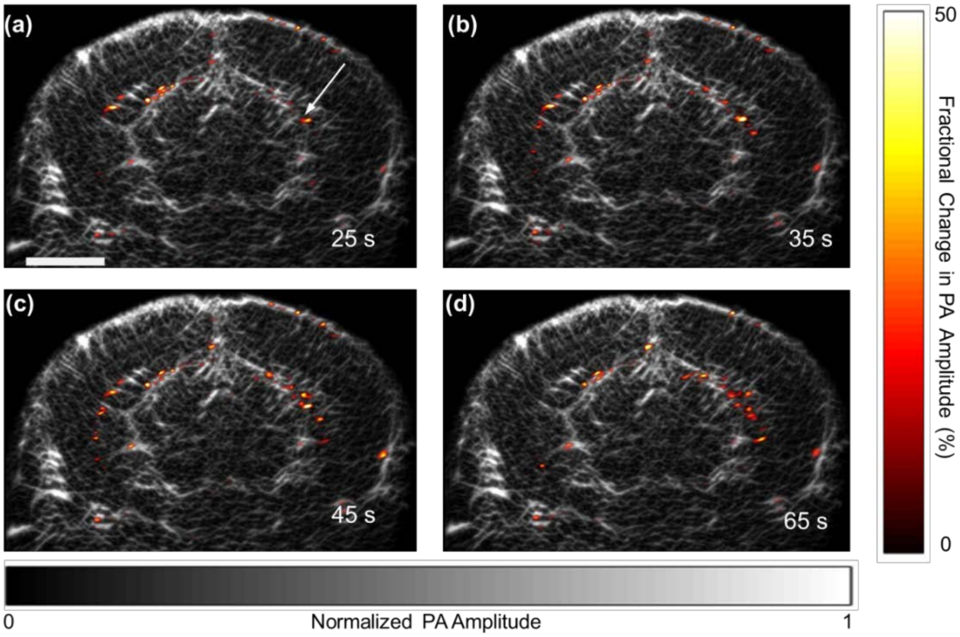

Figure 16. Epileptiform activities of a mouse brain during a seizure. The fractional changes in the PA amplitude at different times after the injection of 4-aminopyridine solution are superimposed on the anatomic image (Bregma –1.0 mm). The scale bar is 2 mm, and the arrow indicates the injection site.

Discussion

In summary, we have built a linear-array PACT system for imaging a whole mouse brain through the intact skull and for studying hemodynamic activities with high spatial resolution and deep penetration. The linear array was scanned in the coronal plane to collect images at different angles. Combing the limited-view images into a full-view image revealed the microvascular network in the brain. We investigated spontaneous neural activities in the deep brain by monitoring the concentration of hemoglobin in the blood vessels and observed strong interhemispherical correlations between chosen functional regions, both in the cortex and in the deep region. We also used linear-array PACT to study epilepsy in the mouse brain induced by an injection of a potassium channel blocker. We observed the epileptic wave spreading around the injection site and a corresponding wave propagating in the opposite hemisphere.

The imaging frame rate of our functional PACT system is lower than that of functional ultrasound imaging [59, 74]; however, we can circumvent this limitation by employing a higher repetition-rate laser for PA excitation. On the other hand, PACT utilizes a different contrast mechanism from ultrasound imaging. Ultrasound tomography images the mechanical properties of soft tissue, and has poor extravascular molecular contrasts. On the basis of the optical absorption of biomolecules, PACT enables molecular imaging by matching the excitation optical wavelength with the absorption peaks of the targeted molecules [75, 76], and thus provides high image contrast. Moreover, PACT can measure the concentration and oxygen saturation (sO_2) of hemoglobin, which are closely related to brain activities but cannot be revealed by ultrasound imaging [77, 78].

Chapter 4

MULTI-CONTRAST PACT WITH ENDOGENOUS CONTRASTS

Monitoring largescale hemodynamic responses

By taking advantage of the difference between the oxy- and deoxy-hemoglobin absorption spectra (**Fig. 17**), we can image whole-body oxygenation dynamics by exciting PA waves alternately with two optimal wavelengths [4]. In order to systemically modulate the oxygen saturation of hemoglobin (sO_2), we manipulated the oxygen concentration in the inhalation gas.

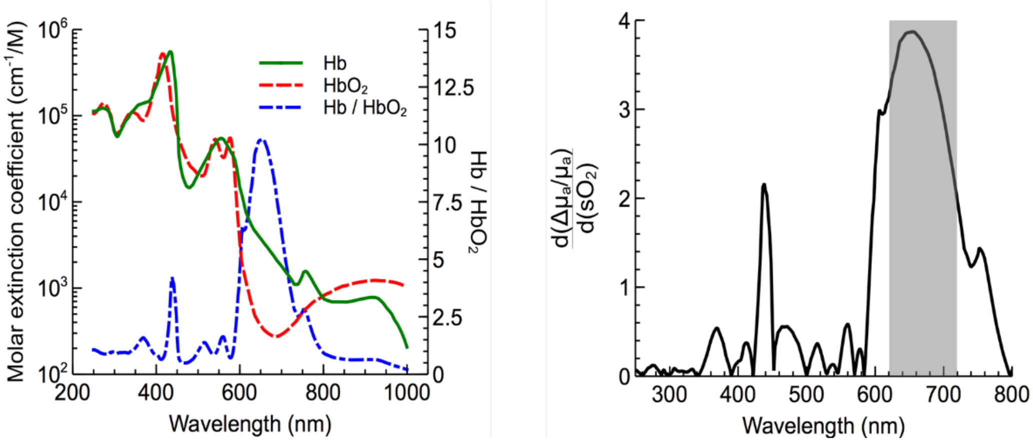

Figure 17. (a) The absorption spectra of oxy-hemoglobin (HbO_2) and deoxy-hemoglobin (HbR), and the absorption ratio of deoxy-hemoglobin to oxy-hemoglobin (HbR/HbO_2). (b) Fractional changes of blood's absorption coefficient (μ_a) corresponding to the blood sO_2 change ($d(\Delta\mu_a/\mu_a)$ / $d(sO_2)$) with visible and NIR light illumination. Wavelengths from 626 nm to 720 nm provide an sO_2 sensitive imaging window for SIP-PACT (highlighted by the gray area).

By illuminating the mouse brain from the top (**Fig. 3a**) with two laser pulses of different wavelengths at a biologically negligible delay (50 µs), we noninvasively imaged both the cortical vasculature and the sO_2 of the cortical vessels *in vivo* (**Fig. 18a** and **18b**). In this experiment, a mixture of 95% oxygen and 5% nitrogen was initially used with gaseous isoflurane for anesthesia. During the oxygen challenge, the mixture was switched to 5%

oxygen and 95% nitrogen for 3 minutes (4.5 minutes for whole-body oxygen challenge), and then switched back to the initial concentration to end the challenge. We estimated the systemic sO_2 change by averaging signals over the superior sagittal sinus, the central vessel shown in color in **Fig. 18a** and **18b**. Variations in sO_2 (**Fig. 18c**), derived from changes of oxy- and deoxy-hemoglobin concentrations (**Fig. 18d**), were observed following the manipulation of the inhalation oxygen concentration. The sO_2 drop resulting from hypoxia is manifestly slower than its recovery, consistent with previous observations [51, 79].

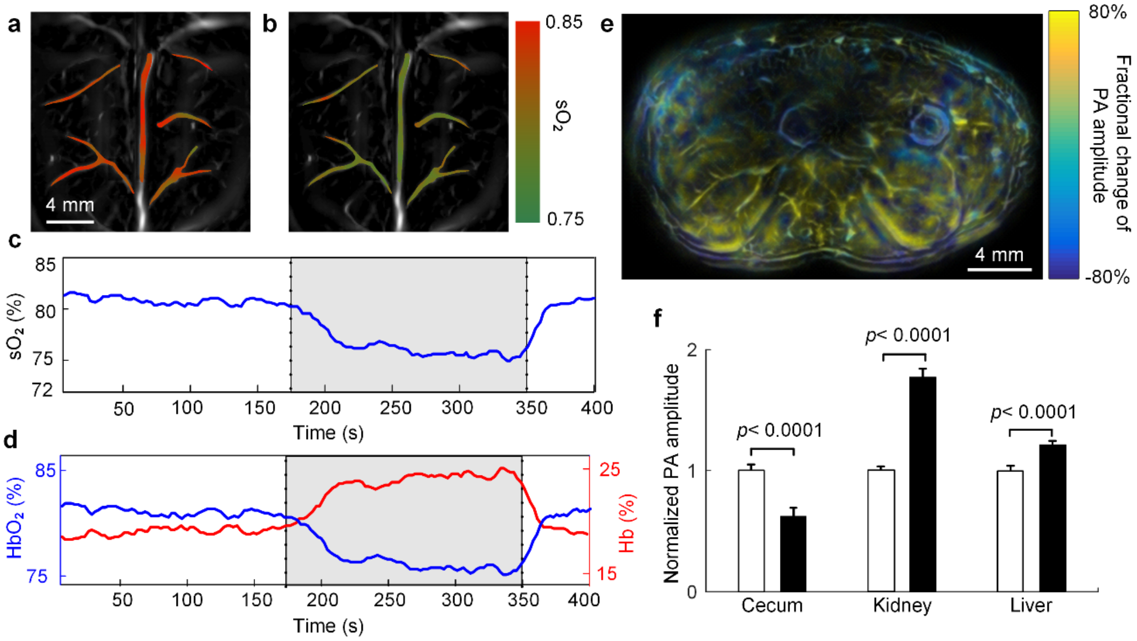

Figure 18. SIP-PACT of mouse whole-body oxygenation dynamics. sO_2 mapping of mouse cortical vasculatures during (a) hyperoxia and (b) hypoxia. (c) Brain sO_2 changes during oxygen challenges, the gray rectangle outlines the challenge periods. (d). Changes in concentrations of oxy-hemoglobin and deoxy-hemoglobin during oxygen challenges, the gray rectangle outlines the challenge periods. (e) Fractional changes in blood oxygen level in the cross-sectional image of the lower abdominal cavity. (f) Normalized PA amplitude, corresponding to blood oxygen level, in internal organs during hyperoxia and hypoxia, where the hollow bars represent the baseline amplitudes and the solid bars represent the plateau amplitudes during challenge ($n = 50$, error bars are s.e.m.). The p values were calculated by paired Student’s t-test.

BOLD MRI, with wide use for functional studies in both animal models and humans, is sensitive primarily to the concentration of deoxy-hemoglobin [80, 81]. Similar to BOLD

MRI, SIP-PACT can also map the trunk's hemodynamic response to a change in oxygen supply by using a single deoxy-hemoglobin sensitive wavelength for excitation, but at a higher imaging speed and greater sensitivity than those of BOLD MRI. After we switched the oxygen concentration from 95% to 5%, the whole-body oxygenation levels changed accordingly (**Fig. 18e**). Because deoxy-hemoglobin has a much stronger molar optical absorption than oxy-hemoglobin at the excitation wavelength of 720 nm, the PA signal changes reflected mainly the whole-body deoxy-hemoglobin concentration changes. In **Fig. 18e**, yellow represents a positive relative PA signal change, which means a decrease in sO_2, while blue shows a negative relative PA signal change, meaning that sO_2 increased. When a global shortage of oxygen occurs, the whole-body sO_2 should drop accordingly. We observed a relative sO_2 decrease in most of the organs, such as the brain, liver, and kidney, and an sO_2 increase in some organs, such as the cecum (**Fig. 18f and Fig. 19**). These observations might be explained as follows: Once global hypoxia occurs, the animal adjusts its whole-body metabolic activity to survive the challenge. The vital organs, such as the brain, heart, and kidney, must maintain their basic functions with normal metabolic activities, so their maintained oxygen consumption under hypoxia leads to an sO_2 drop [82]. Because some other organs, such as the cecum, reduce their metabolic activity to save oxygen for other vital organs, a reduced oxygen extraction fraction leads to an sO_2 increase within those organs [83-85]. For the first time, to our knowledge, we have photoacoustically imaged the dynamics of whole-body oxygenation distribution across internal organs with great detail *in vivo* and without labeling.

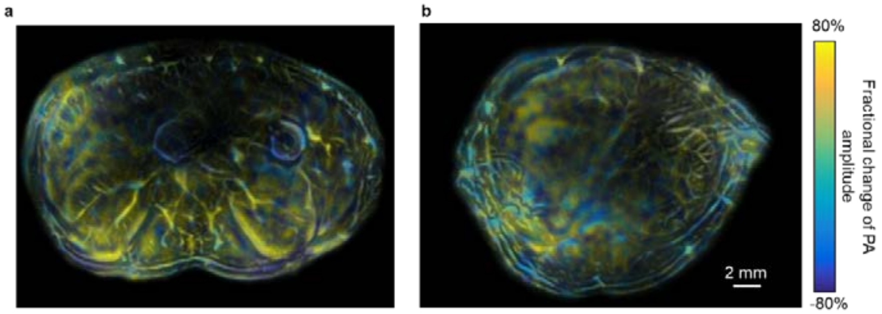

Figure 19. Fractional changes of blood oxygen levels in the cross-section of (a) the lower abdominal cavity during oxygen challenge and (b) the liver during oxygen challenge.

Imaging brain structures

From **Fig. 20a** we can see that at the removal of hemoglobin from the tissue, cytochrome becomes the dominant absorber in the visible region. In a mouse brain, by dry weight, gray matter has 55% protein and 33% lipid, white matter has 55% lipid and 40% protein, and myelin has 70% lipid and 29% protein [86]. Thus the difference in protein/lipid concentrations can be utilized to differentiate the brain structures [24]. To remove the hemoglobin, we used saline perfusion. As shown in **Fig. 20b**, with 600 nm light illumination, a PACT image acquired on the brain surface shows rich cortical vasculature. Signals from major vessels, such the superior sagittal sinus, are so strong that their shadows even appear in the deep brain image (**Fig. 20c**). Consequently, even though different brain structures have different cytochrome and lipid concentrations, which might provide us with structural contrast, we still cannot differentiate them in the deep brain image.

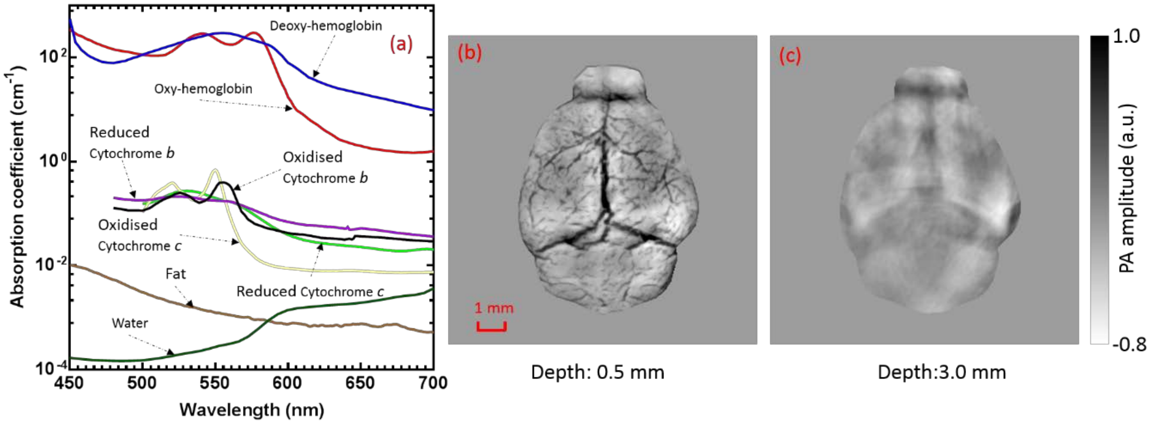

Depth: 0.5 mm

Depth:3.0 mm

Figure 20. Label free PA imaging. (a) Absorption coefficient spectra of endogenous tissue chromophores at typical concentrations in the human body (Adapted from http://omlc.ogi.edu/spectra and http://www.ucl.ac.uk/medphys/research/borl/intro/spectra) (b) *In vivo* imaging of the mouse brain cortex through the intact skull (imaging depth: 0.5 mm beneath the skull surface). (c) *In vivo* imaging of the deep mouse brain (imaging depth: 3.0 mm beneath the skull surface).

Saline perfused mice were prepared by the Hope Center Animal Surgery Core at Washington University, following the standard mouse transcardial perfusion protocol. Blood was removed from the body tissue by pumping phosphate-buffered saline into the left ventricle and draining the blood from the aorta, which was cut with scissors. After 4-5 minutes, the fluid exiting the aorta was clear and the liver had turned white. At this point most of the blood in the body had been replaced with saline. We then dissected the head and placed it into 10% paraformaldehyde (PFA) solution for preservation. After 24 hours of fixation in 10% PFA, we embedded the head in 3% agar gel for imaging.

Figure 21a shows a label-free PACT image (from 2.8 mm below the brain surface) of a saline-perfused mouse brain. To better illustrate different regions, we segmented **Fig. 21a** per the PA amplitude, and labeled different segmentations (**Fig. 21b**). For comparison, we chose one slice of a 3D high-resolution (50 μm in plane resolution) MRI image, with its structural segmentation superimposed as colored lines (**Fig. 21c**) [87], as a gold standard. The mouse brain PACT image shows a nearly perfect match with the MRI image. Different brain structures are clearly identified, including the central gray, cerebellum, cerebral aqueduct, corpus callosum, hippocampus, hypothalamus, inferior colliculus, neocortex, olfactory bulb, and ventricles. To our knowledge, this is the first time that PACT has clearly shown deep structures of the brain with rich contrast among different brain tissue, with the brain intact and without any labeling.

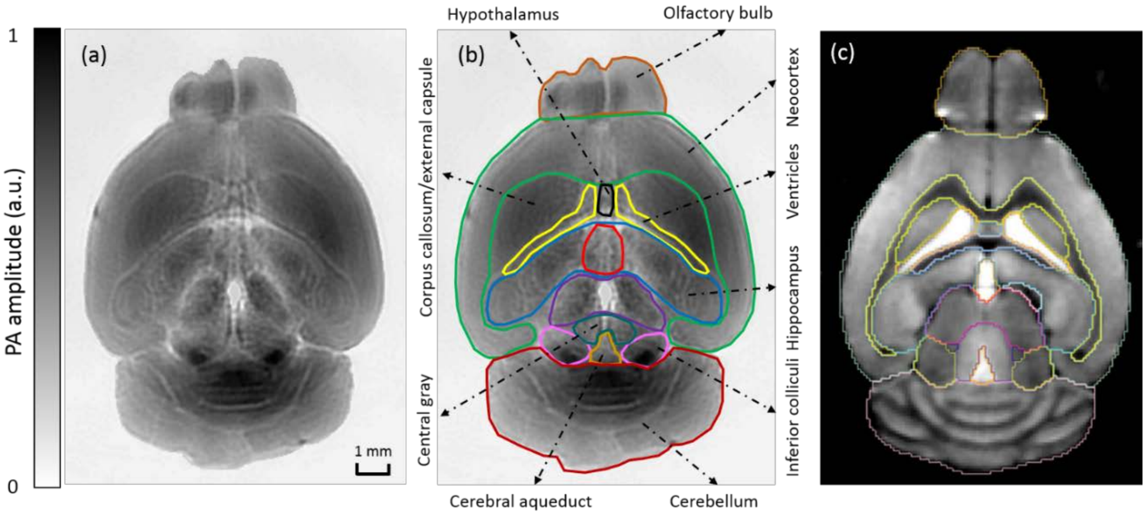
1
0
PA amplitude (a.u.)
(a)
1 mm
(b)
Hypothalamus
Olfactory bulb
Corpus callosum/external capsule
Central gray
Cerebral aqueduct
Cerebellum
Neocortex
Ventricles
Hippocampus
Inferior colliculi
(c)

Figure 21. PACT of the saline perfused mouse brain without the skull. (a) Cross-sectional PACT image of the mouse brain at 2.8 mm depth, clearly resolving the structure of the

brain. (b) Segmented and annotated image from (a). (c) One slice of a 3D high-resolution MRI image with its structural segmentation superimposed as colored lines, chosen as a gold standard for validation of PACT (Courtesy of Frontiers in Neuroscience) [87].

To find the optimal wavelength for imaging brain structures and to verify the origin of contrasts, we varied the laser wavelength from 480 nm to 680 nm with a 20 nm interval. **Figure 22** shows the spectral PACT images of a mouse brain at one selected depth (2.8 mm below the brain surface). A quantitative spectral analysis is discussed in detail in the following sections.

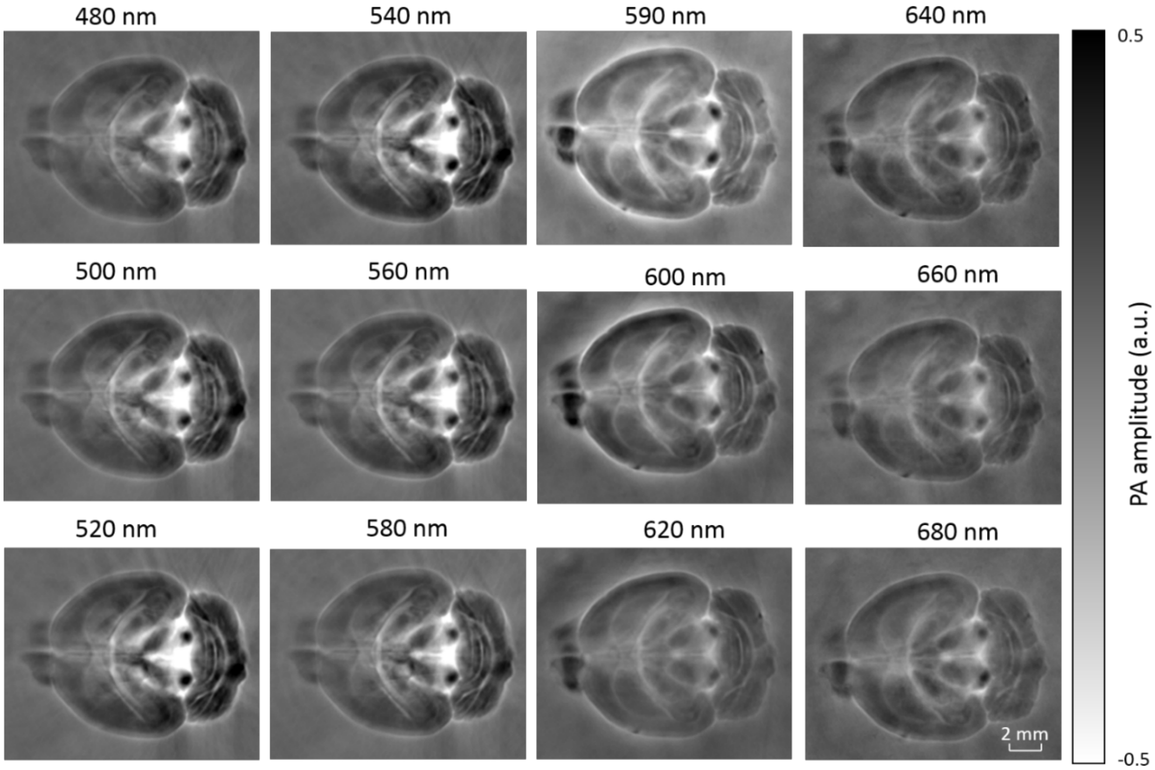

Figure 22. Spectral PACT of a mouse brain at 2.8 mm depth.

After the removal of blood, the remaining dominant chromophores are nuclei (DNA and RNA), water, cytochrome, and lipid. DNA and RNA have a strong absorption in the ultraviolet band (240 nm – 280 nm). However, in the visible light band (420 nm – 680 nm), their absorption is negligible and is $10^2 - 10^3$ times weaker than that of cytochrome [88]. Water contents in various brain tissue are very similar [89], and thus probably provide a relatively constant background in PACT images. Thus, the structural contrast should mainly come from cytochrome/lipid distribution. Each pixel in a single-wavelength PACT image represents a combined contribution from M optical absorbers with known molar extinction coefficient spectra a_m and unknown concentrations c_{m} (m = 1, 2, …, N). Then the spectral decomposition equation can be expressed as

$$\mu_a(\lambda_n) = \sum_{m=1}^{M} a_m(\lambda_n)c_m,\ m = 1,2,\dots,N, \tag{4}$$

where λ_{n} is the *n*th wavelength used for PA excitation. Based on the known extinction coefficients, the concentrations of the optical absorbers can be quantified. In the following spectral analysis, we assume that differences between the Grüneisen parameters of different types of cytochromes are negligible, which was validated in a previous report [90].

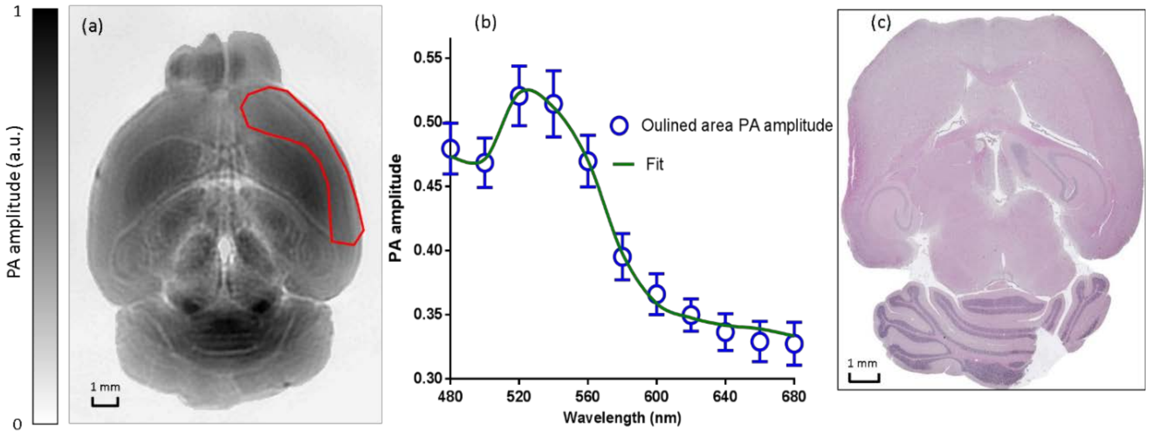

Figure 23. Spectral analysis of the origin of optical absorption in the brain. (a) Cross-section imaged at 600 nm wavelength at 2.8 mm depth as part of the 3D brain imaging, with red outlined areas segmented for analysis. (b) Measured PA spectrum and least-squares fit with a mixture of cytochromes *b* and *c*. (c) Histology image of one horizontal section slice stained with hematoxylin and eosin (H&E).

In mammals, the brain performs numerous computationally intensive tasks, such as information processing, perception, motion control, and learning, and thus consumes a large amount of energy in proportion to its volume. Mitochondria, the energy source, populate the cytoplasm of mammalian cells, including neurons, which rely on mitochondrial energy production for survival [91]. The absorption sources of the mitochondria are mainly cytochromes *b* and *c* [90, 92]. Moreover, myelin has a high concentration of lipid, which has orders of magnitude weaker absorption than that of cytochrome over the spectral range of 480-680 nm. Thus the existence of myelin would further sharpen the contrast of cytochrome. Therefore, the distributions of chromophores map the brain with vivid contrast in PACT images.

Figure 23a shows the optical absorption contrast in one cross section (2.8 mm below the brain surface) based on the joint reconstruction approach. The spectral PA responses (normalized by the laser fluence) of the neocortex area encircled by the red line in **Fig. 23a** are plotted in **Fig. 23b** (labeled by circles). The neocortex consists of gray matter, or neuronal cell bodies and unmyelinated fibers. The high concentration of mitochondria in neuronal cell bodies might be responsible for the optical absorption. Because the absorption sources in mitochondria are mainly cytochromes *b* and *c* [90, 92], the PA spectrum of the red outlined area was fitted according to Eq. (4) with a mixture of 65 ± 12% (molar ratio, mean ± standard error) cytochrome *b* and 35 ± 9% cytochrome *c*, which is in agreement with the measured concentration of cytochrome in mitochondria [90]. The squared 2-norm of the residual is 0.003. The accuracy of spectral analysis, however, is subject to the possible presence of other neglected absorbing proteins (such as cytochrome p450, nitric oxide synthases, and myeloperoxidase) with similar spectra. Absorption from other sources, such as water, flavoproteins, nicotinamide adenine dinucleotide, or other neglected hemeproteins, is orders of magnitude weaker than cytochrome, and was removed as a constant background during the fitting. A hematoxylin and eosin (H&E) stained histology image (**Fig. 23c**) of a horizontal brain section is presented as a validation of the optical absorber, where pink represents the proteins in the cytoplasm and blue represents DNA/RNA in nuclei. In the H&E stained histology image, the brain structure contrast from cytoplasm distribution matches with the absorption contrast based PACT brain structure image, whereas the optical absorption from DNA/RNA is negligible under visible light illumination. This comparison between our PACT image and the H&E stained histology image further validates that the structural contrast is mainly caused by proteins in cytoplasm.

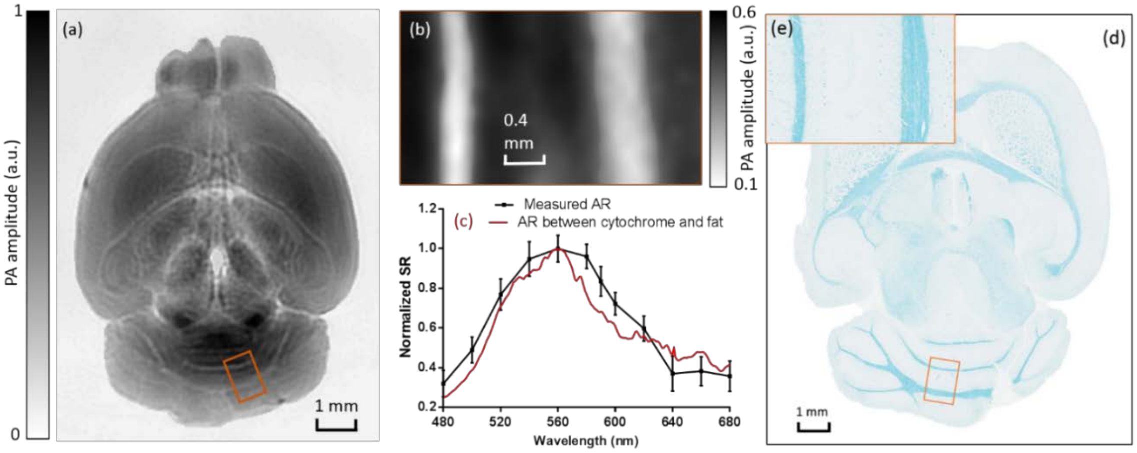

Figure 24. Analysis of the origins of the contrast. (a) Cross-section imaged at 600 nm wavelength at 2.8 mm depth selected from the 3D brain images, with brown outlined areas segmented for analysis. (b) Close-up of the region inside the brown square in (a). (c) Comparison of the measured AR between the granular cell layer and the cerebellar white matter and the AR between cytochrome and fat. (d) Histology image of one horizontal section slice stained with luxol fast blue. (e) Close-up of the region inside the brown square in (d).

To further confirm that structural contrast comes mainly from cytochrome and lipid, another area in the cerebellum (**Fig. 24a**) was segmented for spectral analysis. In a close-up image (**Fig. 24b**), white and black stripes correspond to cerebellar white matter and the granular layer, respectively [93, 94]. The cerebellar white matter, made up largely of myelinated nerve fibers, has a high concentration of lipid, and the granular layer has a high concentration of cytochrome. We calculated the absorption ratio (AR) between the granular cell layer and the cerebellar white matter as follows:

$$AR = \frac{mean(PA_{cwm})}{mean(PA_{gcl})}, \tag{5}$$

Here PA_{cwm} is the PA amplitude of the cerebellar white matter region, and PA_{gcl} is the PA amplitude of the granular layer region. We compare the result with the AR of cytochrome to lipid, which is obtained by taking the ratio point by point between the cytochrome absorption spectrum and the lipid absorption spectrum shown in **Fig. 20a**. The two results match well with each other (**Fig. 24c**), which indicates that the contrast of the PACT image of the saline-perfused brain comes mainly from cytochrome and lipid. To confirm the presence of lipid, a horizontal brain section was stained with luxol fast blue (**Fig. 24d**), which is a commonly used to observe myelin. Comparing the cerebellum of the mouse brain in **Fig. 24a** and **b** with **Fig. 24d** and **e**, the cerebellar white matter structures match well with each other. Combined with the conclusion from **Fig. 23**, **Fig. 24d** tells us that the absorption difference between myelin and cytochrome sharpens PACT image contrast. A potential future study would focus on directly imaging lipid in the mouse brain by employing infrared light around 1200 nm and 1700 nm, which are the C-H bond absorption peaks [95].

Tracking of circulating melanoma tumor cells

Circulating tumor cells (CTCs) have been regarded as an important pathway and a potential indicator for tumor metastasis, a hallmark of tumor malignancy [96, 97]. Tracking the fate of metastasizing cancer cells *in vivo* is vitally important to the study of early extravasation, early angiogenesis, and treatment of cancer [98]. In this study, we targeted melanoma, a skin cancer which was expected to cause an estimated 10,130 fatalities in the United States in 2016 [99], and demonstrated that our SIP-PACT system could monitor melanoma migration in the entire mouse cortical vasculature *in vivo [4]*.

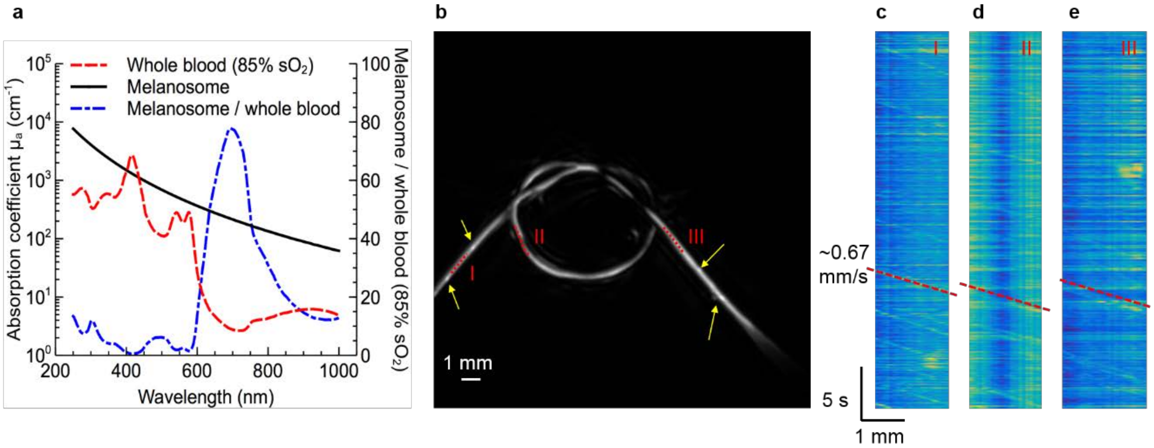

Figure 25. Detection of melanoma cells in blood *in vitro*. (a) Spectra of whole blood (85% sO_2) and melanosome, and the absorption ratio of melanosome and whole blood, which peaks at 680 nm. The melanosome to blood contrast can be maximized with 680-nm excitation. (b) Image of a tube (300 µm in diameter) filled with the mixture of blood and melanoma cells (10^6 cells in 2 mL of bovine blood). The mixture of blood and melanoma

cells is driven by a syringe to flow through the tube. The melanoma cells (or cluster) are highlighted by the yellow arrows. (c–e) Time trace plot of each pixel along the red dashed line in (b). The space-time domain slope in (c–e) were computed by linear fitting as ~0.67 mm s^{-1}, representing the flow speed of melanoma cells.

Melanin has a much stronger optical absorption at around 680 nm than hemoglobin does (**Fig. 25**). Hence, we used SIP-PACT with 680-nm laser excitation to capture the migration of intra-arterially injected melanoma cancer cells along cortical vessels in real-time, with high contrast and without any labeling. We should note that the injected melanoma cells could present in the bloodstream in the form of both single cells and CTC clusters, contributing to the strong signals in our images. A motion-contrast image created from signals before (**Fig. 26a**) and after CTC injection and overlaid on the vascular image shows the melanoma cancer cells (**Fig. 26b**), where colors represent the CTCs' flow directions. The movements of melanoma cancer cells in the yellow dashed box region in **Fig. 26a** are visualized in **Fig. 26c**, where the melanoma cells in the current frame are highlighted in red, those in the previous frames are shown in green, and the flow path of each cell is marked by an orange dashed line. By tracking the melanoma cells in real time and analyzing the movement of flowing melanoma cells in the spatiotemporal frequency domain, we can compute the flow rate of the cancer cells, which is smaller than the cerebral blood flow rate [100, 101]. We extracted the time traces of each pixel along the red dashed line in **Fig. 26a**, and plotted the signals as an image in the space-time domain (**Fig. 26d**). By taking the two-dimensional Fourier transformation of this image, we mapped lines with the same slope in the space-time domain onto a single line in the spatiotemporal frequency domain (**Fig. 26e**), simplifying the calculation of the flow speed and providing better accuracy. The flow speed of the melanoma cells was computed by linear fitting to be 0.65 mm/s. Applying this method with a sliding window, we were able to visualize CTC flow speed distributions in multiple vessels of the brain (**Fig. 26f**).

We visualized the flowing of melanoma cancer cells in both cortical arteries (**Fig**. **27**) and veins. We also observed occasionally ceased motion of melanoma cells, which might be a possible sign of the homing of metastasizing cancer cells (**Fig**. **28**).

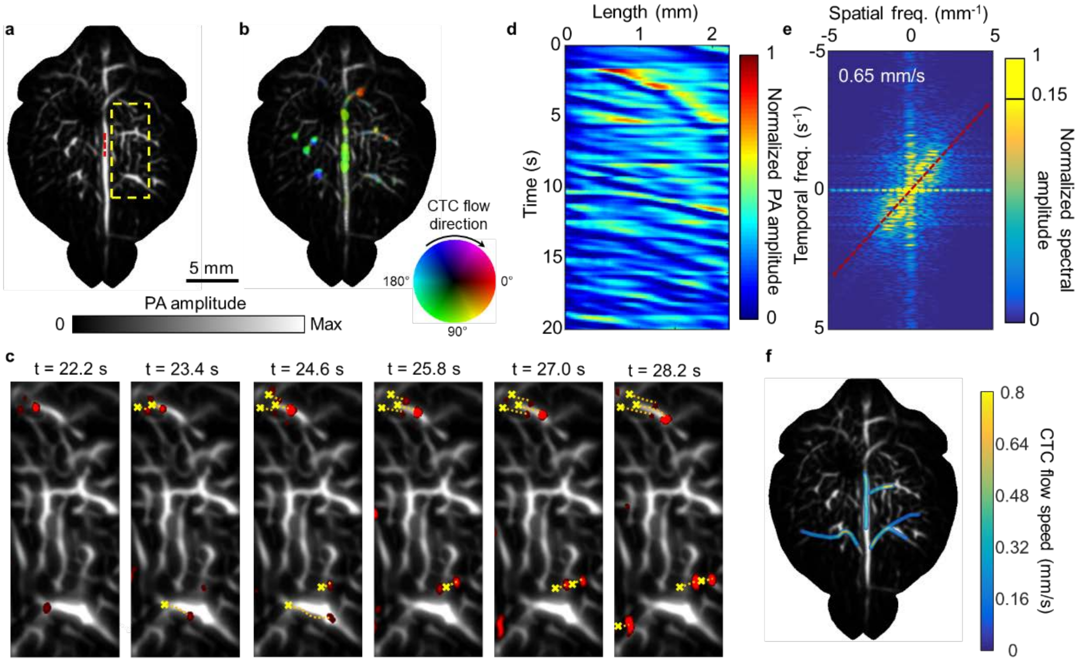
a
b
5 mm
PA amplitude
0
Max
CTC flow direction
180°
0°
90°
d
Length (mm)
0
1
2
Time (s)
0
5
10
15
20
Normalized PA amplitude
1
0
e
Spatial freq. (mm-1)
-5
0
5
Temporal freq. (s-1)
-5
0
5
0.65 mm/s
Normalized spectral amplitude
1
0.15
0
c
t = 22.2 s
t = 23.4 s
t = 24.6 s
t = 25.8 s
t = 27.0 s
t = 28.2 s
f
CTC flow speed (mm/s)
0.8
0.64
0.48
0.32
0.16
0

Figure 26. Label-free tracking of CTCs in the mouse brain *in vivo*. (a) Baseline cortical vasculature before the injection of melanoma cancer cells, under 680-nm excitation. (b) PA imaging of the mouse cortex after injection of melanoma cancer cells, where colors represent CTCs' flow direction. Flow speed is radially encoded in the color disk by hue saturation (a greater radius indicates faster) (c) Tracking the flowing of cancer cells, where red highlights the moving cancer cells in the current frame, yellow crosses show their initial positions, and the orange dashed lines represent the CTCs' flowing traces. (d) Time trace plot of each pixel along the red dashed line in (a). (e) 2D Fourier transform of (d), which maps lines with the same slope in the space-time domain onto a single line in the spatiotemporal frequency domain. The slope of the red dashed line, computed by linear fitting as 0.65 mm s-1, represents the flow speed of CTCs. The spectral amplitude values were normalized according to the maximum value, and were saturated at 0.15 for display purposes. (f) Flow speed distribution of CTCs in segmented cortical vessels.

SIP-PACT has demonstrated the ability to track unlabeled circulating melanoma cancer cells *in vivo* in the mouse brain. This capability might provide new insights into metastasis research, which can potentially be used to better tailor cancer therapies in the future.

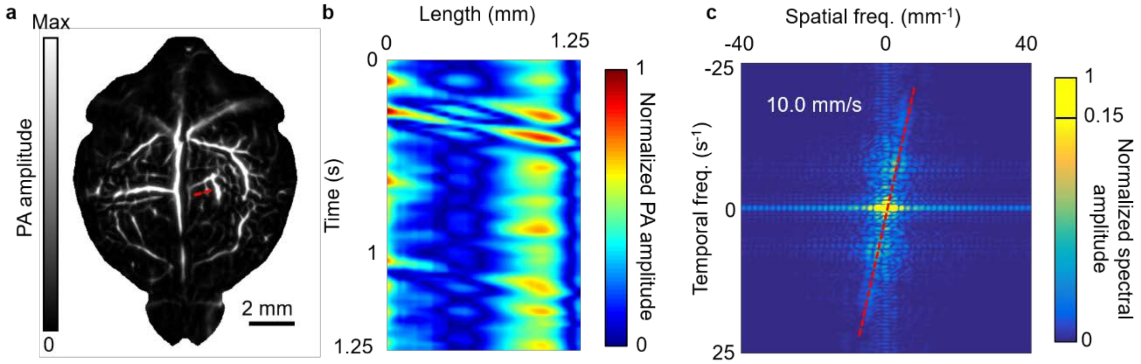

Figure 27. Flowing of melanoma cells in cortical arteries. (a) PA image of the mouse brain cortex after injection of melanoma cancer cells. (b) The time trace plot of each pixel along an artery (the red dashed line in (a)). (c) 2D Fourier transform of (b), which maps lines with the same slope in the space-time domain onto a single line in the spatiotemporal frequency domain. The slope of the red dashed line, computed by linear fitting as 10.0 mm s^{-1}, represents the flow speed of CTCs, which is higher than that in veins.

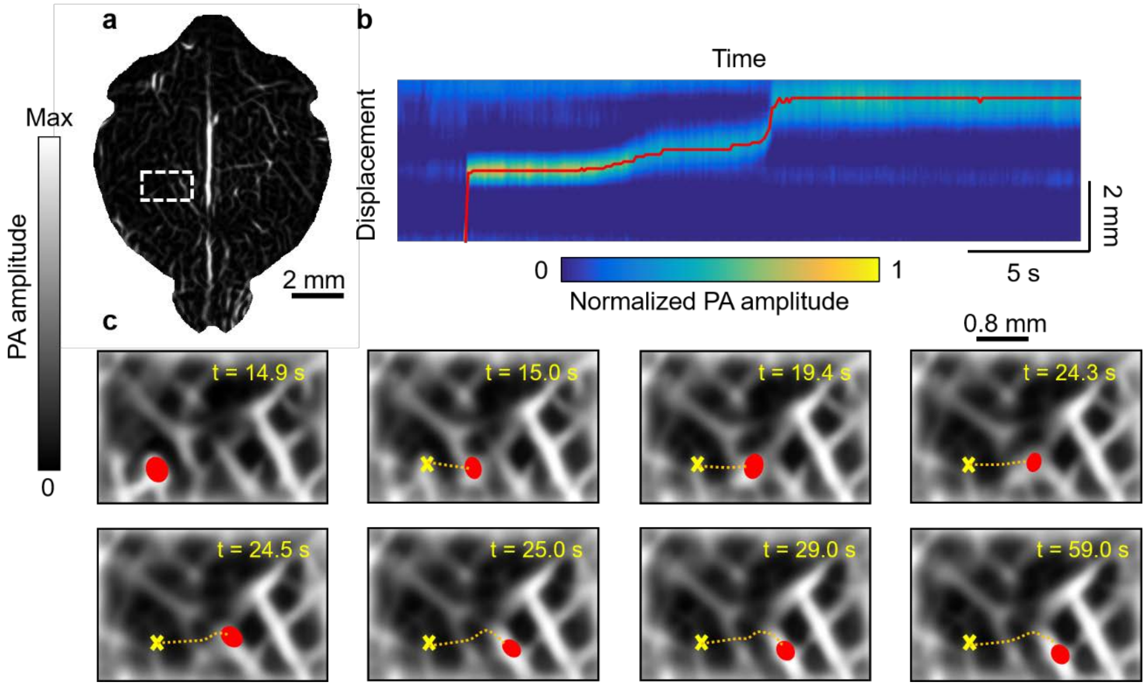
a
Max
PA amplitude
0
2 mm
b
Time
Displacement
2 mm
5 s
0
1
Normalized PA amplitude
c
0.8 mm
t = 14.9 s
t = 15.0 s
t = 19.4 s
t = 24.3 s
t = 24.5 s
t = 25.0 s
t = 29.0 s
t = 59.0 s

Figure 28. *In vivo* observation of CTCs whose motion in mouse cortex has ceased. (a) The PA image of the mouse brain cortex after injection of melanoma cancer cells. (b) Displacement versus time trace plot of the finally ceased CTCs, where the red line is the displacement of the center position of the non-moving CTCs, and the plateau of the red line represents where and when the CTCs ceased moving. (c) Zoomed-in images of the white dashed box in (a), where the yellow crosses represent the initial center position of the

tracked CTC, the red patches label its central position in the current frames, and the orange dashed lines represent the CTCs’ flowing traces.

Chapter 5

MULTI-CONTRAST PACT WITH EXOGENOUS CONTRASTS

PACT of organic near-infrared dyes

Visualization of the whole-body dye perfusion

An NIR dye (FHI 104422P, Fabricolor Holding Int'l LLC) that has much higher optical absorption at 1064 nm than blood does (**Fig. 29**) can be used for visualization of the perfusion process *in vivo [4]*.

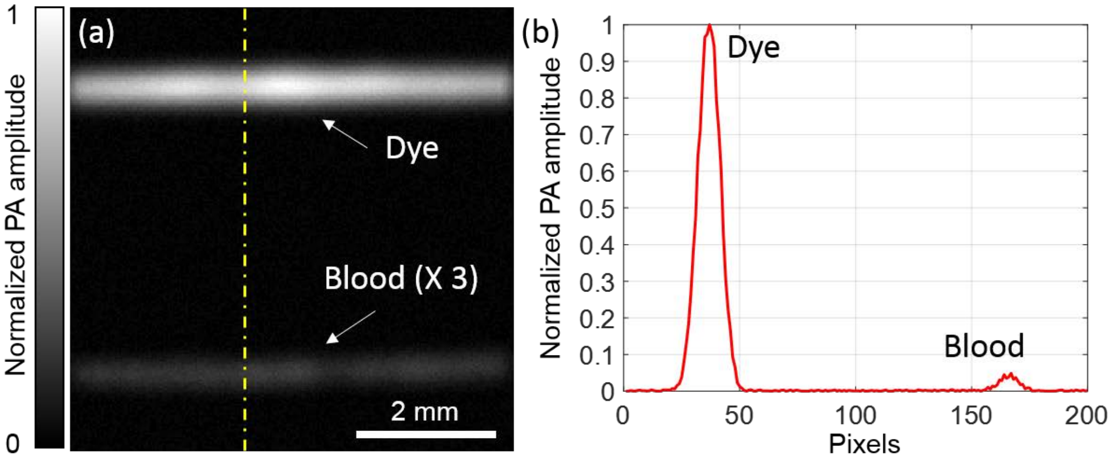

Figure 29. Comparison of absorption of the NIR dye and bovine blood (90% sO_2) at 1064 nm. The NIR dye (0.5% mass concentration in deionized water) and bovine blood are filled in silicone tubes (600 µm diameter), which is embedded in agar. (a) PA image of the two tubes filled with NIR dye and bovine blood, with 1064-nm illumination. The signals from blood are amplified by 3-fold for improved display. (b) Line profile of the yellow dashed line in (a), showing that the NIR dye has 19.8-fold more absorption than blood at 1064 nm. Thus the absorption coefficient of the dye solution is 74.7 cm^{-1}.

After an intra-arterial injection of the NIR dye, the dye perfusion in both the mouse brain and internal organs were visualized by SIP-PACT (**Figs. 30 and 31**) [4]. We thus have demonstrated SIP-PACT's potential for molecular imaging once the dye is functionalized.

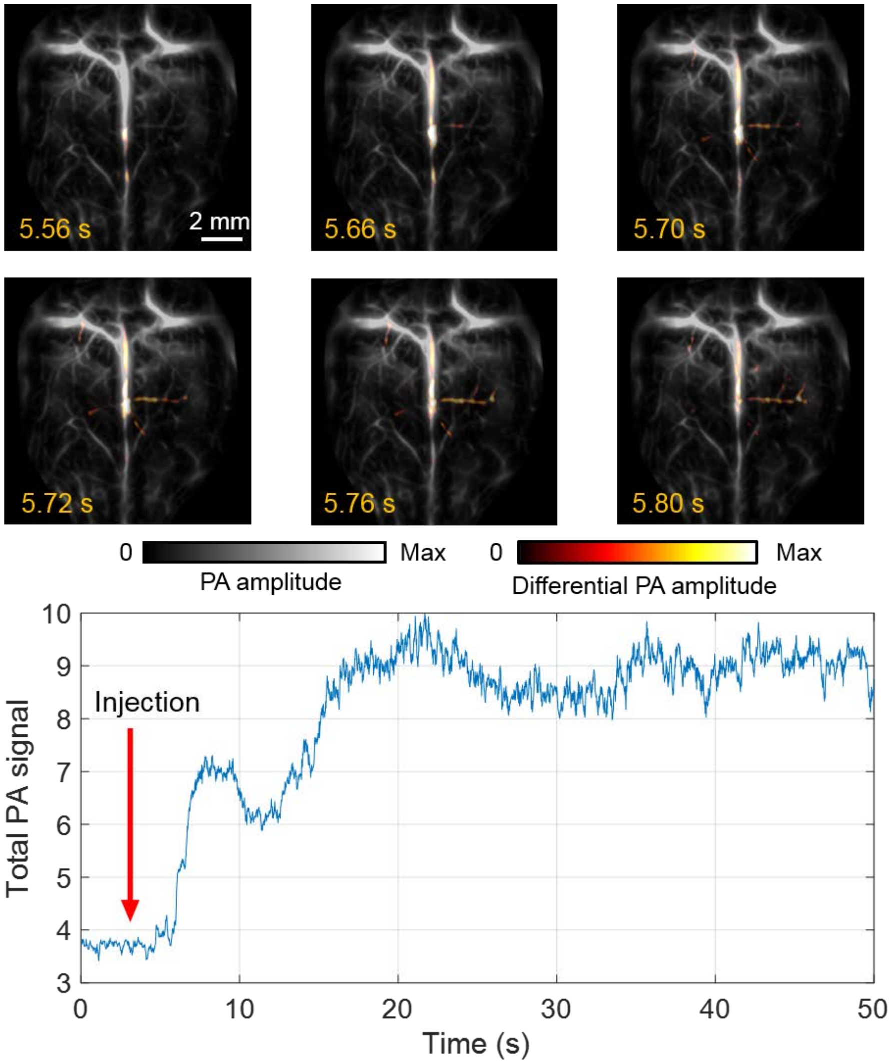

Figure 30. Visualization of dye perfusion in the mouse brain. (a) Images of the mouse cortex after the injection of dye solution at different times. (b) The total PA signal of the mouse brain greatly increases after the injection of dye solution.

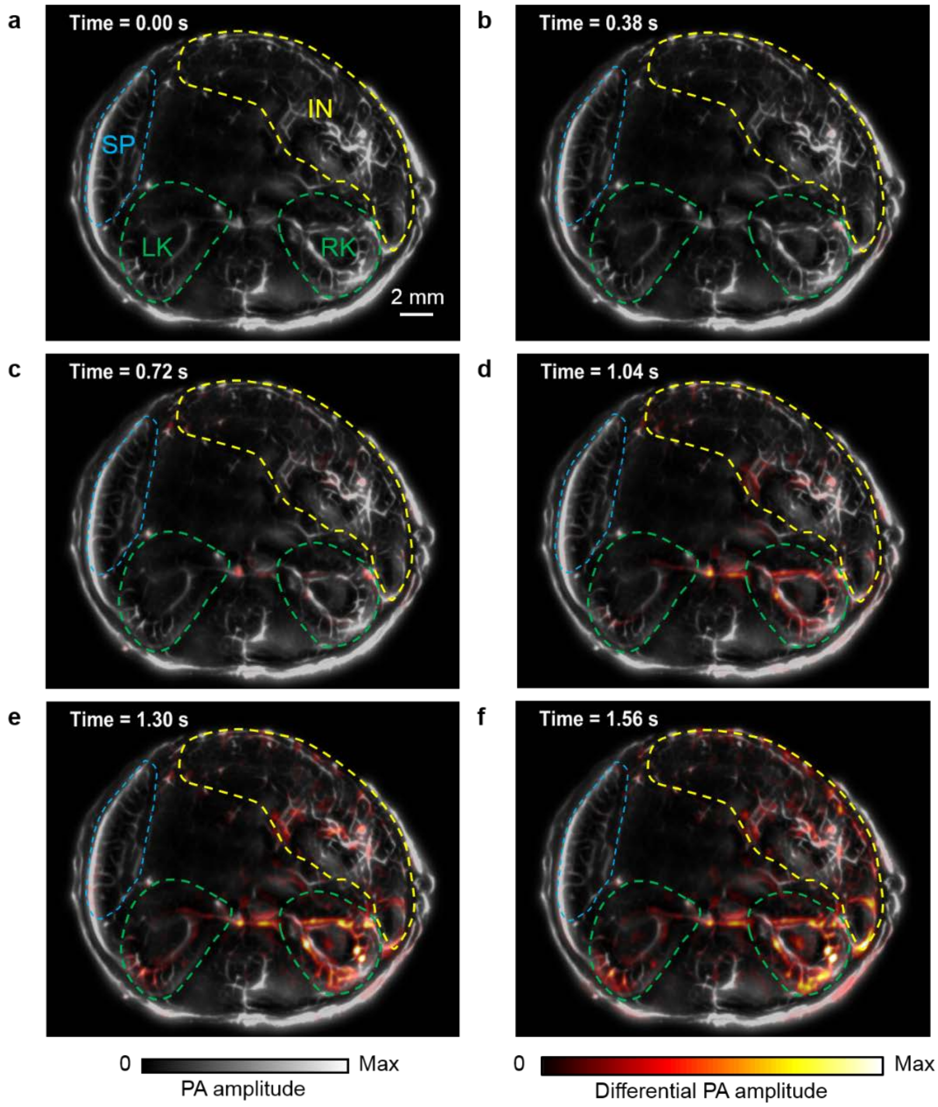
a
Time = 0.00 s
SP
IN
LK
RK
2 mm
b
Time = 0.38 s
c
Time = 0.72 s
d
Time = 1.04 s
e
Time = 1.30 s
f
Time = 1.56 s
0
Max
PA amplitude
0
Max
Differential PA amplitude

Figure 31. Visualization of whole-body dye perfusion. (a–f) Cross-sectional images of the lower abdominal cavity at different times after injection of dye solution, showing that dye molecules perfused to both kidneys and the intestinal region. IN, intestine; LK, left kidney; RK, right kidney; SP, spleen.

Superresolution PACT by localization of single dyed droplets

The spatial resolution of PACT is fundamentally limited by acoustic diffraction and, thus, by the acoustic wavelength in tissue. Although finer resolution can be realized by detecting higher frequency ultrasound, the associated increase in ultrasound attenuation decreases the penetration depth [102, 103]. Inspired by superresolution fluorescence imaging techniques, such as photoactivation localization microscopy (PALM) and stochastic optical reconstruction microscopy (STORM) [104, 105], several techniques have been used to break the acoustic diffraction limit in PACT. One such technique utilized the PA signal fluctuations that were induced by either speckle illumination or flowing absorbers [106, 107]. More recently, superresolution PA imaging has also been demonstrated by the localization of flowing microbeads [108, 109]. However, none of these techniques have been successfully applied to *in vivo* imaging. The main disadvantage of the fluctuation-based technique is that the speckle contrast becomes too low for detection in deep tissue due to the orders of magnitude smaller size of the fully developed speckle grains compared to the detection acoustic wavelength. Moreover, one of the main drawbacks of the bead-based localization technique is that solid beads can jam small blood vessels and block blood flow, thereby impeding *in vivo* applications. Here, we used flowing single dyed droplets for localization to enhance the spatial resolution [25].

The droplets were prepared by mixing oil-dissolved dye (IR-780) with water. The molar absorption coefficient of the IR-780 iodide dye solution is 300 times higher than that of hemoglobin (80% oxy-hemoglobin and 20% deoxy-hemoglobin) at 780 nm (**Fig. 32**). Based on the normal hemoglobin concentration (150 g L^{-1}) in whole blood and the gram-molecular weight of hemoglobin (64,500 g mole^{-1}) [110], the absorption coefficient of the dye solution at 2 mM is approximately 260 times higher than that of whole blood.

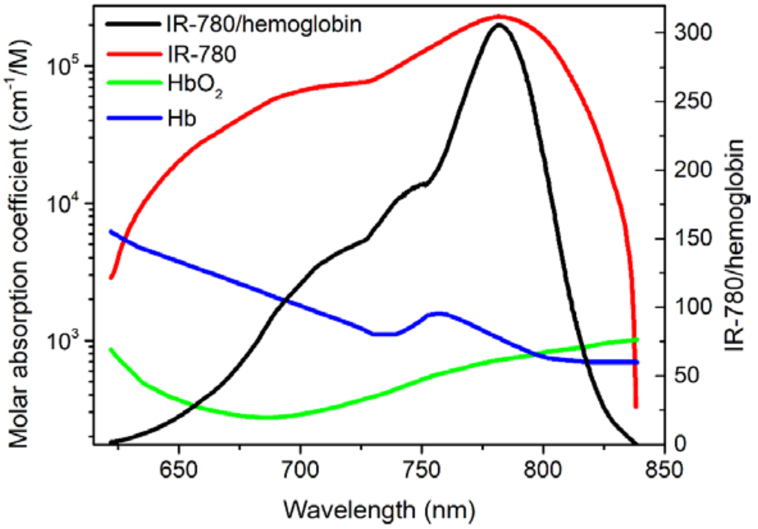

Figure 32. Absorption spectra of HbO_2, HbR, and IR-780 dye solution as well as the absorption coefficient ratio of IR-780 to hemoglobin (80% HbO_2 and 20% HbR).

In the *in vivo* study, droplets were used to improve the spatial resolution in PACT of a mouse brain vasculature. The mouse brain was initially imaged using hemoglobin as the endogenous optical contrast. The laser was tuned to 780 nm, and the pulsed energy was set to 100 mJ. The optical fluence on the head surface was 30 mJ cm^{-2}. The reconstructed image based on hemoglobin contrast is shown in **Fig. 33a**. To quantify the spatial resolution, we plotted the profile of the PA amplitude along the dashed line, where a small vessel began to bifurcate into two. The distance between the two peaks in **Fig. 33b** corresponds to a spatial resolution of approximately 150 µm. Then, the brain was continuously imaged, while droplets were injected into the heart through the catheter. **Fig. 33c** shows a droplet that is flowing in a vessel over time. The droplet flow direction and speed were quantified from the time-lapse images. Due to the high droplet flow speed and the relatively low imaging frame rate (20 Hz), droplets sometimes traveled through a vessel in only a few imaging time points. Therefore, the spatial resolution of the flow speed mapping is low. As shown in **Fig. 33d**, the droplet flow speed in the cortex was 1.3-7.5 mm s^{-1}, which well accords with the previously reported blood flow speed in the cortex [111, 112]. The flow speed that was determined in this way was extracted from multiple droplets; some droplets flowed even faster and reached 26 mm s^{-1} in some vessels. Interestingly, the droplets in the upper and lower parts of the superior sagittal sinus flowed in opposite directions; a possible reason is that vessels from different depths that had different flow directions overlapped with each other.

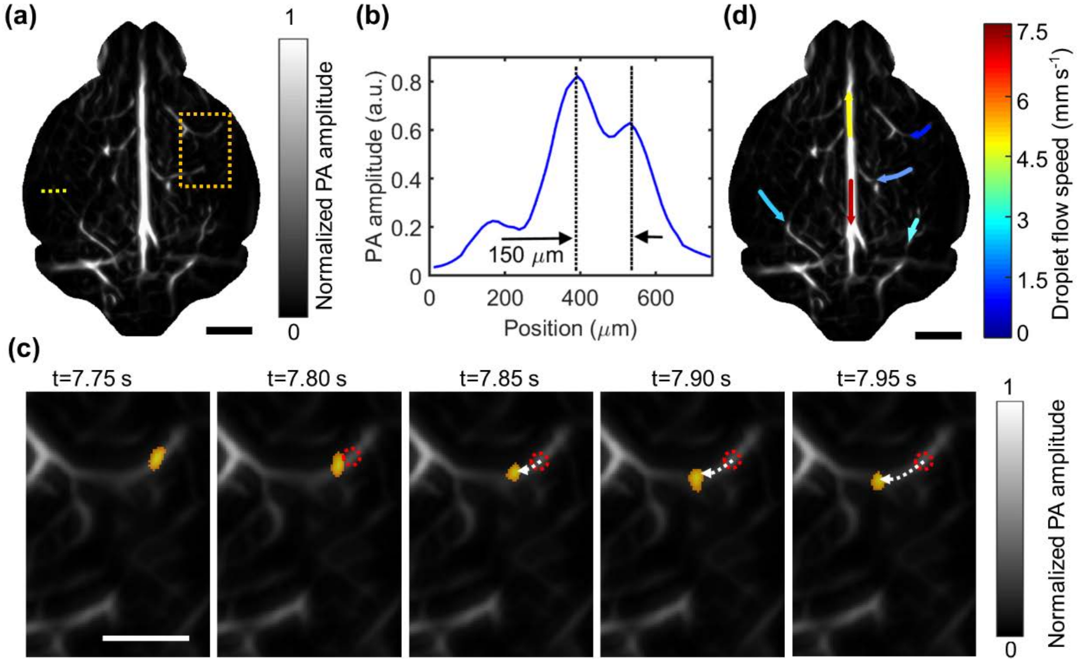
(a)
1
Normalized PA amplitude
0
(b)
PA amplitude (a.u.)
0.8
0.6
0.4
0.2
0
0
200
400
600
Position (μm)
150 μm
(d)
7.5
6
4.5
3
1.5
0
Droplet flow speed (mm s^{-1})
(c)
t=7.75 s
t=7.80 s
t=7.85 s
t=7.90 s
t=7.95 s
1
Normalized PA amplitude
0

Figure 33. Tracking of single dyed droplets in the brain *in vivo*. (a) A unipolar image of the baseline cortical vasculature that was acquired prior to the injection of droplets. (b) A profile of the PA amplitude along the dashed line in (a). (c) The flow of a droplet (orange dot) in brain vessels, which was tracked over time. The droplet images were overlaid on the baseline vascular image in the region that is bounded by the dashed rectangle in (a). The dotted red circles indicate the initial locations of the droplets, and the dashed arrows indicate the flow pathway and direction. (d) The droplet flow velocities for several cortical vessels. The colors indicate the flow speeds, and the arrows indicate the flow directions. The scale bars are 2, 1 and 2 mm in (a), (c) and (d), respectively.

The extracted images of single droplets were analyzed by 2-D Gaussian fitting, and their centers were identified. In total, approximately 220,000 droplets were localized during the half-hour data acquisition, and their centers were used to construct a superresolution image. **Fig. 34a** and **b** show the images of the cortical-layer vessels that were obtained via conventional PACT and superresolution PACT, respectively. Compared with **Fig. 34a**, **Fig. 34b** shows substantial improvements in spatial resolution. **Figure 34c shows** the amplitude profiles the dotted lines in **Fig. 34a** and **b**. In the superresolution image, the vessels appear sharper, and the closely neighboring vessels can be resolved. The droplet-localization technique not only improves the PACT resolution but also lights up the vessels that are otherwise obscured by the blood background. **Figure. 34d** and **e** show the magnified images of the regions that are bounded by dotted rectangles in **Fig. 34a** and **b**, respectively. While no features can be readily identified in the conventional image (**Fig. 34d**), the superresolution image displays bifurcated vessels (**Fig. 34e**). The amplitude profiles along the dotted lines are shown in **Fig. 34f**, according to which the two vessels, which are separated by 25 µm, can be resolved by the droplet-localization technique. These results suggest that the spatial resolution of PACT has been improved by a factor of 6 by the localization of single droplets.

It is possible to improve droplet-localization PACT further. First, dyed droplets with higher optical absorption would increase the spatial resolution due to the inverse relationship between the localization precision and the CNR of single droplets [113]. Thus, photoacoustically brighter dye at a longer wavelength (1.0–1.7 µm) would enable superresolution imaging of the vasculature in deeper tissue. Second, the sizes of the droplets are dispersed in this work, and many small droplets generated a background in the PACT images, thereby degrading the localization precision. This problem could be circumvented by generating mono-dispersed droplets using a microfluidic device [114]. Third, some droplets displayed moon-like shapes, which was probably due to their deviation from the focal plane of the transducers; thus, 2-D Gaussian fitting to these images produced a bias in their center estimation. An estimator with less bias is required for processing the images of these droplets. Fourth, the current imaging frame rate is 20 Hz, which is limited by the laser repetition rate. Although the droplets move slowly in terms of absolute speed (1.3–7.5 mm s^{-1}), they move fast on a superresolution scale, i.e., the droplets displace 1/2 of the superresolution pixel width (25 µm/2) over a short time interval. Capturing the minute displacement accurately requires high frame rates. Moreover, a high frame rate can effectively reduce the data acquisition time and facilitate the removal of the artifacts that resulted from the limited number of localized droplets. We expect the droplet-localization PACT to find wide applications in imaging blood vessels and monitoring targeted drug delivery in deep tissue.

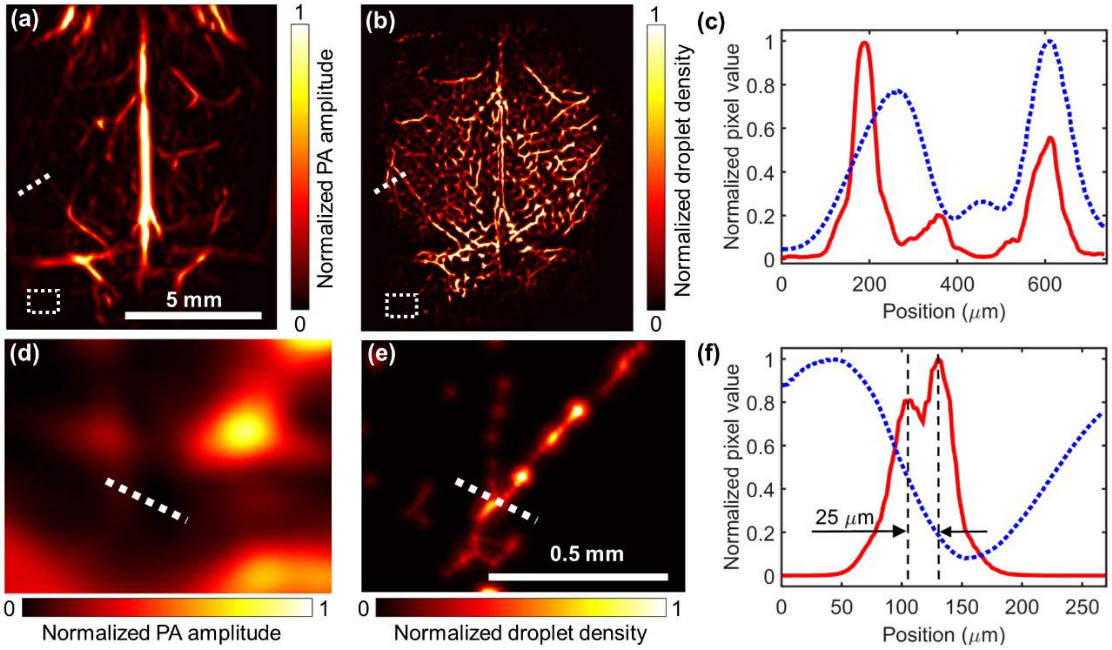
(a)
5 mm
1
0
Normalized PA amplitude
(b)
1
0
Normalized droplet density
(c)
Normalized pixel value
0
0.2
0.4
0.6
0.8
1
0
200
400
600
Position (μm)
(d)
0
1
Normalized PA amplitude
(e)
0.5 mm
0
1
Normalized droplet density
(f)
Normalized pixel value
0
0.2
0.4
0.6
0.8
1
25 μm
0
50
100
150
200
250
Position (μm)

Figure 34. Superresolution imaging of the mouse brain cortex. (a) A unipolar image of the cortical layer that was acquired by conventional PACT using hemoglobin as the contrast. (b) A superresolution PACT image of the cortical layer by localizing single droplets. (c) Amplitude profiles of the conventional image (blue dashed line) and the superresolution image (red solid line) along the dotted lines that are shown in (a) and (b). (d and e) Magnified images of the regions that are bounded by dotted rectangles in (a) and (b). (f) Amplitude profiles along the dotted lines in (d) and (e), where the red solid line corresponds to the profile from the superresolution image, the blue dashed line corresponds to the profile from the conventional image, and the vertical black dashed lines indicate the locations of the two vessels.

PACT of microparticles—metallic microrobots

Recently, tremendous progress in synthetic micro/nanomotors in diverse environment has been made for potential biomedical applications. However, existing micro/nanomotor platforms are inefficient for deep tissue imaging and motion control *in vivo*. Here, we present a SIP-PACT guided investigation of micromotors in intestines *in vivo*. The micromotors capsules (MCs) are stable in the stomach, and the micromotors exhibit efficient propulsion in various biofluids once released from the MCs.

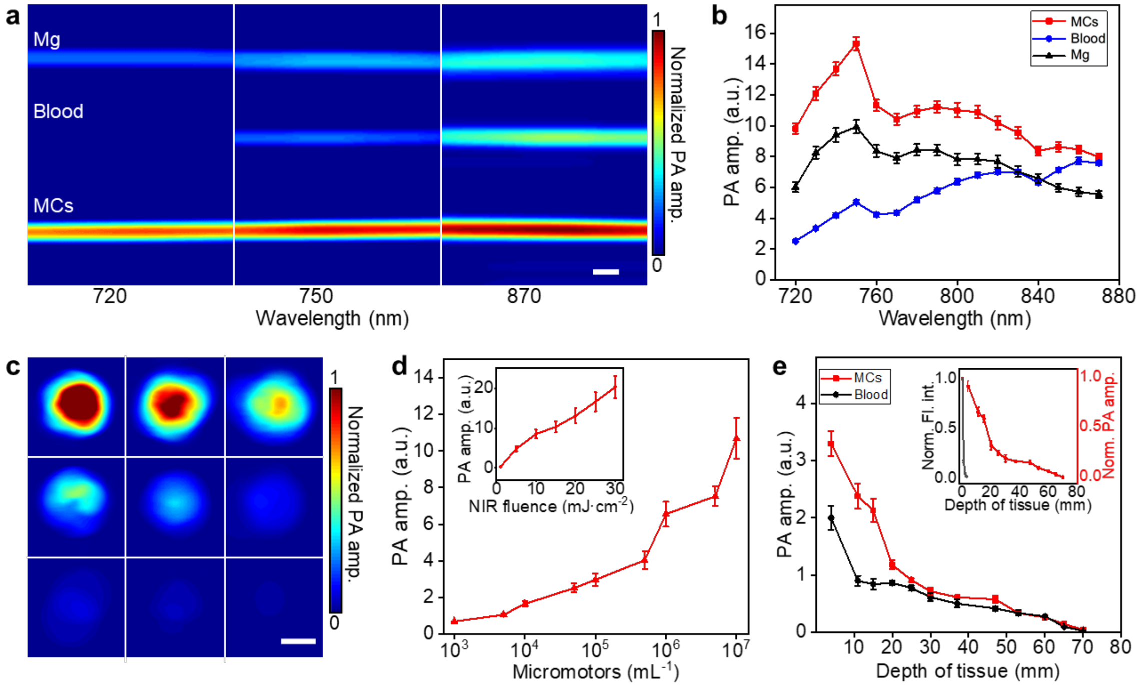

Figure 35. PA characterization of the MCs. (a) PACT images of Mg particles, blood, and MCs in silicone rubber tubes with laser wavelengths at 720, 750, and 870 nm, respectively. Scale bar, 500 µm. (b) PACT spectra of MCs (red line), blood (blue line), and Mg particles (black line), respectively. (c and d) PACT images (c) and the corresponding PA amplitude (d) of the MCs with different micromotor loading amount, and the dependence of the PA amplitude on the fluence of NIR light illumination (inset in d). Scale bar in c, 500 µm. (e) Dependence of PA amplitude of the MCs (red line) and blood (black line) on the depth of tissue, and the normalized PA amplitude and fluorescence intensity of the MCs under tissue (inset). Norm., normalized; amp., amplitude; Fl., fluorescence; int., intensity.

For deep tissue imaging *in vivo*, it is crucial that the MCs should have higher optical absorption than that of the blood background. As shown in **Fig. 35a**, the MCs exhibit strong PA contrast within the NIR wavelength region, ranging from 720 to 890 nm. In order to quantitatively assess the optical absorption of the MCs, we extracted amplitude values from above PA images and subsequently calibrated with optical absorption of hemoglobin [115, 116]. At the wavelength of 750 nm, the MCs display the highest PA amplitude (**Fig. 35b**). The PA signals of the MCs peak at 750 nm with an amplitude of 15.3. The bare Mg particles display a similar PA spectrum, with a lower PA peak with an amplitude of 10.0 at 750 nm. The higher PA amplitude of the MCs than that of bare Mg particles indicates that the Au layer significantly improves the imaging sensitivity owing to its strong optical absorption in the NIR wavelength region (**Fig. 35b**) [117, 118]. In addition, the approximate 3-fold increase in PA amplitudes of the MCs (compared to that of the whole blood) provides sufficient contrast for PACT to detect *in vivo* using 750-nm illumination. **Fig. 35c** and **d** show the PA images and the corresponding PA amplitudes of single MCs with different concentrations of micromotors. The dependence of the PA amplitude on the NIR light fluence was also investigated. As expected, the PA amplitude of the micromotors almost linearly increases with the NIR light fluence (**Fig. 35d, inset**). We also studied the maximum detectable depth of MCs using PACT (**Fig. 35e**). The fluorescence intensity of micromotors dramatically decreased when covered by thin tissue (0.7–2.4 mm in thickness) and became undetectable quickly (**Fig. 35e, inset**). By contrast, PACT can image the micromotors inside tissue deep to ~7 cm (**Fig. 35e**), which reveals that the key advantage of PACT lies in the high spatial resolution and high molecular contrast imaging inside deep tissue [4].

The movement of a swarm of MCs was monitored *in vivo* by the PACT. The MCs were dispersed in pure water and then orally administered into 5–6-week old nude mice. The mice were subsequently anesthetized and the lower abdominal cavity was aligned with the imaging plane of the ultrasonic transducer array for longitudinal imaging. PACT images were captured at a frame rate of 2 Hz for ~8 hours. As shown in **Fig. 36a**, the blood vessels and background tissue are shown in gray and MCs in intestines are highlighted in color. During the imaging period of the first 6 hours, the MCs migrated for ~1.2 cm, roughly 15% of the length of the entire small intestine. After 5 hours, the PA signals of some MCs faded away as they moved downstream in intestines that were outside of the imaging plane. The moving speed of the swarm MCs in intestines and the movements induced by respiratory motion were quantified (**Fig. 36b–d**,). As shown in **Fig. 36b–d**, the abrupt motion caused by respiration is much faster than real migration of the MCs. Despite the respiration-induced movement, PACT can distinguish the signals from the slowly migrating MCs in intestines. These results indicate that PACT can precisely monitor and track the locations of the MCs in the deep tissue *in vivo*.

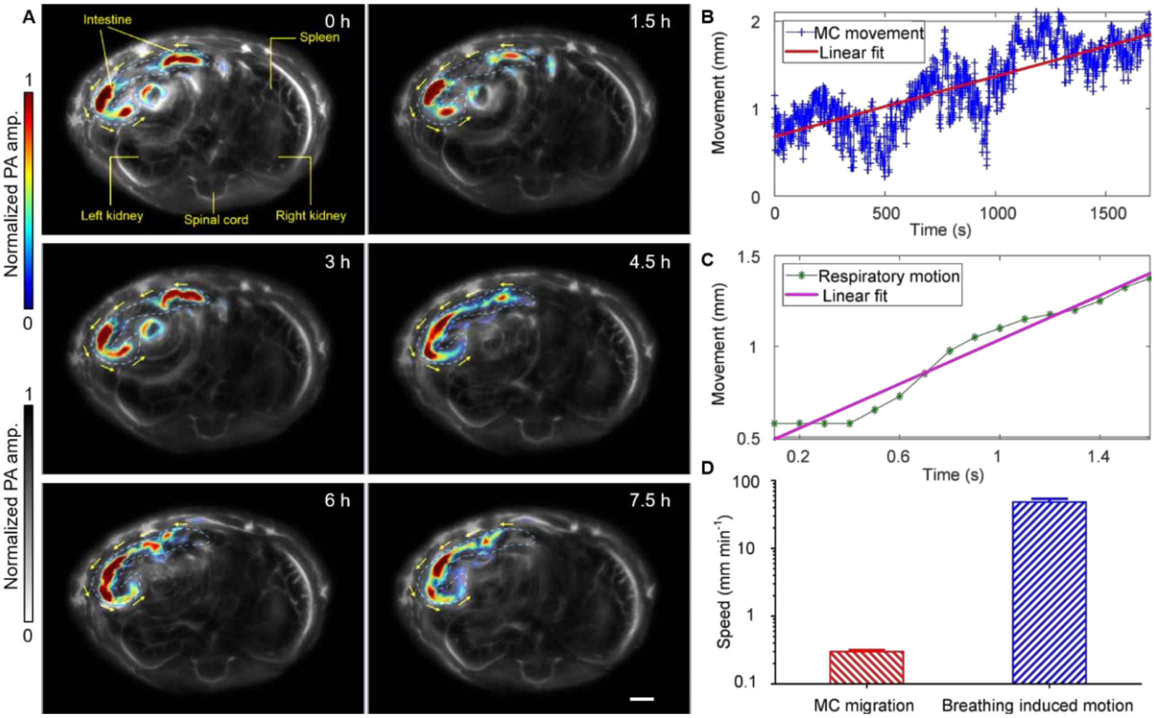
A
Intestine
0 h
Spleen
1.5 h
Normalized PA amp.
1
0
Left kidney
Spinal cord
Right kidney
3 h
4.5 h
Normalized PA amp.
1
0
6 h
7.5 h
B
MC movement
Linear fit
Movement (mm)
2
1
0
0
500
1000
1500
Time (s)
C
Respiratory motion
Linear fit
Movement (mm)
1.5
1
0.5
0.2
0.6
1
1.4
Time (s)
D
Speed (mm min^{-1})
100
10
1
0.1
MC migration
Breathing induced motion

Figure 36. PACT evaluation of the MC dynamics *in vivo*. (a) The time-lapse PACT images of the MCs in intestines for 7.5 hours. The MCs migrating in the intestine are shown in color, the mouse tissue is shown in gray. Scale bar, 2 mm. (b and c) The movement displacement caused by the migration of the MCs in the intestine (b) and by the respiration motion of the mouse (c). (d) Comparison of the speeds of the MC migration and the respiration-induced movement.

PACT has visualized the migration of MCs toward the targeted regions in intestines *in vivo*, which provides a real-time navigation of the MCs for precise control and promises practical biomedical applications, such as drug delivery.

PACT of genetically encoded photoswitchable proteins

Enhancing detection sensitivity and specificity

By using reporter genes expressed in targeted biological processes, optical imaging has provided valuable information for biomedical studies [119, 120]. PAT is inherently suited for molecular imaging by using genetically encoded probes that are either fluorescent or not, such as fluorescent proteins (FPs) and non-fluorescent pigments [121, 122]. Most notably, PAT of the genetically encoded probes typically has strong background signals from hemoglobin which exhibits wideband absorption spectrum that overlap with those of the probes [121-123]. Accurate spectral unmixing of these biomolecules is prevented by highly wavelength-dependent light attenuation in tissue at depths [124]. To overcome these limitations, optically probes with the following characteristics are highly desired in PAT: (*i*) Genetically encodable expression, (*ii*) spectral properties that allow light penetration to deep tissue and robust unmixing from other endogenous biomolecules, (*iii*) light-sensing chromophores that are naturally present in tissue, (*iv*) orthogonality to mammalian cell metabolism and low cytotoxicity. Fortunately, bacterial phytochromes (BphPs), among the very few light-sensing protein classes, can meet these criteria [26].

BphPs are photoreceptors sensitive to 600–800 nm light [125], a wavelength range that partially falls into the deep-penetration optical window in tissue [126]. BphPs consist of a photosensory core module and an output effector domain (**Fig. 37a**). The unique spectral properties of BphPs are defined by a covalently attached chromophore, biliverdin IXα (BV) [127], a product of enzymatic heme degradation (**Fig. 37b**). BV is abundant in mammalian cells [128]. Covalent binding of BV with the photosensory module is autocatalytic without any additional cofactors [129]. Inside a chromophore binding pocket, BV can adopt two conformational states, Pfr and Pr, which differ in the conformation of the C15/16 double bond between the C and D pyrrole rings (**Fig. 37c**) [130]. Photoisomerization of the D ring results in absorption shift towards the NIR region. For unbound BV molecules in cells, photoisomerization occurs around the central methane bridge with a short lifetime (on the level of milliseconds), resulting in virtually the same absorption spectra as that in the ground state (**Fig. 37d**).

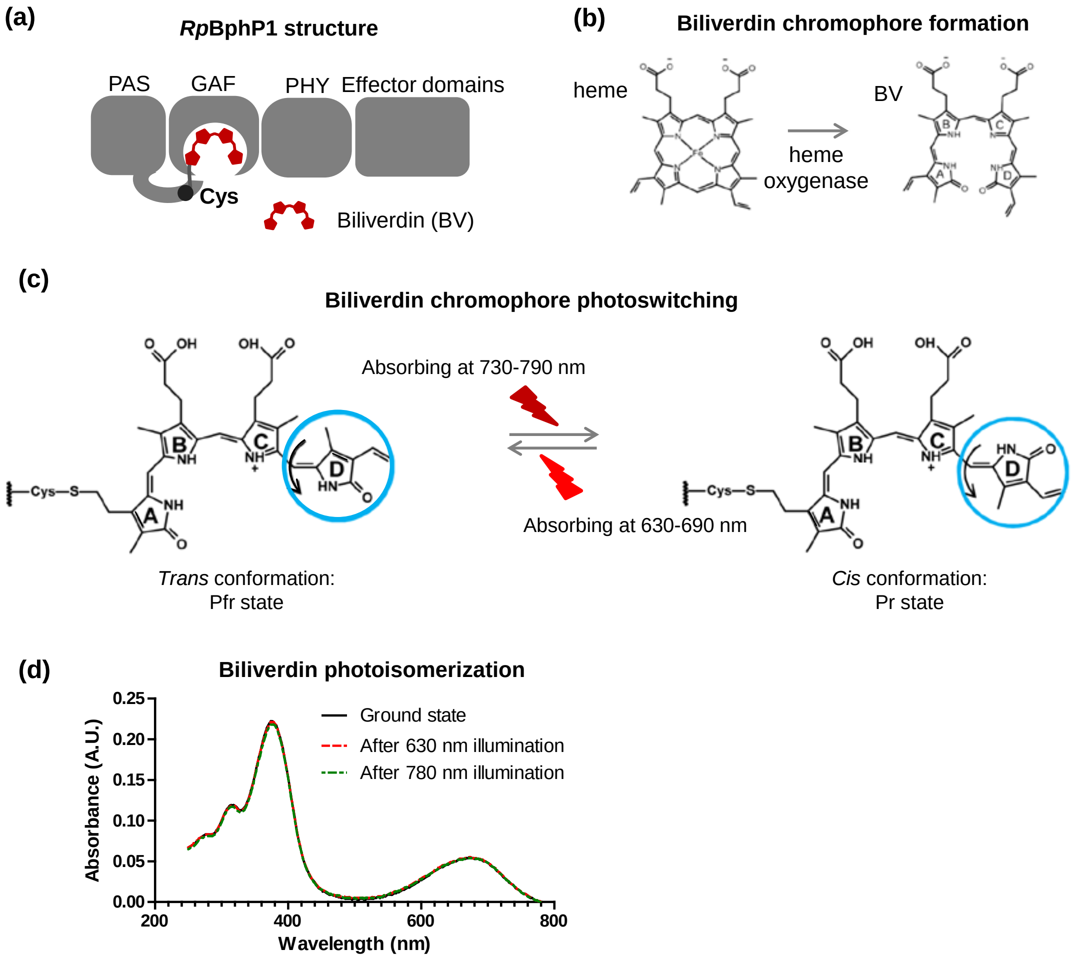
(a)
RpBphP1 structure
PAS
GAF
PHY
Effector domains
Cys
Biliverdin (BV)
(b)
Biliverdin chromophore formation
heme
heme oxygenase
BV
(c)
Biliverdin chromophore photoswitching
Absorbing at 730-790 nm
Absorbing at 630-690 nm
Trans conformation: Pfr state
Cis conformation: Pr state
Cys—S
A
B
C
D
(d)
Biliverdin photoisomerization
Ground state
After 630 nm illumination
After 780 nm illumination
Absorbance (A.U.)
0.25
0.20
0.15
0.10
0.05
0.00
200
400
600
800
Wavelength (nm)

Figure 37. Structure and photochemical properties of *Rp*BphP1 bacterial phytochrome. **(**a) Organization of a monomer subunit of *Rp*BphP1. (b) Enzymatic synthesis of BV from a heme. (c) Photoswitchings of a BV chromophore from the Pfr state to the Pr state, and vice versa, induced by NIR (~730-790 nm) light and far-red (~630-690 nm) light illumination, respectively. The photoswitchings result from the out-of-plane rotation (black arrows) of the D-ring of BV about the adjacent C15/16 double bond between the C and D pyrrole rings. (d) Absorption spectra of unbound BV photoisomerization in solution measured by a standard spectrophotometer. There is virtually no change in the spectra after 5 min illumination at 630 nm and 780 nm.

*Rp*BphP1 phytochrome from the bacterium *Rhodopseudomonas palustris* (referred to as BphP1) has a natural photochromic behavior: it adopts a Pfr state as the ground state, and undergoes the Pfr→Pr photoconversion upon 730–790 nm light illumination and the Pr→Pfr photoconversion upon 630–690 nm light illumination. From here on, we choose the Pfr state of BphP1 as the ON state, and the Pr state as the OFF state, and used 780 nm light for Pfr→Pr photoconversion and 630 nm light for Pr→Pfr photoconversion. The molar extinction coefficients of the ON state BphP1 at 780 nm and of the OFF-state at 630 nm are respectively ~70-fold and ~40-fold higher than that of HbO_2 (**Fig. 38a**). We first studied the reversible photoswitching of BphP1 between the ON and OFF states by measuring its optical absorbance at 780 nm (Online Methods). The optical absorbance shows an exponential decay from ON to OFF under 780 nm switching illumination, and an exponential recovery from OFF to ON under 630 nm switching illumination, multiple switching cycles did not cause photobleaching of BphP1 (**Fig. 38b**).

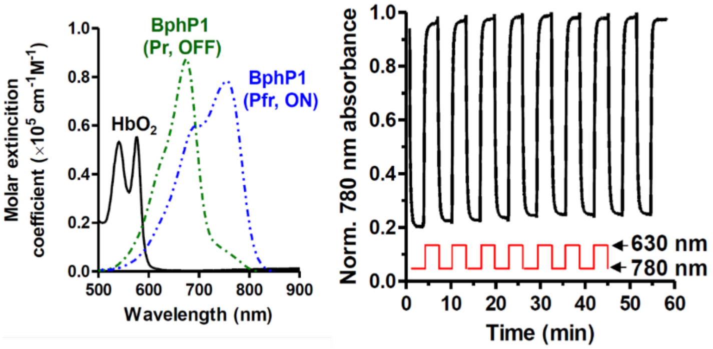

Figure 38. Optical properties of reversible photoswitching of BphP1. (a) Molar extinction spectra of HbO_2, HbR, Pfr (ON) and Pr (OFF) state BphP1. (b) Absorbance of BphP1 at 780 nm, switched off with 780 nm light illumination and then switched on with 630 nm light illumination.

We used U87 human glioblastoma cells to stably express BphP1. Because BphP1 is non-fluorescent, we used a plasmid containing an internal ribosome entry site between BphP1 and EGFP. Both genes were translated from a single bicistronic mRNA (**Fig. 39a**). The co-expressed EGFP was utilized for selecting stable BphP1-expressing cells, for studying the cytotoxicity of BphP1, and for histologically validating the PA imaging. We imaged BphP1-expressing U87 cells and whole bovine blood embedded in scattering media (1% intralipid, 10% gelatin, and 2% oxygenated bovine blood in distilled water; absorption coefficient of 0.1 cm^{-1}; reduced scattering coefficient of ~10 cm^{-1}) at 10 mm depth using PACT. The PA images acquired before and after the photoswitching both had strong background signals, resulting in poor image contrast of the U87 cells (**Fig. 39b**). However, the differential image, averaged over 20 switching cycles, largely removed the non-switchable background signals and achieved a 50-fold enhancement in CNR (**Fig. 39c**). Multiple switching cycles did not cause detectable photobleaching of the cells (**Fig. 39d**). By gradually decreasing the number of U87 cells, we observed a noise-equivalent detection sensitivity of ~20 cells by using differential PA imaging (**Fig. 40a**).

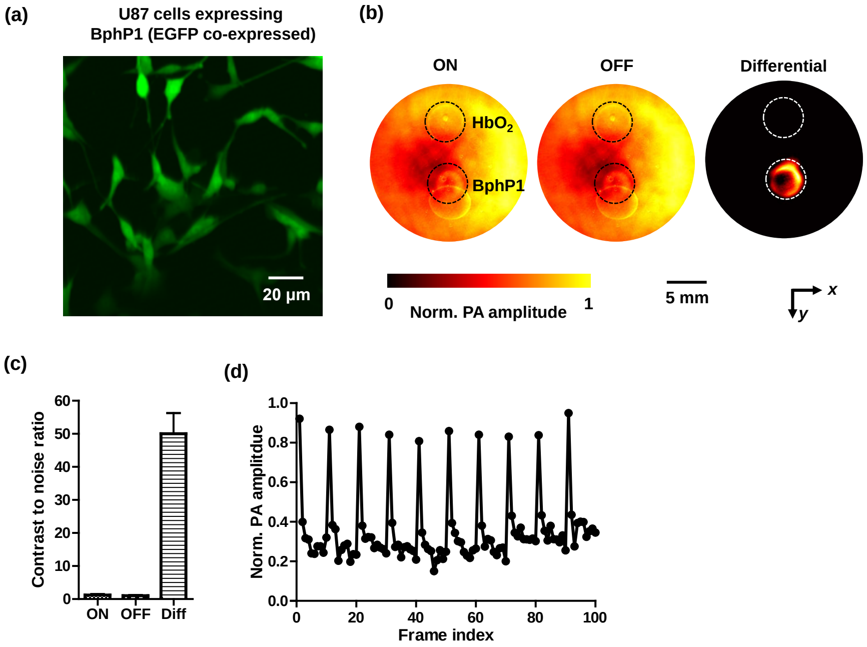

Figure 39. PACT of BphP1-expressing U87 cells at 10 mm depth. (a) Fluorescence microscopic image of the BphP1-expressing U87 cells, where EGFP was co-expressed, providing the fluorescence signal. (b) PA images of U87 cells and HbO_2 placed at 10 mm depth in scattering media mixed with blood to provide background signal. The differential image effectively eliminates the background signals and clearly shows the U87 cells that are otherwise not detectable in the ON and OFF state images. (c) Contrast to noise ratio quantified from the ON state, OFF state, and differential (Diff) PA images. (d) PA signals of BphP1-expressing U87 cells observed over 10 photoswitching cycles.

We next evaluated photoswitching of BphP1 using PACT. We imaged a mouse one week after injection of 10^6 BphP1-expressing U87 cells into the left kidney. Major organs, including the skin, kidneys, spleen, bladder, and spinal cord, could be delineated with strong signals from blood (**Fig. 40b**). However, the U87 tumor in the left kidney, overwhelmed by the blood signals, could not be detected. After 20-cycle photoswitching, the differential PA image clearly showed the tumor at a depth up to ~8 mm, with an average CNR of ~20 (**Fig.**

40c). The photoswitchable tumor had different signals in the ON and OFF state images, while the non-switchable background signals from blood were virtually identical (**Fig. 40d**). After PA imaging, the tumor was histologically confirmed (**Fig. 40e**). The superior sensitivity of BphP1-based PACT was further demonstrated by imaging an otherwise undetectable U87 tumor in a mouse brain, at ~3 mm depth beneath the scalp surface (**Fig. 40f**).

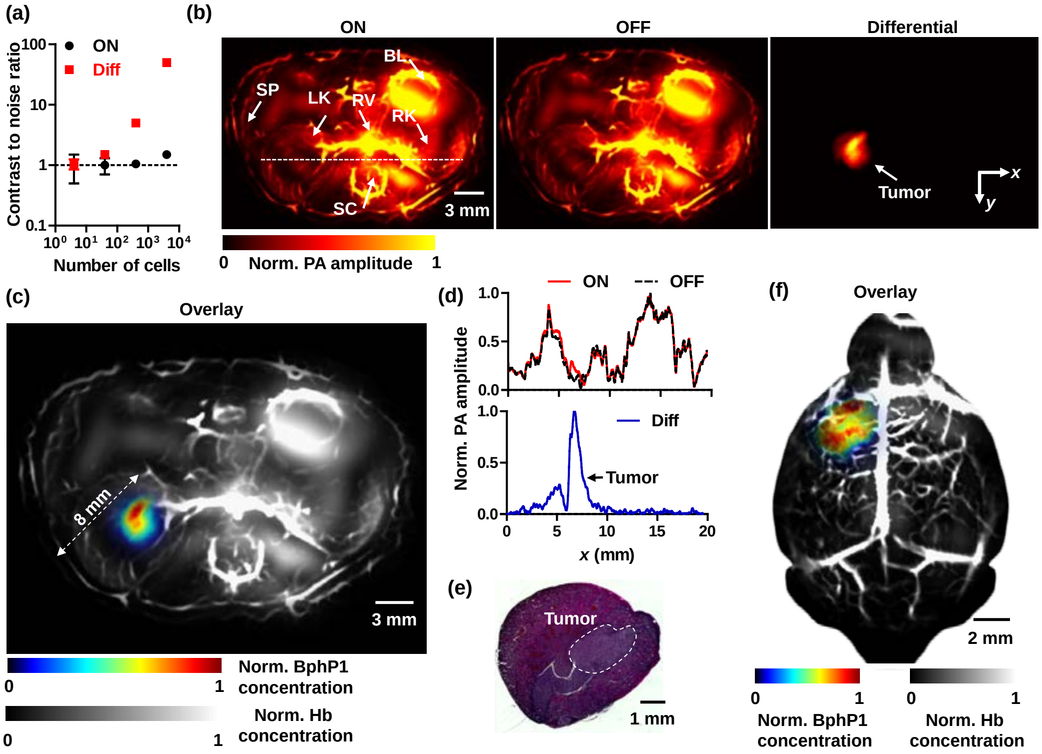
(a)
Contrast to noise ratio
100
10
1
0.1
ON
Diff
10^0 10^1 10^2 10^3 10^4
Number of cells
(b)
ON
OFF
Differential
BL
SP
LK
RV
RK
SC
3 mm
Tumor
x
y
0
Norm. PA amplitude
1
(c)
Overlay
8 mm
3 mm
0
1
Norm. BphP1 concentration
0
1
Norm. Hb concentration
(d)
ON
OFF
1.0
0.5
0.0
Norm. PA amplitude
Diff
Tumor
0
5
10
15
20
x (mm)
(e)
Tumor
1 mm
(f)
Overlay
2 mm
0
1
Norm. BphP1 concentration
0
1
Norm. Hb concentration

Figure 40. Deep PACT of genetically encoded reversibly switchable BphP1 *in vivo*. (a) PA CNR of BphP1-expressing U87 cells embedded at 10 mm depth versus increasing cell counts. (b) *In vivo* whole-body PACT images of the kidney region of a nude mouse, acquired one week after injection of ~10^6 BphP1-expressing U87 cells into the left kidney. The ON and OFF state PA images clearly show the major blood-enriched internal organs, including the left kidney (LK), right kidney (RK), spinal cord (SC), renal vein (RV), bladder (BL), and spleen (SP). The differential image clearly reveals the tumor in the left kidney. (c) An overlay of the U87 tumor (shown in color) in the left kidney and the blood-dominated OFF state image (shown in gray). (d) Normalized signal profiles of the ON state, OFF state, and differential images along the white dashed line in (b). (e) A representative H&E histological image of the harvested left kidney, showing the tumor region. (f) Deep PACT of a mouse brain U87 tumor expressing BphP1. The tumor (shown

in color) was ~3 mm beneath the scalp surface. A global threshold was applied to all the differential images with a threshold level at three times the noise level.

Structurally, BphP proteins consist of a photosensory core module (PCM) and various so-called effector domains (**Fig. 41**) [131-133]. The PAS (Per-ARNT-Sim), GAF (cGMP phosphodiesterase/adenylate cyclase/FhlA), and PHY (phytochrome-specific) protein domains connected with α-helix linkers form the PCM, which typically has a molecular weight of 55-58 kDa. The previously describe RpBphP1 consists of the PCM and two additional effector domains, named the PAS/PAC and HOS domains, and forms a dimer [134]. Moreover, the HOS domain of one monomer interacts with the PCM of another monomer in the dimer. Because of its high molecular weight of ~82 kDa, RpBphP1 exhibits a limited folding efficiency and low expression level in mammalian cells. Attempts to delete the HOS domain resulted in the loss of photochromic behavior, suggesting that photoswitching requires HOS binding to PCM. This finding was surprising, because in some BphPs, deletion of the effector domains does not affect reversible photoswitching, and only further truncation of the PHY domain starts to impair it [135, 136]. A PCM part of the DrBphP phytochrome from *Deinococcus radiodurans* (termed DrBphP-PCM below) does not interact with effector domains, preserves photochromism without effector domains, and is 1.5 times smaller than RpBphP1 (**Fig. 41**). These features make it an attractive template for engineering advanced PA probes [137].

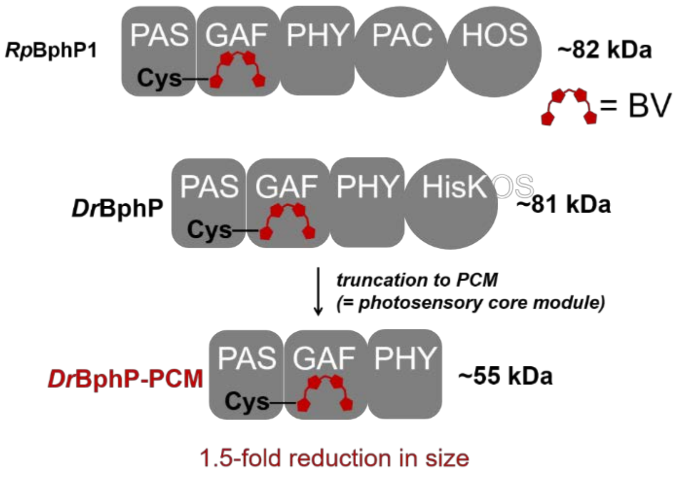
*Rp*BphP1
PAS
GAF
PHY
PAC
HOS
Cys
~82 kDa
= BV
*Dr*BphP
PAS
GAF
PHY
HisKOS
Cys
~81 kDa
truncation to PCM
(= photosensory core module)
*Dr*BphP-PCM
PAS
GAF
PHY
Cys
~55 kDa
1.5-fold reduction in size

Figure 41. Development of a 1.5-fold smaller photochromic probe for PA imaging. Monomers (shown) of naturally dimeric bacterial phytochromes (BphPs) share a common domain structure. It is represented here by the photosensory core module (PCM), formed by the PAS-GAF-PHY domain triad, and output domains. BV is covalently bound with conservative cysteine from the PAS domain and secured to a chromophore-binding pocket in the GAF domain. The molecular weight of the BphPs monomer is ~80 kDa. RpBphP1, consists of the regular PCM and the output PAS/PAS and HOS domains. The domain organization of BphP from Deinococcus radiodurans, DrBphP, is comprised of the PCM and the output histidine kinase (HisK) domain. We truncated full-length DrBphP to its PCM and called the result DrBphP-PCM, achieving a 1.5-fold reduction in the molecular weight of the PA probe.

To characterize DrBphP-PCM as a PA probe and compare it with RpBphP1, we upgraded SIP-PACT for real-time reversible photoswitching, detection of photoswitching rates, and imaging. In order to image RpBphP1, DrBphP-PCM proteins, we combined a Ti:Sapphire laser and an optical parametric oscillator (OPO) for illumination. These two lasers were synchronized and triggered by an FPGA-based controller. Due to the high imaging speed of SIP-PACT, we are able to capture the entire photoswitching process of the BphPs in real time, which enables temporal frequency analysis—frequency lock-in reconstruction (LIR). The result is a better CNR in the images of BphPs, and a reduction in the impacts of motion (*e.g.*, from respiration and heart beating) during *in vivo* imaging.

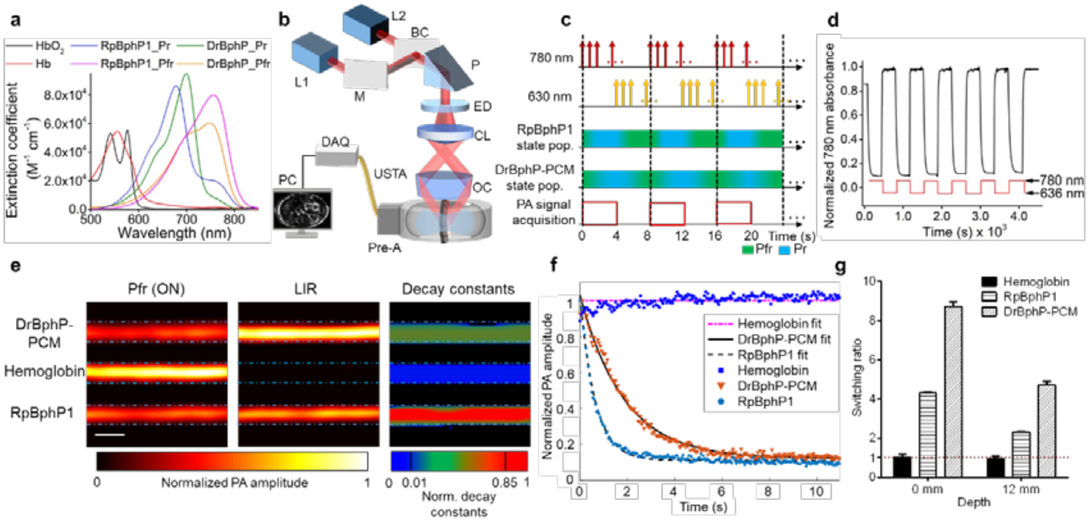

Figure 42. Spectral and PA characterization of the DrBphP-PCM. (a) Molar extinction spectra of HbO$_2$, HbR, Pfr (ON) and Pr (OFF) state of DrBphP-PCM and RpBphP1. (b)

Schematic of the whole-body PACT system. BC, beam combiner; CL, conical lens; DAQ, data acquisition unit; ED, engineering diffuser; M, mirror; OC, optical condenser; P, prism; PC, personal computer; pre-A, pre-amplifier; USTA, ultrasonic transducer array. L1, the Ti:Sapphire laser. L2, the optical parametric oscillator (OPO) laser. (c) Time sequence of photoswitching and imaging of BphPs (pop., population). (d) Absorbance of DrBphP-PCM at 780 nm. (e) PA images of BphPs and hemoglobin in clear media. Left column: ON state PA image of BphPs and hemoglobin, middle column: LIR images of BphPs and hemoglobin; right column, decay constant encoded image showing a reliable separation of DrBphP-PCM, RpBphP1, and hemoglobin. Scale bar, 500 µm. (f) PA signal changes upon 780 nm light illumination and their fits. (g) The switching ratio of BphPs and hemoglobin, defined as the PA amplitude ratio between the ON and OFF states, in both clear media (0 mm in depth) and scattering media (12 mm in depth); error bars are s.e.m. (*n* = 40).

We first measured the molar extinction coefficients for the ON states and the OFF states of DrBphP-PCM and RpBphP1. The ratios between the extinction coefficients of the ON state (Pfr form) at 780 nm and the OFF state (Pr form) at 630 nm of DrBphP-PCM and RpBphP1 were 9.9 and 4.1, respectively (**Fig. 42a**). We employed 780 nm light for PA imaging and photoswitching the BphPs to the OFF state, and used 630 nm light to switch the BphPs back to the ON state (**Fig. 42b**). The laser fluence on the sample surface at both wavelengths did not exceed 12 mJ cm^{-2}, which is below the ANSI safety limit [138]. The imaging and photoswitching time sequences are shown in **Fig. 42c**. The change in RpBphP1 absorbance at 780 nm between the ON and OFF states was about four times, similar to earlier observations [139]. The changes in DrBphP-PCM absorbance at 780 nm between the ON and OFF states were two times larger than that of RpBphP1 (**Fig. 42d**), which resulted in higher PA imaging contrast (**Table 2**).

Tubes filled with DrBphP-PCM (~30 µM), hemoglobin (bovine blood with 90% oxygen saturation, sO_2) and RpBphP1 (~30 µM), respectively, were first embedded in clear gelatin (**Fig. 42e**). Although hemoglobin has the highest contrast in the ON state images (**Fig. 42e**, left column), in LIR, where a pixel-wise extraction of amplitudes of the harmonics of the illumination modulation frequency, both DrBphP-PCM and RpBphP1 signals stand out (**Fig. 42e**, middle column). The LIR method successfully separated the PA signals from two BphPs from the non-photoswitchable blood signals, even with 2.5 times higher CNR than previous differential method [139]. Typically, a threshold level of four times the noise level, estimated as the standard deviation of the background signal outside the imaged region, was globally applied to the PA LIR images. Compared to RpBphP1, DrBphP-PCM took about three times longer time to photoswitch from the ON-state to the OFF-state (**Fig. 42f** and **Table 2)**. This photochemical feature enabled separating the PA signals of DrBphP-PCM and RpBphP1 by measuring the signal decay constants during imaging. Moreover, since hemoglobin is non-photoswitchable, its decay constant was close to zero, making it even more distinguishable from the BphP-based probes in RS-SIP-PACT (**Fig. 42e**, right column). The ON-to-OFF photoswitching rate (decay constant) here is defined as the reciprocal of the time it takes for the PA signal from the protein to drop to 1/*e* of its maximum. The ON-to-OFF photoswitching rates of DrBphP-PCM and RpBphP1 were 0.54 s^{-1} and 1.56 s^{-1} respectively, as measured at a laser fluence of 4 mJ cm^{-2} at 780 nm **(Table 2**).

We further compared the reversible photoswitching of both BphPs in scattering media at depths using 780 nm illumination. Tubes filled as before were embedded at a depth of 12 mm inside a scattering medium (10% gelatin and 1% intralipid in distilled water; reduced scattering coefficient of ~10 cm^{-1}) [140]. We defined the photoswitching ratio as the ratio of the measured PA-signal amplitude of BphPs in the ON state to that in the OFF state. In both the clear medium (0 mm in depth) and scattering medium (12 mm in depth), DrBphP-PCM exhibited 2 times better photoswitching ratio than RpBphP1 (**Fig. 42g**).

Table 2. Spectral and PA properties of RpBphP1 and DrBphP-PCM *in vitro*.

Protein	Photo switching state	Maximum absorption wavelength (nm)	Maximum emission wavelength (nm)	Molar extinction coefficient (M^{-1} cm^{-1})	Fluorescence quantum yield (%)	PA excitation wavelength[a] (nm)	ON-to-OFF photoswitching rate[b] (s^{-1})	PA signal-to-noise ratio[c]		PA switching ratio[d]		Temporal frequency PA image CNR[e]	
								0 mm depth	12 mm depth	0 mm depth	12 mm depth	0 mm depth	12 mm depth
RpBphP1	Pfr (ON)	756	none	78,300	none	780	1.56	501.4 ±15.3	15.2 ±0.3	4.3 ±0.2	2.3 ±0.2	380.3 ±12.0	21.3 ±0.2
	Pr (OFF)	678	n.d.	87,500	n.d.								
DrBphP-PCM	Pfr (ON)	750	none	59,200	none	780	0.54	636.2 ±17.2	25.4 ±1.3	8.7 ±1.5	4.7 ±1.2	550.4 ±16.0	38.3 ±0.3
	Pr (OFF)	700	720	98,000	2.9%								

[a] The laser fluence was 8 mJ cm^{-2}. The wavelengths were chosen on the basis of the absorption of the proteins and the power spectra of the lasers. [b] The ON-to-OFF photoswitching rate is defined as the reciprocal of the time when the PA signal drops to 1/*e* of its maximum, measured at [a] a laser fluence of 4 mJ cm^{-2}. [c] The protein concentration was 30 µM, and the reduced scattering coefficient of the scattering media was ~10 cm^{-1}. Data are reported as mean ± s.d. [d] The switching ratio is the ratio of the PA signal amplitudes acquired in the ON and the OFF states. Data are reported as mean ± s.d. The hemoglobin concentration was 2.3 mM. Data are reported as mean ± s.d.

We next used SIP-PACT to image the HEK-293 cells expressing both BphPs in equimolar quantities from a single plasmid and the U87 cells expressing only DrBphP-PCM. For each measurement voxel, we reasonably assumed that the local fluence was uniform within that voxel, because the 1/e optical penetration depth for NIR light is far greater than the voxel length. Experimental results showed that the photoswitching signals from HEK-293 cells expressing both BphPs contained two decay components, while the signals from U87 cells expressing DrBphP-PCM exhibited only one decay component, regardless of local fluence. To reliably separate the two types of tumors inside deep tissue *in vivo*, we applied this labeling strategy to the liver tumors. We first injected U87 cells expressing DrBphP-PCM (0.5×10^6) into the right lobe of the mouse liver and waited 5 days to allow the injected U87 cells to grow. After the waiting period, we injected HEK-293 cells expressing both BphPs (8×10^6) into the left lobe of the liver. At two hours post injection, we then imaged the tumor-bearing mouse (n = 3). The lock-in reconstructed (LIR) image clearly resolved the two tumors (**Fig. 43a**), where BphP signals are shown in color and the background blood signals are shown in gray. The signal decays from the tumors can be modeled in the form of $g(t) = a + b \cdot e^{\left(\frac{-t}{T_1}\right)} + c \cdot e^{\left(\frac{-t}{T_2}\right)}$, where $T_1 > T_2$. The signals from HEK-293 cells were fitted with two similar coefficients $b \approx c \approx 0.5$, while the signals from U87 cells were fitted with very different coefficients $b \approx 1$, $c \approx 0$. The HEK-293 tumors contain two different photochromic proteins, exhibiting two different decay constants in the decay process (**Fig. 43b, c**); while the U87 tumors contain only one photochromic protein, exhibiting only one decay constant in the decay process (**Fig. 43b, c**). The background anatomy is shown in gray The computed coefficients, b and c, are shown in colour in **Fig. 43b** and **c**, respectively. Moreover, by analyzing the number of decay constants involved, we achieved reliable differentiation between the two tumors in deep tissue (~9.1 mm beneath skin, **Fig. 43d–f**). Coefficient k, defined as $k = \frac{max\{b,c\}}{min\{b,c\}}$, encoded image overlaid on a conventional PACT image is shown in **Fig. 43d**. Because the HEK-293 tumors contain two different photochromic proteins and U87 tumors contain only one photochromic protein, the normalized coefficient k of HEK-293 tumors is much smaller than that of U87 tumor, showing a reliable separation of the two tumors. The LIR image was used to form a binary mask, and the decay constant computation was implemented in the masked regions. As shown in **Fig. 43f,** coefficient *k*, showing the largest difference, can be used to separate the two types of tumors. Independent of the light fluence, the coefficient *k* for HEK-293 tumors is ~1, and the coefficient *k* for U87 tumors is much larger (*k* > 8).

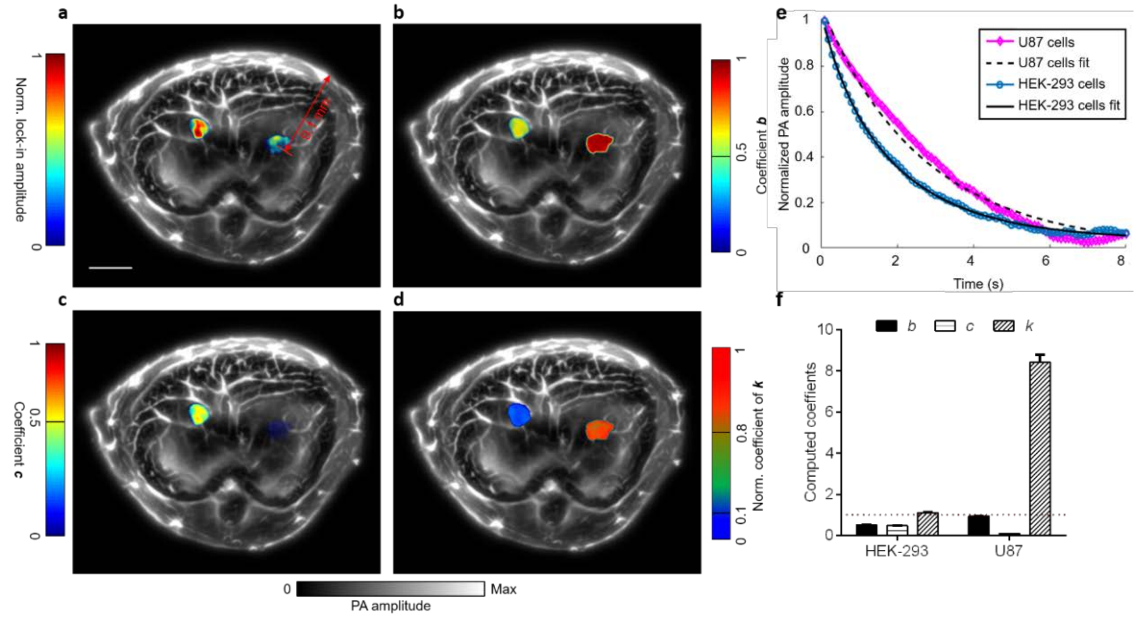
a
b
c
d
e
f
Norm. lock-in amplitude
1
0
8.1 mm
Coefficient b
0.5
Coefficient c
Norm. coefficient of k
0.8
0.1
0
PA amplitude
Max
Normalized PA amplitude
0.2
0.4
0.6
0.8
Time (s)
2
4
6
8
U87 cells
U87 cells fit
HEK-293 cells
HEK-293 cells fit
Computed coeffients
10
HEK-293
U87
b
c
k

Figure 43. *In vivo* separation of two types of cells at depths. (a) LIR image overlaid on a conventional PACT cross-sectional image, highlighting the two tumors of HEK-293 cells expressing both DrBphP-PCM and RpBphP1 (left lobe) or U87 cells expressing DrBphP-PCM (right lobe) inside the liver. (b) Coefficient *b* encoded image overlaid on a conventional PACT image. (c) Coefficient *c* encoded image overlaid on a conventional PACT cross-sectional image. (d) Normalized coefficient *k* encoded image overlaid on a conventional PACT image. (e) PA signal decays and their fits in the tumor regions. (f) The computed coefficients of *b*, *c*, and *k* from the tumor regions. Scale bar, 5 mm.

Currently, because of the absence of PA probes with NIR absorbance, whole-body molecular imaging of protein-protein interactions (PPIs) employs bioluminescent luciferases and FPs. PPI studies utilize Förster resonance energy transfer (FRET), bioluminescence energy transfer (BRET), and bimolecular fluorescence complementation (BiFC) approaches. However, relatively small changes in the FRET and BRET signals make these techniques suboptimal for use in whole mammals. BiFC is based on the tagging of two proteins of interest, each with half of an FP. Upon interaction of the proteins, the two halves of the split

FP associate with each other to form a fluorescent complex with the complemented FP, thus reporting the PPIs. Recently, we engineered several BiFC reporters from NIR FPs and demonstrated their ability to detect PPIs in mice [141, 142]. However, NIR BiFC did not provide high spatial resolution and sensitivity in imaging PPIs in deep tumors. PPIs were also imaged *in vivo* using split luciferase [143-146] and thymidine kinase [147], resulting in bioluminescence and positron emission signals, respectively. However, these reporters require injection of substrates. Moreover, the emission of the most red-shifted split-luciferase is limited to 615 nm [146], and thymidine kinase's signal provides low contrast and a non-specific background *in vivo*.

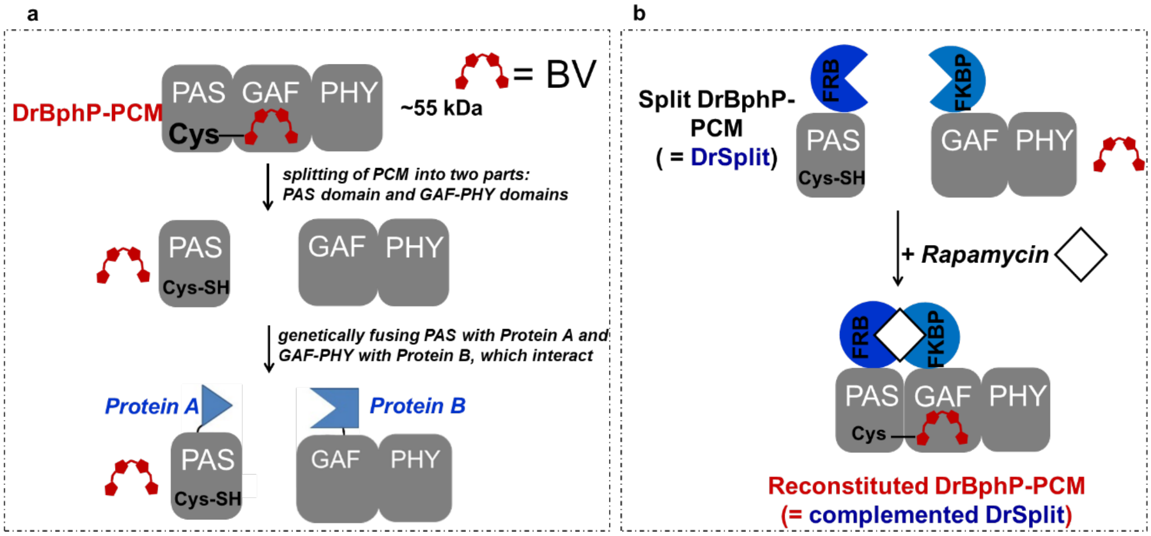
a
DrBphP-PCM
PAS GAF PHY
Cys
= BV
~55 kDa
splitting of PCM into two parts:
PAS domain and GAF-PHY domains
PAS
Cys-SH
GAF PHY
genetically fusing PAS with Protein A and
GAF-PHY with Protein B, which interact
Protein A
Protein B
PAS
Cys-SH
GAF PHY
b
Split DrBphP-PCM
(= DrSplit)
FRB
FKBP
PAS
Cys-SH
GAF PHY
+ Rapamycin
FRB
FKBP
PAS GAF PHY
Cys
Reconstituted DrBphP-PCM
(= complemented DrSplit)

Figure 44. Development of the bimolecular photoacoustic complementation (BiPC) reporter DrSplit. (a) DrBphP-PCM consists of three domains, PAS, GAF, and PHY. The biliverdin (BV) chromophore is covalently bound with conservative cysteine from the PAS domain and secured to a chromophore-binding pocket in the GAF domain. DrBphP-PCM was genetically split into two parts, the PAS domain and GAF-PHY domain, together named DrSplit. In this case, BV does not bind with any part of DrSplit. Genetically fusing one protein of interest (protein A) to one part of DrSplit and another protein of interest (protein B) to another part of DrSplit makes possible the monitoring of protein-protein interactions (PPIs) between protein A and protein B. (b) We used a model rapamycin-induced PPI between the FRB and FKBP proteins for evaluation of DrSplit. FRB was fused to the PAS domain and FKBP was fused to the GAF-PHY domains. Upon addition of rapamycin to the DrSplit, DrBphP-PCM was re-functionalized.

We engineered a split version of DrBphP-PCM, resulting in the first bimolecular photoacoustic complementation (BiPC) reporter, termed DrSplit, and applied it to study intracellular PPIs at depths. We genetically separated (split) DrBphP-PCM between the DrPAS domain and the DrGAF-PHY domains, and termed the set of these two constructs DrSplit (**Fig. 44a**). Notably, the PAS-GAF domains alone do not exhibit reversible photoswitching [148]. Complementation of the PAS domain with the GAF-PHY domain reconstitutes the complete PCM (i.e. PAS-GAF-PHY domains), thus recovering its photoswitching property. To test DrSplit complementation, we used a rapamycin-induced PPIs between the FRB and FKBP proteins [141, 142]. We genetically fused the FRB protein to the DrPAS domain, and the FKBP protein to the DrGAF-PHY domains (**Fig. 44b**).

Using DrSplit, we next longitudinally imaged PPIs in the tumors and monitored tumor metastases in the liver of mice (*n* = 4) (**Fig. 45a–d**). DrSplit-expressing MTLn3 cells (1×10^6) were first locally injected in the mouse liver. Then, rapamycin was injected through the tail vein ~40–44 h before the PA imaging. The LIR images highlighted the photoswitchable signals from the complemented DrSplit resulting from the PPIs. We detected an exponential growth of the primary tumor in the right lobe of the liver over one month (**Fig. 45a–e**). From day 15, we detected a delayed exponential growth of secondary tumors on the left lobe of the liver, resulted from metastasizing MTLn3 cells spreading to the other liver lobe (**Fig. 45b–e**). The diameter of the secondary tumor on day 15 was ~400 µm (**Fig. 45b**). The postmortem histology results confirmed the PA-measured relative locations of the tumors (**Fig. 45f**). The smallest secondary tumor had a diameter of ~400 µm, assuming the mean volume of MTLn3 cells is ~2000 μm^3, each resolution voxel contained ~3,100 MTLn3 cells. The CNR of the secondary tumor was ~9.7 in the LIR image. At a detection confidence level of 90%, we can detect PPIs with as few as ~530 cells at this depth.

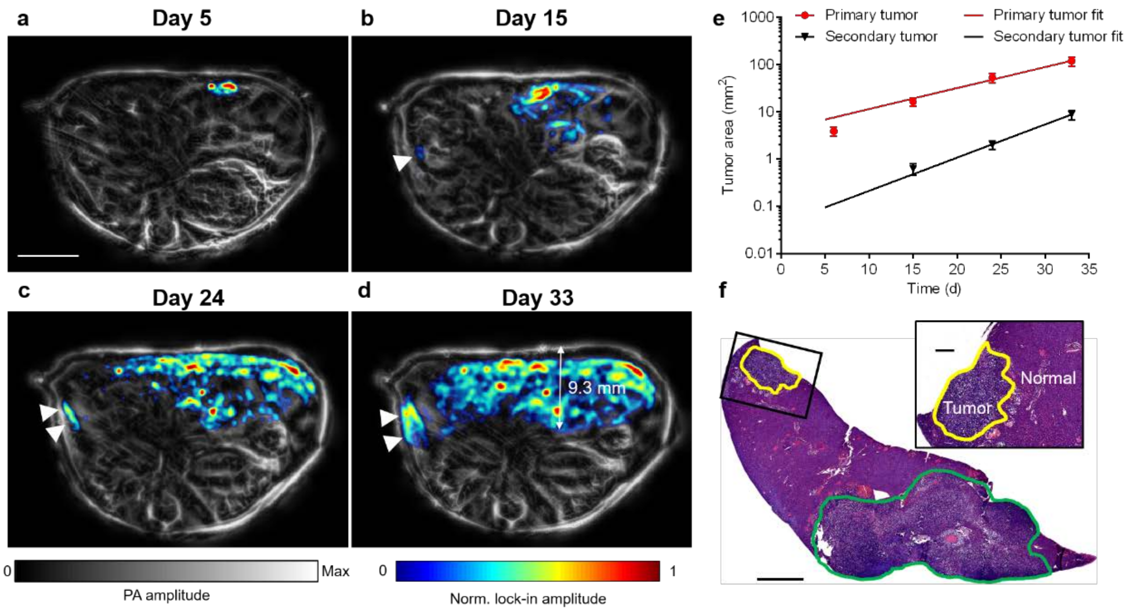
a
Day 5
b
Day 15
c
Day 24
d
Day 33
9.3 mm
0
Max
PA amplitude
0
1
Norm. lock-in amplitude
e
Primary tumor
Secondary tumor
Primary tumor fit
Secondary tumor fit
Tumor area (mm²)
1000
100
10
1
0.1
0.01
0
5
10
15
20
25
30
35
Time (d)
f
Normal
Tumor

Figure 45. Longitudinal imaging of PPIs in a tumor and monitoring of tumor metastases in a mouse liver. ~1×10^6 MTLn3 cells expressing DrSplit were injected into the mouse liver. The mice (*n* = 4) were imaged at multiple time points after tumor cell injection, and rapamycin was injected via the tail vein ~40-44 h before each PA imaging. (a-d) PA images of the mouse on (a) day 5, (b) day 15, (c) day 24, and (d) day 33 after injection of tumor cells, where the white arrows indicate the secondary tumor. LIR images are overlaid on the anatomical images. The overlay image shows the DrSplit signal in color and the background blood signal in gray. Scale bar, 5 mm. (e) Tumor growth curve, in-plane tumor area vs. time (quantified from LIR images). (f) A representative H&E histological image of a harvested left lobe of a tumorous liver, showing the tumor metastasis, where the primary tumor and secondary tumor are bordered by green and yellow lines, respectively. Scale bar, 1 mm. The close-up H&E image shows the secondary tumor, which can be clearly differentiated from normal tissue. Scale bar, 100 µm.

The NIR photochromic DrBphP-PCM probe and DrSplit PPI reporter engineered here, combined with PACT, open possibilities in basic biology and biomedical research. Both probes can noninvasively monitor individual pathways in subsets of cells in deep tissue and provide analysis of multiple pathways in a whole organ. DrSplit will allow detection of various biological processes that involve PPIs, such as wound healing, host-pathogen interactions, and organ development, and also serve as a whole-cell sensor for metabolic changes. Although BiPC of split reporters, such as DrSplit, can be irreversible, as with BiFC, it will visualize the accumulation of transient PPIs and low-affinity complexes [149, 150]. The higher detection sensitivity of BiPC can advance the monitoring of activities of drug targets, to identify potential off-target effects by detecting PPIs associated with downstream pathways. Furthermore, it will enable *in vivo* genome-wide studies of PPIs, which previously were tested with BiFC, outperforming it in depth and spatial resolution [151].

Guiding light focusing inside tissue

Recently, a rapidly developed technique—wavefront shaping— aims to overcome optical scattering and achieve tight light focus in deep tissue by creating constructive interference of the scattered photons. Wavefront shaping techniques typically require guide stars, which provide feedback for optimizing the incident optical field, to focus light inside biological tissue [152]. Several guide stars have been developed, including ultrasonic [153-156], nonlinear optical [157-161], fluorescence [162], kinetic [163, 164], photoacoustic [165-167], magnetic [168, 169], and microbubble [170] mechanisms. To enable non-invasive *in vivo* applications, such as deep tissue imaging, tissue-type specific photodynamic therapy and optogenetic control over targeted neurons, a genetically encoded guide star is desired. To our best knowledge, until now, only the fluorescence-based mechanisms, in combination with the optical phase conjugation (OPC) method, have the potential to be genetically encoded inside the biological tissue for light focusing. However, due to the incoherence property of the fluorescent photons, the demonstrated maximum focusing depth is only 0.5 mm [162]. Thus, the wavefront engineering community is still yearning for a genetically encoded guide star for deep tissue focusing. Here, we introduced a genetically-encoded photochromic guide star (GePGS)—reversibly switchable bacterial phytochrome (RSBP)—into biological tissue to provide feedback for focusing inside tissue. With the following characteristics, RSBP can serve as an ideal genetically encoded guide star for *in vivo* applications: (i) RSBP works at the near-infrared (NIR) wavelength region, where photons least attenuated by the biological tissue, and thus allowing the maximum tissue penetration; (ii) RSBP can be genetically encoded and expressed inside targeted tissue *in vivo* and their light-sensing chromophore, BV, is abundant in mammalian tissue; (iii) the absorption coefficients of RSBP can be rapidly and efficiently modulated [171] by both ballistic and scattered photons to induce local light field changes.

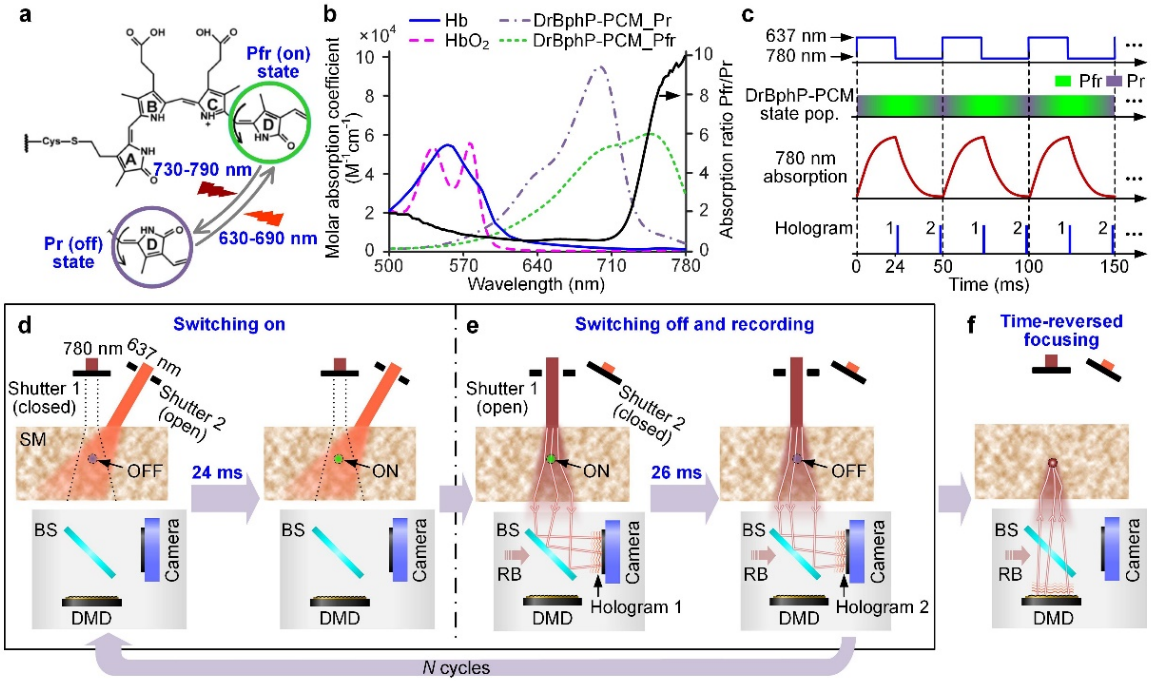

a
Pfr (on) state
Pr (off) state
730-790 nm
630-690 nm
Cys–S
b
Hb
HbO2
DrBphP-PCM_Pr
DrBphP-PCM_Pfr
Molar absorption coefficient (M⁻¹cm⁻¹)
×10⁴
Absorption ratio Pfr/Pr
Wavelength (nm)
c
637 nm
780 nm
DrBphP-PCM state pop.
Pfr
Pr
780 nm absorption
Hologram
Time (ms)
d
Switching on
780 nm
637 nm
Shutter 1 (closed)
Shutter 2 (open)
SM
OFF
24 ms
ON
BS
Camera
DMD
e
Switching off and recording
Shutter 1 (open)
Shutter 2 (closed)
26 ms
RB
Hologram 1
Hologram 2
f
Time-reversed focusing
N cycles

Figure 46. Principle of GePGS guided optical focusing inside scattering media. (a) Photoswitching of DrBphP-PCM chromophore from the Pfr state to the Pr state, and vice versa, induced by 780 nm light and 637 nm light illumination, respectively. The photoswitchings result from the out-of-plane rotation (black arrows) of the D-ring of biliverdin about the adjacent C15/16 double bond between the C and D pyrrole rings. (b) Molar absorption spectra of HbO_2, HbR, Pfr (ON) and Pr (OFF) states of DrBphP-PCM. The absorption ratio (black solid line) between the two states (Pfr/Pr) is ~10 at 780 nm. (c) Time sequence of GePGS guided DOPC system (pop., population). (d) Switching the DrBphP-PCM to ON state by a 637-nm laser with a duration of 24 ms. (e) Switching the DrBphP-PCM to OFF state by a 780-nm laser with a duration of 26 ms and capturing two holograms with an interval of 25 ms. (f) Time reversed focusing on the GePGS inside scattering media. BS beam splitter; RB reference beam.

Figure 46 depicts the principles of GePGS-guided optical focusing inside scattering media. The GePGS used here is DrBphP-PCM. The molar absorption spectra of HbO2, HbR, and the two states of DrBphP-PCM are shown in Fig. 1b. DrBphP-PCM has obvious changes in terms of spectral absorption characteristics between its two states. The absorption ratio (black-solid line in **Fig. 46b**) between its two states (Pfr/Pr) is ~10 at 780 nm, which is selected as the working wavelength for the GePGS-guided digital OPC (DOPC) system. DrBphP-PCM also possesses weak intrinsic fluorescence in the Pr state [172], which can be used to quickly verify its successful expression in tissue. **Figure 46c** shows the time sequence of the GePGS-guided digital OPC (DOPC) system and **Fig. 46d-f** show the corresponding operations for focusing light inside scattering media. The 637-nm and 780-nm light alternatingly illuminated the GePGS to switch it on and off at a frequency f_{mod} of 20 Hz for N cycles. Then the frequency of the 780-nm photons passing through the GePGS was shifted to $f_0 \pm nf_{\mathrm{mod}}$, where f_0 is the original frequency of 780-nm light, and $n = 1, 2, 3, \ldots$ (Supplementary Note 1). To obtain the wavefront of the tagged photons with frequencies of $f_0 \pm f_{\mathrm{mod}}$, a reference beam with a frequency of f_0 was introduced to interfere with the photons passing through the scattering medium (**Fig. 46e**). In each cycle, the GePGS was switched to ON state by 637-nm light illumination for 24 ms (**Fig. 46d**), and then, it was gradually switched off by 780-nm light illumination for 26 ms (**Fig. 46e**). Two holograms with a time interval of $1/(2f_{\mathrm{mod}})$, were recorded during the switching off process. Then the wavefront of the tracked photons was calculated from the recorded holograms. Finally, a digital micromirror device (DMD) was used to playback the reference beam with a conjugate wavefront to form a focus onto the GePGS, as shown in **Fig. 46f**. To minimize the impacts of the fast motions in scattering media, we averaged each hologram from N cycles.

Tissue-mimicking phantom experiments

To demonstrate GePGS-guided light focusing inside a tissue-mimicking phantom, we injected solution of purified DrBphP-PCM into a square tube, which was sandwiched by two 1.5-mm thick intralipid-gelatin phantoms, as shown in **Fig. 47a**. The concentration of GePGS is 300 μM, and the reduced scattering coefficient of the intralipid-gelatin phantoms is ~10 cm^{-1}. **Figure 47b** shows the normalized transmittance of the 780-nm light passing through the tubes with different inner dimensions during the switching off process of GePGS. The transmittance of the protein at OFF state was 70%, 81%, 89%, and 95%, when the inner dimensions of the tubes were 300 μm, 200 μm, 100 μm, and 50 μm, respectively. And **Fig. 47c** shows the time-reversed focusing on the different sizes of tubes. The PBRs are 38.2, 23.9, 10.4, and 5.3 for inner dimensions as 50 μm, 100 μm, 200 μm, and 300 μm, respectively.

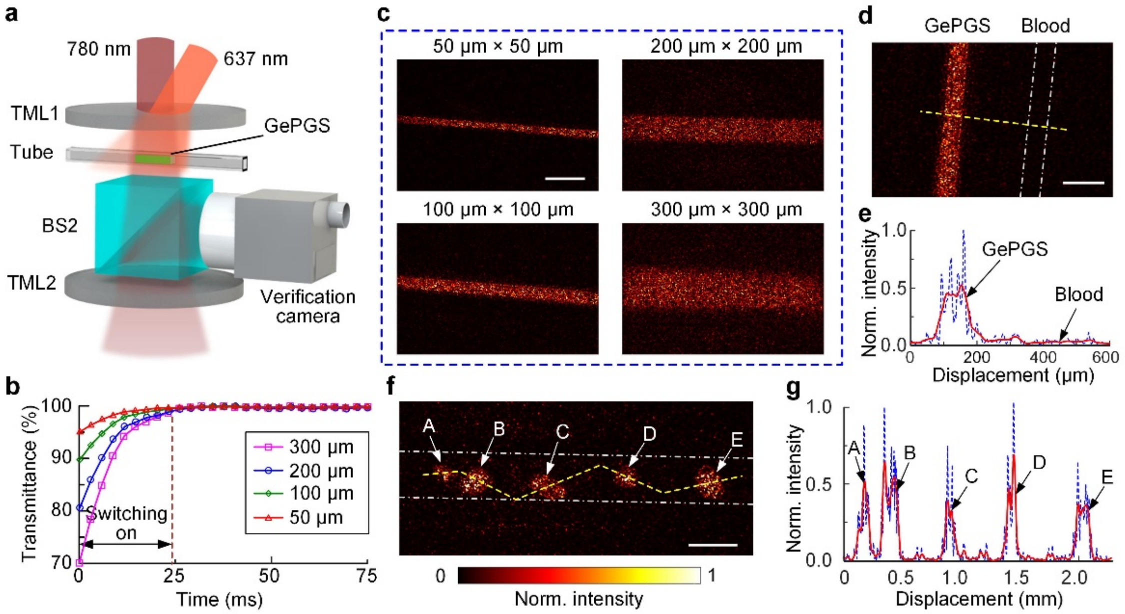

Figure 47. *In vitro* demonstration of focusing light onto GePGS inside scattering media. **(a)** Experimental setup for *in vitro* demonstration. BS, beam splitter; IP, intralipid-gelatin phantom. TML, tissue-mimicking layer. (**b)** Normalized (Norm.) transmittance of the light passing through the tubes with different sizes filled with GePGS. The length of the inner side of the tubes is 50 µm, 100 µm, 200 µm, and 300 µm, respectively. (**c)** Images of the focusing light onto GePGS injected in the tubes with different sizes. Scale bar, 300 µm. (**d)** Image shows that light is focused only onto the GePGS. Two tubes filled with GePGS and blood, respectively, are placed side by side. The white dash-dotted lines represent the inner wall of the tube filled with blood. The length of the inner side of the tubes is 100 µm. Scale bar, 200 µm. (e) Normalized intensity distribution along the yellow line in (**d)**. (**f)** Image of the focusing light onto a tube filled with U87 cells expressing GePGS. It shows that light is focused onto the GePGS expressing cells/cell clusters. The white dash-dotted lines represent the inner wall of the tube. Scale bar, 300 µm. (**g)** Normalized intensity distribution along the yellow line in (**f)**. In (e) and (g), the blue dashed line is the measured value, and the red solid line is the smoothed curve with a span of 10 points.

To verify that light only focuses on the GePGS, we sandwiched two tubes (length of inner side, 50 µm) side-by-side, filled with GePGS and bovine blood, respectively, between the two intralipid-gelatin phantoms. The time-reversed light pattern was shown in **Fig. 47d**, where the white dot-dash lines illustrate the position of the tube filled with blood. **Figure 47e** is the normalized intensity distribution along the yellow line in **Fig. 47d**. It is obviously that light was focused only on the GePGS, not on the blood. To show advantage of the developed GePGS in live mammals, we established an U87 cell line stably expressing

DrBphP-PCM, and then demonstrated the time-reversed focusing. A tube (length of inner side, 300 μm), sandwiched between the two intralipid-gelatin phantoms, was filled with GePGS expressing U87 cells. **Figure 47f** shows time-reversed light pattern, where the white dot-dash lines represent the inner wall of the tube. It is clear the time-reversed light focused on the GePGS expressing cells or cell clusters. **Figure 47g** illustrates the normalized intensity distribution along the yellow line in **Fig. 47f**. And five cells or cell clusters in the field of view with different sizes were identified.

Focusing inside mouse tumors *in vivo*

Next, we demonstrated GePGS-guide focusing inside murine tissue *in vivo*. The experimental setup is shown in **Fig. 48a**. The U87 cells expressing GePGS were injected to a mouse ear to induce tumors. We conducted the DOPC experiment on the mouse 5-day post injection. The mouse ear was illuminated by 637-nm and 780-nm light alternately with a modulation frequency of 20 Hz. The DOPC system was used to record scattered 780-nm light wavefront and played back the reference beam with an optimal wavefront to focus inside the mouse ear on the tumor. In mouse ear, both the GePGS and the fast decorrelation components, such as blood flow and respiratory motion, tagged photons in the process of OPC (**Fig. 48b**). This inevitably led to the competition between the fast decorrelation components and the GePGS in terms of light focusing. Here, the frequency lock-in technology utilized in the modulation of the GePGS significantly suppressed the impact of the fast decorrelation components. Thus, we can specifically filter out the photons tagged by the GePGS only and reject the other noise photons.

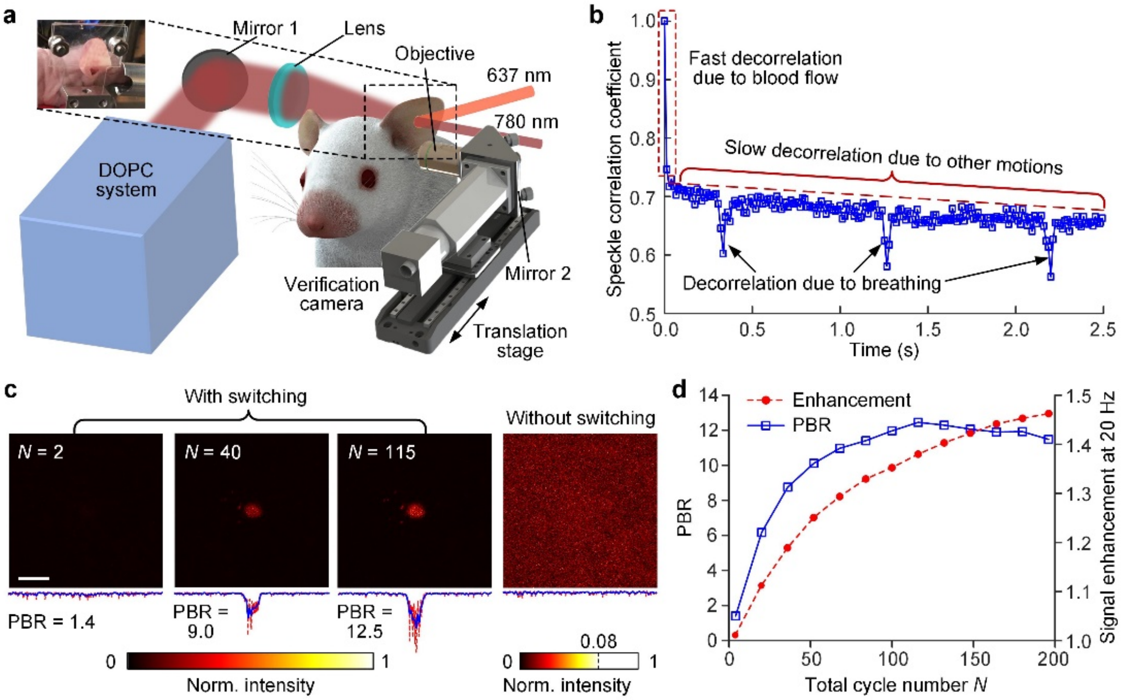

Figure 48. *In vivo* demonstration of focusing light inside tumors. (a) Schematic of the set-up for focusing light inside tumors on the mouse ear *in vivo*. A microscope is placed on a translation stage and can be moved horizontally into the light path to image the time-reversed focus. (b) The speckle correlation coefficient as a function of time for a living-mouse ear. Three speckle decorrelation characteristics were identified. (c) Normalized intensity distribution of the optical foci inside the tumor on the mouse ear. Left, with 637-nm light switching for *N*= 2, 40 and 120, respectively; Right, without 637-nm light switching. Scale bar, 100 µm. (d) Signal enhancement of tagged photons (at 20 Hz) and the PBR of time-reversed focusing as a function of total cycle number *N*.

To get a high contrast focus on the tumor inside the mouse ear, we modulated the GePGS for *N* cycles. Because the tumor was close to the right side of the mouse ear, a microscope was placed on the right side of the mouse ear to observe the photons transmitted through the ear from the left side (**Fig. 48a**). The time-reversed foci, with different *N*, on the tumor were captured by the microscope (**Fig. 48c**, left three panels). In the control experiment, where the light modulation was off, no light focus was observed (**Fig. 48c**, right panel). The detected signals of tagged photons (at 20 Hz) increase with increasing of *N* (**Fig. 48d**, red-circle-dashed curve). The PBR of the time-reversed focus also increases with *N* but reaches the maximum when averaging over 115 cycles, and starts to decrease if averaged more (**Fig. 48d**, blue-squared-solid curve). This is because the impact of slow decorrelation (**Fig. 48b**) on PBR becomes obvious as the overall time of DOPC increases. With the capability of selective delivery of light on to the specific tissue types, such as tumors, the GePGS guided wavefront shaping advances light-driven therapy of targeted tumors at depths *in vivo*.

Focusing in the live mouse brain tissue

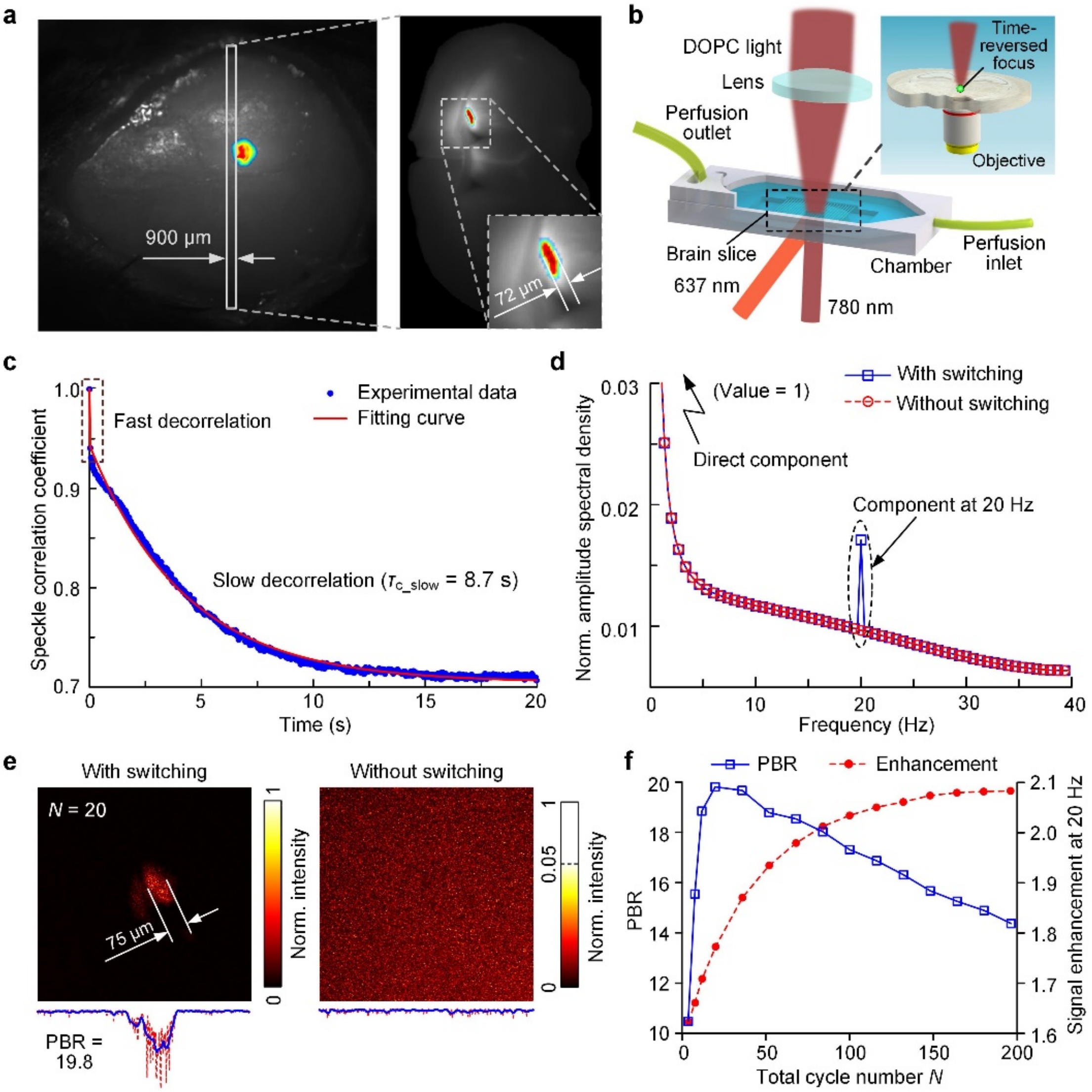

Figure 49. Demonstration of focusing light inside live brain slices. (a) Fluorescence images of the transduced mouse brain *in vivo* and a live brain slice showing the brain tissue expressing GePGS. The differential fluorescence signals between ON and OFF states highlight the brain tissue express RSBPs, which are shown in color; and the background signals are shown in gray. Excitation wavelength, 630 nm. (b) Schematic of the set-up for

focusing light inside brain slices. (c) Speckle correlation coefficient as a function of time for a live brain slice. Two speckle decorrelation characteristics are identified. (d) Normalized amplitude spectral density of the detected photons, where a peak is observed at 20 Hz with light switching. (e) Normalized intensity distribution of the optical foci inside the brain slices. Left, with 637-nm light switching for *N*= 20; Right, without 637-nm light switching. (f) Signal enhancement of tagged photons (at 20 Hz) and the PBR of time-reversed focusing as a function of total cycle number *N*.

Due to the strong optical scattering nature of the brain, current light delivery for optogenetic manipulations and optical readouts still primarily employs invasive optical fiber implants to reach targets in the deep brain. We have transduced the mouse brain with AAVs *in vivo*. Fluorescence images showed a successful expression of DrBphP-PCM in the brain (**Fig. 49a**, left panel), although the imaging resolution was not very high due to the strong optical scattering of brain tissue. To demonstrate light focusing inside the live brain tissue, a 900-μm thick brain slice was harvested. On this brain slice, the DrBphP-PCM was expressed close to the bottom side (**Fig. 49a**, right panel view from the bottom side of the brain slice). The DOPC experimental setup is shown in **Fig. 49b**. In the brain slice, the principal decorrelation is slow decorrelation with a decorrelation time of 8.7 s (**Fig. 49c**). After modulating the GePGS for 20 cycles, the tagged photon signals at 20 Hz have been increased by a factor of ~2 (**Fig. 49d**). An objective was placed on the bottom side of the brain slice to observe the light focus (**Fig. 49b**, inset). With 20 cycles of modulation, we observed a time-reversed focus on the brain slice with a PBR of 19.8 (Fig. 5e, left panel), which matches well with the fluorescence image (**Fig. 49a**, right panel). In the control experiment, without light modulation, no light focus was observed (**Fig. 49e**, right panel). The tagged photon signals increased with increasing of *N* (**Fig. 49f**, red-circle-dashed curve). While the PBR of the time-reversed focus also increased with *N* but reached the maximum after averaging over 20 cycles, and then started to decrease if averaging more (**Fig. 49e**, blue-squared-solid curve), because the dominated slow decorrelation caused mismatch between the recorded wavefront and the optimal wavefront.

Discussion

We have introduced an RSBP, such as DrBphP-PCM, as the GePGS and experimentally demonstrated the time-reversed focusing light inside scattering media. The RSBP, working in the NIR window, maximize the optical penetration in biological tissue. The optical absorption of the RSBP is controllable upon light illumination. Moreover, the RSBP can be genetically encoded and expressed inside the tissue through either exogenous cell translation or native expression via virus infection, which makes them crucial noninvasive imaging tool. Taking advantages of both the tissue-specific expression and effective light modulation of the GePGS, we can effectively focus light onto targeted tissue, such as tumors, at depth, which promises advance photodynamic therapy (PDT). Conventionally, PDT employs NIR light to activate the photosensitizers for the tumor destruction [173-175]. However, the strong tissue scattering significantly reduces the light delivery efficiency and limits the penetration of PDT. Now the GePGS guided light focusing overcomes the aforementioned limitations and facilitates PDT with effective photon utilization at previously unreachable tissue depths.

Noninvasively focusing light deep inside the living tissue promises many biomedical studies, especially for neuroscience, where light is routinely used for both monitoring neural activity with genetically encoded voltage or calcium indicators [176, 177] and controlling neural activity via optogenetic actuators [178, 179]. Although advanced optical imaging techniques, such as multiphoton microscopy, adaptive optical microscopy and photoacoustic tomography have significantly extended the depths of optical access *in vivo* [8, 23, 180-183], noninvasive light focusing in the diffusive regime in living brain tissue remains challenging. We successfully expressed RSBP in neurons using viral transduction. After multiple-cycle modulation of GePGS, scattering photons have been effectively tagged and a tight optical focus has been created inside the brain slice. Importantly, RSBP-based GePGS itself can be the optogenetic actuators [184, 185]. Thus, the GePGS-guided photons can automatically and specifically focus on a neural activity actuator, without blind activation of background neurons, which should significantly increase the light delivery efficiency and the specificity of noninvasive deep-brain manipulations.

The GePGS has been demonstrated based on a DOPC system, the guide star itself and the frequency modulation method are also compatible with the feedback-based wavefront shaping method. The amplitude and phase contribution of each optical field component for focusing inside scattering media can be optimized based on the feedback alternating signals from the GePGS at a specific frequency. The physical limit of the photoswitching time for DrBphP-PCM, the GePGS used in this manuscript, is 1 ms [171]. which allows to further improve our DOPC system for a faster response to fight against tissue optical decorrelation and thus permits even deeper light focusing. Moreover, the combination of GePGS guided focusing and PAT, which provides high spatial resolution imaging in deep tissue based on optical contrast, is another appealing direction to explore. PAT can directly visualize the light focus in deep tissue and also image the focusing light induced biological activities, such as neuron firing and metabolic responses of tumors.

Chapter 5

CONCLUSIONS AND OUTLOOK

Overall, multi-contrast PACT is a powerful tool for imaging the small animal whole body and whole brain functions, complementary to other small-animal imaging modalities in its contrast mechanism, spatiotemporal resolution, speed, and penetration. The increasing applications of PACT in preclinical research and clinical translations provide strong momentum for PACT's development. The exciting research and translational capabilities of PACT come with several technical challenges, but none are beyond reach. (1) For imaging neuronal activities in the deep brain, novel voltage-/calcium-sensitive indicators of action potentials need to be found or engineered. Most of the currently available voltage/calcium indicators operate in the visible wavelength range, which limits the tissue penetration [177, 186]. Strong optical absorption in the red and NIR spectral ranges is preferable. In addition, the other characteristics of the indicators, such as voltage/calcium sensing mechanism, life time, response time, etc., need to be tailored for optimized PA contrast. Nonfluorescent NIR bacteriophytochromes could be candidates to report action potentials for PA imaging. (2) The major barrier of translating PAT to adult human brain imaging is the skull. The adult human skull (~5–11 mm thick) greatly attenuates the excitation light and the emitted PA waves, and strongly distorts the PA waveforms, resulting in low image quality. A potential solution is to combine PACT with X-ray CT or MRI, which can provide accurate skull information to correct for the signal distortion. (3) NIR light is still attenuated strongly by the skull, which hinders imaging the whole human brain using PACT. As another source of non-ionizing radiation, microwaves can also heat tissue by producing molecular rotations and torsions [187, 188]. The human skull is more transparent to microwaves than to photons. Thermoacoustic tomography (TAT) [189-192], utilizing microwave pulses instead of laser pulses, can potentially extend the penetration depth beyond 10 cm and enable deep human brain imaging.

BIBLIOGRAPHY

[1] A. G. Bell, "ART. XXXIV.--On the Production and Reproduction of Sound by Light," American Journal of Science (1880-1910), 20(118), 305 (1880).

[2] M. Baker, "Whole-animal imaging: The whole picture," Nature, 463(7283), 977-980 (2010).

[3] L. H. V. Wang, and S. Hu, "Photoacoustic tomography: in vivo imaging from organelles to organs," Science, 335(6075), 1458-1462 (2012).

[4] L. Li, L. Zhu, C. Ma *et al.*, "Single-impulse panoramic photoacoustic computed tomography of small-animal whole-body dynamics at high spatiotemporal resolution," Nature Biomedical Engineering, 1, 0071 (2017).

[5] M. Zhou, L. Li, J. Yao *et al.*, [Nanoparticles for Photoacoustic Imaging of Vasculature] Springer, Cham, (2017).

[6] L. Li, J. Yao, and L. V. Wang, [Photoacoustic tomography enhanced by nanoparticles] John Wiley & Sons, Inc., (2016).

[7] W. Liu, Y. Zhou, M. Wang *et al.*, "Correcting the limited view in optical-resolution photoacoustic microscopy," Journal of biophotonics, 11(2), e201700196 (2018).

[8] H.-C. Hsu, L. Li, J. Yao *et al.*, "Dual-axis illumination for virtually augmenting the detection view of optical-resolution photoacoustic microscopy," Journal of biomedical optics, 23(7), 076001 (2018).

[9] L. Zhu, L. Li, L. Gao *et al.*, "Multiview optical resolution photoacoustic microscopy," Optica, 1(4), 217-222 (2014).

[10] L. Zhu, L. Gao, L. Li *et al.*, "Cross-optical-beam nonlinear photoacoustic microscopy." 8943, 89433H.

[11] Y. S. Zhang, J. Yao, C. Zhang *et al.*, "Optical-Resolution Photoacoustic Microscopy for Volumetric and Spectral Analysis of Histological and Immunochemical Samples," Angewandte Chemie International Edition, 53(31), 8099-8103 (2014).

[12] L. Li, C. Yeh, S. Hu *et al.*, "Fully motorized optical-resolution photoacoustic microscopy," Optics letters, 39(7), 2117-2120 (2014).

[13] L. Li, C. Yeh, S. Hu *et al.*, "Combined optical and mechanical scanning in optical-resolution photoacoustic microscopy." 8943, 89435X.

[14] L. V. Wang, and J. Yao, "A practical guide to photoacoustic tomography in the life sciences," Nature Methods, 13, 627 (2016).

[15] X. Wang, Y. Pang, G. Ku *et al.*, "Noninvasive laser-induced photoacoustic tomography for structural and functional in vivo imaging of the brain," Nature biotechnology, 21(7), 803 (2003).

[16] G. Li, L. Li, L. Zhu *et al.*, "Multiview Hilbert transformation for full-view photoacoustic computed tomography using a linear array," Journal of biomedical optics, 20(6), 066010 (2015).

[17] T. T. Wong, Y. Zhou, A. Garcia-Uribe *et al.*, "Use of a single xenon flash lamp for photoacoustic computed tomography of multiple-centimeter-thick biological tissue ex vivo and a whole mouse body in vivo," Journal of biomedical optics, 22(4), 041003 (2016).

[18] Y. Qu, L. Li, Y. Shen *et al.*, “Dichroism-sensitive photoacoustic computed tomography,” Optica, 5(4), 495-501 (2018).

[19] C. Yeh, L. Li, L. Zhu *et al.*, “Dry coupling for whole-body small-animal photoacoustic computed tomography,” Journal of biomedical optics, 22(4), 041017 (2017).

[20] T. Imai, J. Shi, T. T. Wong *et al.*, “High-throughput ultraviolet photoacoustic microscopy with multifocal excitation,” Journal of biomedical optics, 23(3), 036007 (2018).

[21] G. Li, J. Xia, L. Li *et al.*, "Isotropic-resolution linear-array-based photoacoustic computed tomography through inverse Radon transform." 9323, 93230I.

[22] H. Ke, C. Liu, L. V. Wang *et al.*, “Performance characterization of an integrated ultrasound, photoacoustic, and thermoacoustic imaging system,” Journal of biomedical optics, 17(5), 056010 (2012).

[23] P. Zhang, L. Li, L. Lin *et al.*, “High-resolution deep functional imaging of the whole mouse brain by photoacoustic computed tomography in vivo,” Journal of biophotonics, 11(1), e201700024 (2018).

[24] L. Li, J. Xia, G. Li *et al.*, "Label-free photoacoustic tomography of whole mouse brain structures <i>ex vivo</i>." 3, 8.

[25] P. Zhang, L. Li, L. Lin *et al.*, “In vivo superresolution photoacoustic computed tomography by localization of single dyed droplets,” Light: Science & Applications, 8(1), 36 (2019).

[26] J. Yao, A. A. Kaberniuk, L. Li *et al.*, “Multiscale photoacoustic tomography using reversibly switchable bacterial phytochrome as a near-infrared photochromic probe,” Nature Methods, 13(1), 67-+ (2016).

[27] L. Li, A. A. Shemetov, M. Baloban *et al.*, “Small near-infrared photochromic protein for photoacoustic multi-contrast imaging and detection of protein interactions in vivo,” Nature Communications, 9(1), 2734 (2018).

[28] P. Zanzonico, [Noninvasive Imaging for Supporting Basic Research] Springer Berlin Heidelberg, Berlin, Heidelberg(2011).

[29] V. Ntziachristos, “Going deeper than microscopy: the optical imaging frontier in biology,” Nature Methods, 7(8), 603-614 (2010).

[30] X. Jun, and L. V. Wang, “Small-Animal Whole-Body Photoacoustic Tomography: A Review,” IEEE Transactions on Biomedical Engineering, 61(5), 1380-9 (2014).

[31] D. Wu, and J. Zhang, “In vivo mapping of macroscopic neuronal projections in the mouse hippocampus using high-resolution diffusion MRI,” NeuroImage, 125, 84-93 (2016).

[32] O. I. Alomair, I. M. Brereton, M. T. Smith *et al.*, “In vivo high angular resolution diffusion-weighted imaging of mouse brain at 16.4 Tesla,” PloS one, 10(6), e0130133 (2015).

[33] S. J. Schambach, S. Bag, L. Schilling *et al.*, “Application of micro-CT in small animal imaging,” Methods, 50(1), 2-13 (2010).

[34] D. J. Brenner, and E. J. Hall, “Computed Tomography — An Increasing Source of Radiation Exposure,” New England Journal of Medicine, 357(22), 2277-2284 (2007).

[35] A. Greco, M. Mancini, S. Gargiulo *et al.*, “Ultrasound Biomicroscopy in Small Animal Research: Applications in Molecular and Preclinical Imaging,” Journal of Biomedicine and Biotechnology, 2012, 14 (2012).

[36] T. Kim, R. Zhou, M. Mir *et al.*, “White-light diffraction tomography of unlabelled live cells,” Nat Photon, 8(3), 256-263 (2014).

[37] N. G. Horton, K. Wang, D. Kobat *et al.*, “In vivo three-photon microscopy of subcortical structures within an intact mouse brain,” Nat Photon, 7(3), 205-209 (2013).

[38] F. Zhang, L.-P. Wang, M. Brauner *et al.*, “Multimodal fast optical interrogation of neural circuitry,” Nature, 446(7136), 633-639 (2007).

[39] C. Darne, Y. Lu, and E. M. Sevick-Muraca, “Small animal fluorescence and bioluminescence tomography: a review of approaches, algorithms and technology update,” Physics in Medicine and Biology, 59(1), R1-R64 (2014).

[40] D. Razansky, M. Distel, C. Vinegoni *et al.*, “Multispectral opto-acoustic tomography of deep-seated fluorescent proteins in vivo,” Nature Photonics, 3(7), 412-417 (2009).

[41] J. Yao, L. Wang, J.-M. Yang *et al.*, “High-speed label-free functional photoacoustic microscopy of mouse brain in action,” Nature Methods, 12(5), 407-+ (2015).

[42] A. P. Jathoul, J. Laufer, O. Ogunlade *et al.*, “Deep in vivo photoacoustic imaging of mammalian tissues using a tyrosinase-based genetic reporter,” Nature Photonics, 9(4), 239-246 (2015).

[43] H.-P. Brecht, R. Su, M. Fronheiser *et al.*, “Whole-body three-dimensional optoacoustic tomography system for small animals,” Journal of Biomedical Optics, 14(6), 064007-064007-8 (2009).

[44] A. Taruttis, S. Morscher, N. C. Burton *et al.*, “Fast Multispectral Optoacoustic Tomography (MSOT) for Dynamic Imaging of Pharmacokinetics and Biodistribution in Multiple Organs,” PLOS ONE, 7(1), e30491 (2012).

[45] E. Merčep, N. C. Burton, J. Claussen *et al.*, “Whole-body live mouse imaging by hybrid reflection-mode ultrasound and optoacoustic tomography,” Optics Letters, 40(20), 4643-4646 (2015).

[46] D. Razansky, A. Buehler, and V. Ntziachristos, “Volumetric real-time multispectral optoacoustic tomography of biomarkers,” Nat. Protocols, 6(8), 1121-1129 (2011).

[47] X. Luis Dean-Ben, and D. Razansky, “Adding fifth dimension to optoacoustic imaging: volumetric time-resolved spectrally enriched tomography,” Light Sci Appl, 3, e137 (2014).

[48] J. Tang, J. E. Coleman, X. Dai *et al.*, “Wearable 3-D Photoacoustic Tomography for Functional Brain Imaging in Behaving Rats,” Scientific reports, 6, (2016).

[49] X. Yuan, and L. V. Wang, “Effects of acoustic heterogeneity in breast thermoacoustic tomography,” Ultrasonics, Ferroelectrics, and Frequency Control, IEEE Transactions on, 50(9), 1134-1146 (2003).

[50] B. E. Treeby, and B. T. Cox, “k-Wave: MATLAB toolbox for the simulation and reconstruction of photoacoustic wave fields,” J Biomed Opt, 15(2), 021314 (2010).

[51] E. W. Stein, K. Maslov, and L. V. Wang, “Noninvasive, in vivo imaging of blood-oxygenation dynamics within the mouse brain using photoacoustic microscopy,” Journal of Biomedical Optics, 14(2), 020502-020502-3 (2009).

[52] T. P. Matthews, J. Poudel, L. Li *et al.*, “Parameterized Joint Reconstruction of the Initial Pressure and Sound Speed Distributions for Photoacoustic Computed Tomography,” SIAM Journal on Imaging Sciences, 11(2), 1560-1588 (2018).

[53] J. Poudel, T. P. Matthews, L. Li *et al.*, “Mitigation of artifacts due to isolated acoustic heterogeneities in photoacoustic computed tomography using a variable data truncation-based reconstruction method,” Journal of biomedical optics, 22(4), 041018 (2017).

[54] T. P. Matthews, L. Li, L. V. Wang *et al.*, "Compensation for air voids in photoacoustic computed tomography image reconstruction." 9708, 970841.

[55] J. Xia, C. Huang, K. Maslov *et al.*, “Enhancement of photoacoustic tomography by ultrasonic computed tomography based on optical excitation of elements of a full-ring transducer array,” Optics Letters, 38(16), 3140-3143 (2013).

[56] J. N. Cohn, S. Finkelstein, G. McVeigh *et al.*, “Noninvasive pulse-wave analysis for the early detection of vascular-disease,” Hypertension, 26(3), 503-508 (1995).

[57] E. Kis, O. Cseprekal, Z. Horvath *et al.*, “Pulse wave velocity in end-stage renal disease: Influence of age and body dimensions,” Pediatric Research, 63(1), 95-98 (2008).

[58] E. Jonckers, J. Van Audekerke, G. De Visscher *et al.*, “Functional Connectivity fMRI of the Rodent Brain: Comparison of Functional Connectivity Networks in Rat and Mouse,” PLOS ONE, 6(4), e18876 (2011).

[59] B.-F. Osmanski, S. Pezet, A. Ricobaraza *et al.*, “Functional ultrasound imaging of intrinsic connectivity in the living rat brain with high spatiotemporal resolution,” Nature communications, 5, (2014).

[60] X. L. Dean-Ben, G. Sela, A. Lauri *et al.*, “Functional optoacoustic neuro-tomography for scalable whole-brain monitoring of calcium indicators,” Light Sci Appl., 5, e16201 (2016).

[61] S. Gottschalk, T. F. Fehm, X. L. Deán-Ben *et al.*, “Noninvasive Real-Time Visualization of Multiple Cerebral Hemodynamic Parameters in Whole Mouse Brains Using Five-Dimensional Optoacoustic Tomography,” Journal of Cerebral Blood Flow & Metabolism, 35(4), 531-535 (2015).

[62] Y. Chen, A. D. Aguirre, L. Ruvinskaya *et al.*, “Optical coherence tomography (OCT) reveals depth-resolved dynamics during functional brain activation,” Journal of neuroscience methods, 178(1), 162-173 (2009).

[63] C. Tischbirek, A. Birkner, H. Jia *et al.*, “Deep two-photon brain imaging with a red-shifted fluorometric Ca2+ indicator,” Proceedings of the National Academy of Sciences, 112(36), 11377-11382 (2015).

[64] M. Xu, and L. V. Wang, “Universal back-projection algorithm for photoacoustic computed tomography,” Physical Review E, 71(1), 016706 (2005).

[65] Y. Xu, L. V. Wang, G. Ambartsoumian *et al.*, “Reconstructions in limited-view thermoacoustic tomography,” Medical physics, 31(4), 724-733 (2004).

[66] B. Biswal, F. Zerrin Yetkin, V. M. Haughton *et al.*, “Functional connectivity in the motor cortex of resting human brain using echo-planar MRI,” Magnetic resonance in medicine, 34(4), 537-541 (1995).

[67] M. D. Fox, and M. E. Raichle, “Spontaneous fluctuations in brain activity observed with functional magnetic resonance imaging,” Nature reviews neuroscience, 8(9), 700 (2007).

[68] M. D. Greicius, B. H. Flores, V. Menon *et al.*, “Resting-state functional connectivity in major depression: abnormally increased contributions from subgenual cingulate cortex and thalamus,” Biological psychiatry, 62(5), 429-437 (2007).

[69] R. L. Buckner, J. Sepulcre, T. Talukdar *et al.*, “Cortical hubs revealed by intrinsic functional connectivity: mapping, assessment of stability, and relation to Alzheimer's disease,” Journal of neuroscience, 29(6), 1860-1873 (2009).

[70] S. M. Lawrie, C. Buechel, H. C. Whalley *et al.*, “Reduced frontotemporal functional connectivity in schizophrenia associated with auditory hallucinations,” Biological Psychiatry, 51(12), 1008-1011 (2002).

[71] J. Grandjean, A. Schroeter, I. Batata *et al.*, “Optimization of anesthesia protocol for resting-state fMRI in mice based on differential effects of anesthetics on functional connectivity patterns,” NeuroImage, 102, 838-847 (2014).

[72] M. D. Fox, D. Zhang, A. Z. Snyder *et al.*, “The global signal and observed anticorrelated resting state brain networks,” Journal of neurophysiology, 101(6), 3270-3283 (2009).

[73] M. Nasiriavanaki, J. Xia, H. Wan *et al.*, “High-resolution photoacoustic tomography of resting-state functional connectivity in the mouse brain,” Proceedings of the National Academy of Sciences, 111(1), 21-26 (2014).

[74] E. Macé, G. Montaldo, I. Cohen *et al.*, “Functional ultrasound imaging of the brain,” Nature methods, 8(8), 662 (2011).

[75] J. Yao, A. A. Kaberniuk, L. Li *et al.*, “Multiscale photoacoustic tomography using reversibly switchable bacterial phytochrome as a near-infrared photochromic probe,” Nat Meth, 13(1), 67-73 (2016).

[76] A. P. Jathoul, J. Laufer, O. Ogunlade *et al.*, “Deep in vivo photoacoustic imaging of mammalian tissues using a tyrosinase-based genetic reporter,” Nature Photonics, (2015).

[77] H. F. Zhang, K. Maslov, G. Stoica *et al.*, “Functional photoacoustic microscopy for high-resolution and noninvasive in vivo imaging,” Nat Biotechnol., 24(7), 848-851 (2006).

[78] S. Tzoumas, A. Nunes, I. Olefir *et al.*, “Eigenspectra optoacoustic tomography achieves quantitative blood oxygenation imaging deep in tissues,” Nature communications, 7, ncomms12121 (2016).

[79] J. Xia, A. Danielli, Y. Liu *et al.*, “Calibration-free quantification of absolute oxygen saturation based on the dynamics of photoacoustic signals,” Optics Letters, 38(15), 2800-2803 (2013).

[80] M. E. Raichle, “Behind the scenes of functional brain imaging: A historical and physiological perspective,” Proceedings of the National Academy of Sciences of the United States of America, 95(3), 765-772 (1998).

[81] S. Ogawa, T.-M. Lee, A. R. Kay *et al.*, “Brain magnetic resonance imaging with contrast dependent on blood oxygenation,” Proceedings of the National Academy of Sciences, 87(24), 9868-9872 (1990).

[82] M. B. V. Roberts, [Control of respiratory gases] Thomas Nelson and Sons Ltd, Delta Place, 27 Bath Road, Cheltenham, CL53 7th, United Kingdom, 16 (1986).

[83] J. T. Joiner, [Diving Physiology] Best Publishing Company, 3 (2001).

[84] A. Karimova, and J. D. Pinsky, "The endothelial response to oxygen deprivation: biology and clinical implications," Intensive Care Medicine, 27(1), 19-31 (2001).

[85] C. A. Piantadosi, [Air as good as we deserve] Oxford University Press, 198 Madison Avenue, New York, New York, 10016(2003).

[86] G. S. Scott Brady, R. Wayne Albers, Donald Price, [Basic Neurochemistry: Molecular, Cellular and Medical Aspects] Elsevier Academic Press, Burlington, MA 01803, USA(2006).

[87] Y. Ma, D. Smith, P. R. Hof *et al.*, "In vivo 3D digital atlas database of the adult C57BL/6J mouse brain by magnetic resonance microscopy," Frontiers in Neuroanatomy, 2, 10 (2008).

[88] J. C. Sutherland, and K. P. Griffin, "ABSORPTION-SPECTRUM OF DNA FOR WAVELENGTHS GREATER THAN 300-NM," Radiation Research, 86(3), 399-410 (1981).

[89] W. L. Lin, R. Venkatesan, K. Gurleyik *et al.*, "An absolute measurement of brain water content using magnetic resonance imaging in two focal cerebral ischemic rat models," Journal of Cerebral Blood Flow and Metabolism, 20(1), 37-44 (2000).

[90] C. Zhang, Y. S. Zhang, D. K. Yao *et al.*, "Label-free photoacoustic microscopy of cytochromes," J Biomed Opt, 18(2), 20504 (2013).

[91] M. Picard, and B. S. McEwen, "Mitochondria impact brain function and cognition," Proceedings of the National Academy of Sciences of the United States of America, 111(1), 7-8 (2014).

[92] A. V. Brusnichkin, D. A. Nedosekin, E. I. Galanzha *et al.*, "Ultrasensitive label-free photothermal imaging, spectral identification, and quantification of cytochrome c in mitochondria, live cells, and solutions," Journal of Biophotonics, 3(12), 791-806 (2010).

[93] M. Tanaka, K. Yamaguchi, T. Tatsukawa *et al.*, "Connexin43 and bergmann glial gap junctions in cerebellar function," Frontiers in neuroscience, 2(2), 225-33 (2008).

[94] S. Kim, S. Pickup, O. Hsu *et al.*, "Enhanced delineation of white matter structures of the fixed mouse brain using Gd-DTPA in microscopic MRI," Nmr in Biomedicine, 22(3), 303-309 (2009).

[95] J. Hui, R. Li, E. H. Phillips *et al.*, "Bond-selective photoacoustic imaging by converting molecular vibration into acoustic waves," Photoacoustics, 4(1), 11-21 (2016).

[96] G. Miura, "Cancer tumor imaging: Catch me if you can," Nat Chem Biol, 10(7), 485-485 (2014).

[97] S. Nagrath, L. V. Sequist, S. Maheswaran *et al.*, "Isolation of rare circulating tumour cells in cancer patients by microchip technology," Nature, 450(7173), 1235-1239 (2007).

[98] Y. Kienast, L. von Baumgarten, M. Fuhrmann *et al.*, "Real-time imaging reveals the single steps of brain metastasis formation," Nature Medicine, 16(1), 116-U157 (2010).

[99] R. L. Siegel, K. D. Miller, and A. Jemal, “Cancer statistics, 2016,” CA: A Cancer Journal for Clinicians, 66(1), 7-30 (2016).
[100] V. J. Srinivasan, S. Sakadžić, I. Gorczynska *et al.*, “Quantitative cerebral blood flow with Optical Coherence Tomography,” Optics Express, 18(3), 2477-2494 (2010).
[101] S. B. Cox, T. A. Woolsey, and C. M. Rovainen, “Localized dynamic changes in cortical blood flow with whisker stimulation corresponds to matched vascular and neuronal architecture of rat barrels,” Journal of Cerebral Blood Flow & Metabolism, 13(6), 899-913 (1993).
[102] L. V. Wang, and S. Hu, “Photoacoustic tomography: In vivo imaging from organelles to organs,” Science, 335(6075), 1458-1462 (2012).
[103] L. V. Wang, “Multiscale photoacoustic microscopy and computed tomography,” Nature Photonics, 3, 503 (2009).
[104] E. Betzig, G. H. Patterson, R. Sougrat *et al.*, “Imaging Intracellular Fluorescent Proteins at Nanometer Resolution,” Science, 313(5793), 1642-1645 (2006).
[105] M. J. Rust, M. Bates, and X. Zhuang, “Sub-diffraction-limit imaging by stochastic optical reconstruction microscopy (STORM),” Nature Methods, 3, 793 (2006).
[106] T. Chaigne, J. Gateau, M. Allain *et al.*, “Super-resolution photoacoustic fluctuation imaging with multiple speckle illumination,” Optica, 3(1), 54-57 (2016).
[107] T. Chaigne, B. Arnal, S. Vilov *et al.*, “Super-resolution photoacoustic imaging via flow-induced absorption fluctuations,” Optica, 4(11), 1397-1404 (2017).
[108] S. Vilov, B. Arnal, and E. Bossy, “Overcoming the acoustic diffraction limit in photoacoustic imaging by the localization of flowing absorbers,” Optics Letters, 42(21), 4379-4382 (2017).
[109] X. L. Dean-Ben, and D. Razansky, “Localization optoacoustic tomography,” Light: Science & Applications, 7, 18004 (2018).
[110] S. Prahl, [Optical Absorption of Hemoglobin].
[111] B. Ning, N. Sun, R. Cao *et al.*, “Ultrasound-aided Multi-parametric Photoacoustic Microscopy of the Mouse Brain,” Scientific Reports, 5, 18775 (2015).
[112] Y. Li, U. Baran, and R. K. Wang, “Application of Thinned-Skull Cranial Window to Mouse Cerebral Blood Flow Imaging Using Optical Microangiography,” PLOS ONE, 9(11), e113658 (2014).
[113] R. E. Thompson, D. R. Larson, and W. W. Webb, “Precise Nanometer Localization Analysis for Individual Fluorescent Probes,” Biophysical Journal, 82(5), 2775-2783 (2002).
[114] L. Yobas, S. Martens, W.-L. Ong *et al.*, “High-performance flow-focusing geometry for spontaneous generation of monodispersed droplets,” Lab on a Chip, 6(8), 1073-1079 (2006).
[115] A. de la Zerda, S. Bodapati, R. Teed *et al.*, “Family of Enhanced Photoacoustic Imaging Agents for High-Sensitivity and Multiplexing Studies in Living Mice,” Acs Nano, 6(6), 4694-4701 (2012).
[116] M. Eghtedari, A. Oraevsky, J. A. Copland *et al.*, “High sensitivity of in vivo detection of gold nanorods using a laser optoacoustic imaging system,” Nano Letters, 7(7), 1914-1918 (2007).
[117] W. Guo, C. Guo, N. Zheng *et al.*, “CsxWO3 Nanorods Coated with Polyelectrolyte Multilayers as a Multifunctional Nanomaterial for Bimodal Imaging-Guided

Photothermal/Photodynamic Cancer Treatment," Adv Mater, 29(4), 1604157-n/a (2017).

[118] T. Ji, V. G. Lirtsman, Y. Avny *et al.*, "Preparation, Characterization, and Application of Au-Shell/Polystyrene Beads and Au-Shell/Magnetic Beads," 13(16), 1253-1256 (2001).

[119] V. Ntziachristos, "Going deeper than microscopy: the optical imaging frontier in biology," Nat Methods, 7(8), 603-614 (2010).

[120] R. Weissleder, and M. J. Pittet, "Imaging in the era of molecular oncology," Nature, 452(7187), 580-9 (2008).

[121] D. Razansky, M. Distel, C. Vinegoni *et al.*, "Multispectral opto-acoustic tomography of deep-seated fluorescent proteins in vivo," Nature Photonics, 3(7), 412-417 (2009).

[122] A. Krumholz, D. M. Shcherbakova, J. Xia *et al.*, "Multicontrast photoacoustic in vivo imaging using near-infrared fluorescent proteins," Sci Rep, 4, 3939 (2014).

[123] J. Laufer, A. Jathoul, M. Pule *et al.*, "In vitro characterization of genetically expressed absorbing proteins using photoacoustic spectroscopy," Biomedical Optics Express, 4(11), 2477-2490 (2013).

[124] V. Ntziachristos, and D. Razansky, "Molecular Imaging by Means of Multispectral Optoacoustic Tomography (MSOT)," Chemical Reviews, 110(5), 2783-2794 (2010).

[125] K. D. Piatkevich, F. V. Subach, and V. V. Verkhusha, "Engineering of bacterial phytochromes for near-infrared imaging, sensing, and light-control in mammals," Chem Soc Rev, 42(8), 3441-52 (2013).

[126] R. Weissleder, and V. Ntziachristos, "Shedding light onto live molecular targets," Nat Med, 9(1), 123-8 (2003).

[127] E. Giraud, and A. Vermeglio, "Bacteriophytochromes in anoxygenic photosynthetic bacteria," Photosynth Res, 97(2), 141-53 (2008).

[128] M. T. Tran, J. Tanaka, M. Hamada *et al.*, "In vivo image analysis using iRFP transgenic mice," Exp Anim, 63(3), 311-9 (2014).

[129] N. C. Rockwell, and J. C. Lagarias, "A brief history of phytochromes," Chemphyschem, 11(6), 1172-80 (2010).

[130] M. E. Auldridge, and K. T. Forest, "Bacterial phytochromes: more than meets the light," Crit Rev Biochem Mol Biol, 46(1), 67-88 (2011).

[131] D. M. Shcherbakova, A. A. Shemetov, A. A. Kaberniuk *et al.*, "Natural photoreceptors as a source of fluorescent proteins, biosensors, and optogenetic tools," Annu Rev Biochem, 84, 519-50 (2015).

[132] K. G. Chernov, T. A. Redchuk, E. S. Omelina *et al.*, "Near-Infrared Fluorescent Proteins, Biosensors, and Optogenetic Tools Engineered from Phytochromes," Chem Rev, 117(9), 6423-6446 (2017).

[133] O. S. Oliinyk, K. G. Chernov, and V. V. Verkhusha, "Bacterial Phytochromes, Cyanobacteriochromes and Allophycocyanins as a Source of Near-Infrared Fluorescent Probes," Int J Mol Sci, 18(8), (2017).

[134] D. Bellini, and M. Z. Papiz, "Structure of a bacteriophytochrome and light-stimulated protomer swapping with a gene repressor," Structure, 20(8), 1436-46 (2012).

[135] X. Yang, E. A. Stojkovic, J. Kuk *et al.*, "Crystal structure of the chromophore binding domain of an unusual bacteriophytochrome, RpBphP3, reveals residues that modulate photoconversion," Proc Natl Acad Sci U S A, 104(30), 12571-6 (2007).

[136] J. R. Wagner, J. Zhang, D. von Stetten *et al.*, "Mutational analysis of Deinococcus radiodurans bacteriophytochrome reveals key amino acids necessary for the photochromicity and proton exchange cycle of phytochromes," J Biol Chem, 283(18), 12212-26 (2008).

[137] H. Takala, A. Bjorling, O. Berntsson *et al.*, "Signal amplification and transduction in phytochrome photosensors," Nature, 509(7499), 245-248 (2014).

[138] A. N. S. I. I. (ANSI), [American National Standard for Safe Use of Lasers], (2007).

[139] J. Yao, A. A. Kaberniuk, L. Li *et al.*, "Multiscale photoacoustic tomography using reversibly switchable bacterial phytochrome as a near-infrared photochromic probe," Nat Methods, 13(1), 67-73 (2016).

[140] P. Lai, X. Xu, and L. V. Wang, "Dependence of optical scattering from Intralipid in gelatin-gel based tissue-mimicking phantoms on mixing temperature and time," J Biomed Opt, 19(3), 35002 (2014).

[141] G. S. Filonov, and V. V. Verkhusha, "A near-infrared BiFC reporter for in vivo imaging of protein-protein interactions," Chem Biol, 20(8), 1078-86 (2013).

[142] D. M. Shcherbakova, M. Baloban, A. V. Emelyanov *et al.*, "Bright monomeric near-infrared fluorescent proteins as tags and biosensors for multiscale imaging," Nat Commun, 7, 12405 (2016).

[143] K. E. Luker, L. A. Mihalko, B. T. Schmidt *et al.*, "In vivo imaging of ligand receptor binding with Gaussia luciferase complementation," Nat Med, 18(1), 172-7 (2011).

[144] K. E. Luker, M. C. Smith, G. D. Luker *et al.*, "Kinetics of regulated protein-protein interactions revealed with firefly luciferase complementation imaging in cells and living animals," Proc Natl Acad Sci U S A, 101(33), 12288-93 (2004).

[145] R. Paulmurugan, Y. Umezawa, and S. S. Gambhir, "Noninvasive imaging of protein-protein interactions in living subjects by using reporter protein complementation and reconstitution strategies," Proc Natl Acad Sci U S A, 99(24), 15608-13 (2002).

[146] V. Villalobos, S. Naik, M. Bruinsma *et al.*, "Dual-color click beetle luciferase heteroprotein fragment complementation assays," Chem Biol, 17(9), 1018-29 (2010).

[147] T. F. Massoud, R. Paulmurugan, and S. S. Gambhir, "A molecularly engineered split reporter for imaging protein-protein interactions with positron emission tomography," Nat Med, 16(8), 921-6 (2010).

[148] D. M. Shcherbakova, M. Baloban, and V. V. Verkhusha, "Near-infrared fluorescent proteins engineered from bacterial phytochromes," Curr Opin Chem Biol, 27, 52-63 (2015).

[149] M. Morell, A. Espargaro, F. X. Aviles *et al.*, "Detection of transient protein-protein interactions by bimolecular fluorescence complementation: the Abl-SH3 case," Proteomics, 7(7), 1023-36 (2007).

[150] M. L. MacDonald, J. Lamerdin, S. Owens *et al.*, "Identifying off-target effects and hidden phenotypes of drugs in human cells," Nat Chem Biol, 2(6), 329-37 (2006).

[151] K. E. Miller, Y. Kim, W. K. Huh *et al.*, "Bimolecular Fluorescence Complementation (BiFC) Analysis: Advances and Recent Applications for Genome-Wide Interaction Studies," J Mol Biol, 427(11), 2039-2055 (2015).

[152] R. Horstmeyer, H. Ruan, and C. Yang, "Guidestar-assisted wavefront-shaping methods for focusing light into biological tissue," Nature photonics, 9(9), 563-571 (2015).

[153] X. Xu, H. Liu, and L. V. Wang, “Time-reversed ultrasonically encoded optical focusing into scattering media,” Nature Photonics, 5(3), 154-157 (2011).

[154] K. Si, R. Fiolka, and M. Cui, “Fluorescence imaging beyond the ballistic regime by ultrasound-pulse-guided digital phase conjugation,” Nature photonics, 6(10), 657-661 (2012).

[155] Y. M. Wang, B. Judkewitz, C. A. DiMarzio *et al.*, “Deep-tissue focal fluorescence imaging with digitally time-reversed ultrasound-encoded light,” Nature communications, 3, 928 (2012).

[156] H. Ruan, J. Brake, J. E. Robinson *et al.*, “Deep tissue optical focusing and optogenetic modulation with time-reversed ultrasonically encoded light,” Science Advances, 3(12), eaao5520 (2017).

[157] C.-L. Hsieh, Y. Pu, R. Grange *et al.*, “Digital phase conjugation of second harmonic radiation emitted by nanoparticles in turbid media,” Optics Express, 18(12), 12283 (2010).

[158] N. Ji, D. E. Milkie, and E. Betzig, “Adaptive optics via pupil segmentation for high-resolution imaging in biological tissues,” Nat Meth, 7(2), 141-147 (2010).

[159] J. Tang, R. N. Germain, and M. Cui, “Superpenetration optical microscopy by iterative multiphoton adaptive compensation technique,” Proceedings of the National Academy of Sciences, 109(22), 8434-8439 (2012).

[160] O. Katz, E. Small, Y. Guan *et al.*, “Noninvasive nonlinear focusing and imaging through strongly scattering turbid layers,” Optica, 1(3), 170 (2014).

[161] I. N. Papadopoulos, J.-S. Jouhanneau, J. F. A. Poulet *et al.*, “Scattering compensation by focus scanning holographic aberration probing (F-SHARP),” Nature Photonics, 11(2), 116 (2017).

[162] I. M. Vellekoop, M. Cui, and C. Yang, “Digital optical phase conjugation of fluorescence in turbid tissue,” Applied Physics Letters, 101(8), 081108 (2012).

[163] C. Ma, X. Xu, Y. Liu *et al.*, “Time-reversed adapted-perturbation (TRAP) optical focusing onto dynamic objects inside scattering media,” Nature Photonics, 8(12), 931-936 (2014).

[164] E. H. Zhou, H. Ruan, C. Yang *et al.*, “Focusing on moving targets through scattering samples,” Optica, 1(4), 227-232 (2014).

[165] F. Kong, R. H. Silverman, L. Liu *et al.*, “Photoacoustic-guided convergence of light through optically diffusive media,” Optics letters, 36(11), 2053-2055 (2011).

[166] T. Chaigne, O. Katz, A. C. Boccara *et al.*, “Controlling light in scattering media non-invasively using the photoacoustic transmission matrix,” Nature Photonics, 8(1), 58-64 (2014).

[167] P. Lai, L. Wang, J. W. Tay *et al.*, “Photoacoustically guided wavefront shaping for enhanced optical focusing in scattering media,” Nature Photonics, 9(2), 126-132 (2015).

[168] H. Ruan, T. Haber, Y. Liu *et al.*, “Focusing light inside scattering media with magnetic-particle-guided wavefront shaping,” Optica, 4(11), 1337 (2017).

[169] Z. Yu, J. Huangfu, F. Zhao *et al.*, “Time-reversed magnetically controlled perturbation (TRMCP) optical focusing inside scattering media,” Scientific reports, 8(1), 2927 (2018).

[170] H. Ruan, M. Jang, and C. Yang, "Optical focusing inside scattering media with time-reversed ultrasound microbubble encoded light," Nature Communications, 6, 8968 (2015).
[171] H. Takala, A. Björling, O. Berntsson *et al.*, "Signal amplification and transduction in phytochrome photosensors," Nature, 509, 245 (2014).
[172] V. V. Lychagov, A. A. Shemetov, R. Jimenez *et al.*, "Microfluidic System for In-Flow Reversible Photoswitching of Near-Infrared Fluorescent Proteins," Analytical Chemistry, 88(23), 11821-11829 (2016).
[173] J. Ge, M. Lan, B. Zhou *et al.*, "A graphene quantum dot photodynamic therapy agent with high singlet oxygen generation," Nature Communications, 5, 4596 (2014).
[174] N. M. Idris, M. K. Gnanasammandhan, J. Zhang *et al.*, "In vivo photodynamic therapy using upconversion nanoparticles as remote-controlled nanotransducers," Nature Medicine, 18, 1580 (2012).
[175] D. E. J. G. J. Dolmans, D. Fukumura, and R. K. Jain, "Photodynamic therapy for cancer," Nature Reviews Cancer, 3, 380 (2003).
[176] T.-W. Chen, T. J. Wardill, Y. Sun *et al.*, "Ultrasensitive fluorescent proteins for imaging neuronal activity," Nature, 499(7458), 295 (2013).
[177] Y. Gong, C. Huang, J. Z. Li *et al.*, "High-speed recording of neural spikes in awake mice and flies with a fluorescent voltage sensor," Science, 350(6266), 1361-1366 (2015).
[178] K. Deisseroth, "Optogenetics," Nature methods, 8(1), 26 (2011).
[179] E. S. Boyden, F. Zhang, E. Bamberg *et al.*, "Millisecond-timescale, genetically targeted optical control of neural activity," Nature neuroscience, 8(9), 1263 (2005).
[180] N. Ji, D. E. Milkie, and E. Betzig, "Adaptive optics via pupil segmentation for high-resolution imaging in biological tissues," Nature methods, 7(2), 141 (2009).
[181] N. G. Horton, K. Wang, D. Kobat *et al.*, "In vivo three-photon microscopy of subcortical structures within an intact mouse brain," Nature photonics, 7(3), 205 (2013).
[182] L. Li, L. Zhu, C. Ma *et al.*, "Single-impulse panoramic photoacoustic computed tomography of small-animal whole-body dynamics at high spatiotemporal resolution," Nature biomedical engineering, 1(5), 0071 (2017).
[183] J. Yao, L. Wang, J.-M. Yang *et al.*, "High-speed label-free functional photoacoustic microscopy of mouse brain in action," Nature methods, 12(5), 407 (2015).
[184] A. V. Leopold, K. G. Chernov, A. A. Shemetov *et al.*, "Neurotrophin receptor tyrosine kinases regulated with near-infrared light," Nature communications, 10(1), 1129 (2019).
[185] A. A. Kaberniuk, A. A. Shemetov, and V. V. Verkhusha, "A bacterial phytochrome-based optogenetic system controllable with near-infrared light," Nature methods, 13(7), 591-597 (2016).
[186] T.-W. Chen, T. J. Wardill, Y. Sun *et al.*, "Ultrasensitive fluorescent proteins for imaging neuronal activity," Nature, 499, 295 (2013).
[187] G. Ku, and L. V. Wang, "Scanning microwave-induced thermoacoustic tomography: Signal, resolution, and contrast," Medical Physics, 28(1), 4-10 (2001).
[188] R. A. Kruger, D. R. Reinecke, and G. A. Kruger, "Thermoacoustic computed tomography–technical considerations," Medical physics, 26(9), 1832-1837 (1999).

[189] M. Xu, and L. V. Wang, "Time-domain reconstruction for thermoacoustic tomography in a spherical geometry," IEEE transactions on medical imaging, 21(7), 814-822 (2002).

[190] R. A. Kruger, K. K. Kopecky, A. M. Aisen *et al.*, "Thermoacoustic CT with radio waves: A medical imaging paradigm," Radiology, 211(1), 275-278 (1999).

[191] G. Ku, B. D. Fornage, X. Jin *et al.*, "Thermoacoustic and photoacoustic tomography of thick biological tissues toward breast imaging," Technology in cancer research & treatment, 4(5), 559-565 (2005).

[192] Y. Xu, and L. V. Wang, "Rhesus monkey brain imaging through intact skull with thermoacoustic tomography," ieee transactions on ultrasonics, ferroelectrics, and frequency control, 53(3), 542-548 (2006).